Coláiste na Tríonóide, Baile Átha Cliath
Trinity College Dublin
Ollscoil Átha Cliath | The University of Dublin

# The Optimisation of Silicas: Pre-treatment, Grafting & Potential Devices.

Presented for the degree of Doctor of Philosophy
National University of Ireland.

By

**Tom F. O'Mahony**

B.Sc., M.Sc.

Under the supervision of Professor Michael Morris

Department of Chemistry,
Trinity College Dublin,
Ireland.

2021

# Declaration

I, Tom F. O'Mahony, declare that this thesis has not been submitted as an exercise for a degree at this or any other university and it is entirely my own work.

Tom F. O'Mahony

## Abstract

Silica materials especially mesoporous silicas are prime candidates as materials which could help solve many issues currently existing such as rising CO2 levels as capture devices and rising levels of cancer worldwide as therapeutics. Interest in these materials are always rising due to the large amount of applications which these materials hold a good portion of the research. From adsorption processes in waste streams and exhaust systems to supports of enzymes and catalysts, silicas offer large benefits to these areas of study.

In chapter 1, the main motivations as to why the research presented during this PhD was carried out are discussed. The chapter explains the current challenges facing the various sectors, based on the application associated with that particular area. It lays out the fundamentals associated with mesoporous silicas which include synthesis, grafting and characterisation of resulting products.

In chapter 2 the synthetic methods to produce silica throughout the results chapters are outline and discussed. The methods of characterisation including the techniques used are also described along with their governing principals.

In chapter 3 the role of cleaning methods is examined in terms of their effect on mesoporous silicas. The cleaning of silica surfaces is a critical step in the semiconductor industry and is carried out before functionalisation to prime the surface for attachment with whatever ligand or agent is being attached. The chapter examines this effect in mesoporous silicas and looks to determine if it has any effect on latter grafting quantities.

In chapter 4 the functionalisation of mesoporous silicas SBA-15 and MCM-41 with polymers is examined. Hydroxyl-terminated poly-2-vinyl pyridine is used and the optimal conditions for grafting are determined. Using SBA-15 grafted poly-2-vinyl pyridine, metal salts can be infiltrated into the polymer layer and were examined with potential applications such as heavy metal adsorption from waste streams and as a catalyst in mind.

Chapter 5 explores the incorporation of antimicrobial essential oils (EO) into mesoporous silica, SBA-15 for potential application food packaging. The development of a simple method to load antimicrobial EO within a support material chemically bound to a substrate was explored. Mesoporous silica (SBA-15) was functionalised *via* a post-synthetic reaction using (3-aminopropyl) triethoxysilane (APTES) and then grafted to a 3-glycidyloxypropyltrimethoxysilane (GPTS) modified surface. The smart delivery device was assessed against common food spoilage microorganisms.

In chapter 6 final conclusions are wrapped up and potentially new lines of enquiries which could be examined are outlined in future works.

## Acknowledgements

The work in this thesis has been made possible by the help and support of several people throughout these past four years and beyond who offered guidance and support at times when it was needed. I thank you very much for all the help along the road.

My utmost appreciation to Prof. Mick Morris for the opportunity and encouragement to begin this project. Throughout the time spend in TCD, he always backed my ideas and gave me all available knowledge and resources to help me to succeed. The patience, faith and support shown in meetings, whether private or public was always reassuring and gave me confidence in what I was trying to do even when I didn't believe it. I would also like to thank the others along the way who gave enormous contributions at various stages. To Cian Cummins for helping me at the beginning to get started and showing me the ropes around the lab and the university. His patience is second to none for all the questions he answered, even after multiple answers on the same topic and on material not in his immediate background. It was only after Cian left that the gap which he filled was noticed and shows the full measure of the guy to never look for thanks and appreciation. He truly is a gentleman and good friend. To David Sullivan and Ross Lundy for helping solve questions along the way and providing great ideas to add to my research. They both collaborated on multiple research ideas and always helped to offer ideas and support. To the rest in the Morris group (too many to mention) for the fun and encouragement, it was all invaluable and I just want to thank you all. I also need to mention Dr Mark Kavanagh (Geology), Dr. Manuel Reuther and Dr. John O'Brien (Chemistry), Clive Downing (AML) and Alan O'Meara (Physics) all from Trinity college, for helping when I needed specific advice or techniques at critical times. Finally, those in CRANN, AML and Chemistry who made time enjoyable while in the university.

Lastly, I need to thank my family (Mam & Dad, Eliz, Richard & the girls, Trish, Cian & Charlotte) and Aoife for all their support. They are the true heroes who helped me to get through this when times were hard. Their constant encouragement and drive really helped me get to this long end

point. Too my parents, for always giving me every opportunity, I thank you so much. You both were always willing to drop everything if I ever needed help. This is as much for you both as for me so again I cannot thank you both enough. Aoife thank you for all you do for me. Without question, you help and share the struggle with everything we encounter and the unwavering love you have always shown. Thank you so much. This is dedicated to you all.

## Published Articles

1. **O'Mahony, T.F**; Morris, M, Hydroxylation methods for mesoporous silica and their impact on surface functionalisation *Microporous and Mesoporous Materials* **2021,** 110989, DOI: 10.1016/j.micromeso.2021.110989.
2. Lundy, R; Yadav, P; Prochukhan, N; Giraud, E; **O'Mahony, T. F**; Selkirk, A; Mullen, E; Conway, J; Turner, M; Daniels, S; Mani-Gonzalez, P; Snelgrove, M; Bogan, J; McFeely, C; O'Connor, R; McGlynn, E; Hughes, G; Cummins, C; Morris, M., Monolayer Point' in Polymer Brush Films for Fabricating Highly Coherent TiO2 Thin Films by Vapor Phase Infiltration *Langmuir* **2020**, DOI: 10.1021/acs.langmuir.0c02512
3. Mah, P T; O'Connell, P; Focaroli, S; Lundy, R; **O'Mahony, T. F**.; Hastedt, J E; Gitlin, I; Oscarson, S; Fahy, J V; Marie, A., The use of hydrophobic amino acids in protecting spray dried trehalose formulations against moisture-induced changes *European Journal of Pharmaceutics and Biopharmaceutics* 144, **2019**,139-153.
4. **O'Mahony, T.F**; Sullivan, D.J; Cruz-Romero, M.C; Cummins, E; Kerry, J.P; Morris, M.A., The use of porous silica particles as carriers for a smart delivery of antimicrobial essential oils in food applications *ACS Omega* **2021**, 6, 45, 30376-30385 https://doi.org/10.1021/acsomega.1c03549

## Abbreviations & Acronyms

| | |
|---|---|
| AFM | Atomic force microscopy |
| APTES | 3-Aminopropyltriethoxysilane |
| APTS | 3-Aminopropyltriethoxysilane |
| ATP | Adenosine triphosphate |
| ATR | Attenuated total reflectance |
| BCPs | Block copolymers |
| BET | Brunauer-Emmett-Teller |
| BJH | Barrett-Joyner-Halenda |
| BSA | Bovine serum albumin |
| C18 | Octadecyl silane derivative |
| CEL | Cellulase |
| Cp | Cross polarization |
| CHN | Carbon-Hydrogen-Nitrogen |
| COF | Covalently ordered frameworks |
| CPG | Crystalline porous glass (silica) |
| CTAB | Hexadecyltrimethylammonium bromide |
| DMSO | Dimethyl sulfoxide |
| DDS | Drug delivery system |
| EOs | Essential oils |
| ESCA | Electron spectroscopy for chemical analysis |

| | |
|---|---|
| FDA | Food & drug administration |
| FSM | Folded sheet mesoporous |
| FTIR | Fourier-transform infrared spectroscopy |
| GPTS | 3-glycidyloxypropyltrimethoxysilane |
| GRAS | Generally recognized and safe |
| HMF | 5-hydroxymethylfurfural |
| HMS | Hexagonal mesoporous silicas |
| HPLC | High performance liquid chromatography |
| ISO | International Organization for Standardization |
| LYS | Lysozyme |
| MASNMR | Magic angle spinning nuclear magnetic resonance |
| MCF | Mesocellular foam (silica) |
| MCM | Mobil composition of matter (silica) |
| MIC | Minimum inhibition concentration |
| MOF | Metal organic framework |
| MPTMS | 3-mercaptopropyl trimethoxysilane |
| MSI | Metal salt inclusion |
| MSN | Mesoporous silica nanoparticle |
| $M_w$ | Molecular weight |
| NAMs | Natural antimicrobial materials |
| NMR | Nuclear magnetic resonance |

| | |
|---|---|
| NP | Nanoparticle |
| OEO | Oregano essential oils |
| ODS | Octadecylsilane |
| OMS | Ordered mesoporous silica |
| P123 | Pluronic 123 ($PEO_{20}PPO_{70}PEO_{20}$) |
| P2vP | Poly-2-vinyl pyridine |
| P2vP-OH | Hydroxy-terminated Poly-2-vinyl pyridine |
| P4vP | Poly-4-vinyl pyridine |
| PCMS | Poly (chloromethyl styrene) |
| PEG | Polyethylene glycol |
| PGMA | Poly (glycidyl methacrylate) |
| PMOs | Periodic mesoporous organosilicas |
| RCA | Radio Corporation of America |
| RPLC | Reverse phase liquid chromatography |
| SBA | Santa Barbara amorphous (silica) |
| SC | Standard cleaning |
| SEC | Size exclusion chromatography |
| SEM | Scanning electron microscopy |
| SIS | Sequential infiltration synthesis |
| ssNMR | Solid state Nuclear magnetic resonance |
| TEM | Transmission electron microscopy |

| | |
|---|---|
| TEOS | Tetraethyl ortho silicate |
| THF | Tetrahydrofuran |
| TGA | Thermogravimetric analysis |
| TGA-DTG | Thermogravimetric analysis – Derivative thermogravimetry |
| UHPLC | Ultra-high-pressure liquid chromatography |
| XPS | X-ray photoelectron spectroscopy |
| XRD | X-ray diffraction |
| MASNMR | Magic angle spinning nuclear magnetic resonance |

# Table of Contents

# *Chapter 1*

# *Introduction*

## 1.1 Porous materials

The term ‘porous materials’ is incredibly vague and is widely used to describe so much in an ever-expanding field. From zeolites in the 1940s[1] to novel covalently ordered frameworks (COFs)[2,3] today, materials are still being developed and innovated to deal with many niche issues which exist, of which porous materials have a huge impact. Porous materials although a vast umbrella, can be defined by several different properties. Porous materials can be crystalline (quartz) or amorphous (colloidal). They can occur naturally while most used in supports and devices are synthesized. Silica or other oxide-based materials such as alumina[4] and titania[5] materials also account for a large proportion of these which are classified as inorganic materials whereas materials such as COFs are considered fully organic materials. Somewhere in the middle of these mentioned are metal organic frameworks (MOFs)[6–8]. By diving into different categories of these materials, one finds that these can be further classified based on their morphologies and dimensions.

The most important of these classifications though is based on the surface chemistry of porous materials. Pores are divided in to macropores, mesopores and micropores[9]. Understanding the pore structure of the material is vital as it more often than not determines the application or area to which the material can have the most impact. Macroporous materials have pore sizes greater than 50 nm and include porous glasses such as controlled porous glass (CPG). Mesoporous materials have pore sizes ranging between 2 and 50 nm and includes silica materials such as mesocellular foam (MCF). Microporous materials have pore sizes less than 2 nm and zeolites are an example of such. Due to the pore network of many of these porous materials, applications in areas which utilise processes such as adsorption and chemical interactions to produce materials in catalysis, separations, and storage. Of all the materials that could be discussed, it is the area of porous silicas which will be discussed in this chapter and thesis.

## 1.2 Silica

### *1.2.1 Naturally occurring silicas*

Silicon is the most abundant metal on earth accounting for approximately 55% of the crust and therefore leads to formation of many natural silicate species. There are many silicas which occur naturally which tend to be categorised into crystalline and amorphous. Crystalline silicas include cristobalite, stishovite, tridymite and of course quartz, of which is the most well-known due to its wide use in watches. Quartz is formed from a natural hydrothermal method and occurs in two states alpha and beta. The crystal forms a tectosilicate structure with a framework of a hexagonal symmetry along with channels which run parallel along the c axis[10]. Cristobalite and tridymite are two crystalline polymorphs which contain a more open structure allowing for the incorporation of other dopants when compared with quartz. Tridymite has a two layer crystalline structure whereas cristobalite has a three layer crystalline structure[11,12]. Cristobalite is formed under high temperature and for that reason is often found in volcanic rocks. Opal is another form of silica except in its purest form is amorphous. Opal has a high degree of hydration and due to this and other additions to its make-up, is found with limited crystallinity. There are multiple polymorphs of opal and are labelled opal-A, opal-C and opal-CT[11,12]. Finally, other naturally occurring amorphous silicas include diatomaceous earth and infusorial earth.

### *1.2.2 Synthetic silicas*

Silicas have been synthesised for decades. Using the sol-gel method (detailed in section 1.4.1), silica is prepared into various morphologies and sizes. These low-cost silica sols in solution produce particles in which do not settle or agglomerate. These are sometimes classified as dispersed silica systems. These sols can produce gels in which the silica forms a three-dimensional network which spans the total volume of the solvent phase. These gels are often produced in alcoholic solvents but if prepared in water they are known as hydrogels[13,14]. The addition of fillers into the silica network solution can also add to keeping the structure from shrinking during drying producing more silica materials with varying properties. Further processing of these gels

by drying for instance removes the solvent phase leaving behind the three-dimensional network of amorphous silica which are known as xerogels in which a large shrinkage typically occurs[15]. If for instance the solvent is removed using a gas (i.e. super-critical fluids) to fill the space of the gel, the resulting silica framework is known as an aerogel. These aerogels are typically fragile but can consist of a pore structure that is predominantly air, up to 95%[13,16–18].

A major technological advance in the field of porous silicas came with Stober et al, when they used the sol-gel method to synthesise monodisperse spherical silica particles[19]. Obviously, in the infancy of its development but the method changed the face of analytical chemistry especially chromatography[20]. The ability to consistently produce particles of the same morphology and size, enormously change the efficiency of columns in chromatography by allowing columns to be regularly packed with uniform spheres[21]. These particles be they nano- or micron- sized, drove development further to more adventitious properties by building on the stober process[22–24]. Langsi et al grew sub-2 µm what are termed as superficially porous silica or core-shell particles[25]. These typically consist of a solid, mostly non-porous spherical core synthesised using a similar stober process and then growing multiple layers of a porous shell[26].

Fumed silicas (pyrogenic) are synthesized by combustion of silicon tetrachloride in a plasma flame producing a relatively high surface area material that is rich in silanols at the surface. These materials are often used in spectroscopic studies for better understanding of the surface properties[27]. More recently as pyrogenic silica, it is considered safe for food packaging and additives and it has gained attention for its inflammatory effects which is discussed by Sun et al[28].

Ordered mesoporous silica (OMS) materials are the most commonly used and studied silica materials. These materials offer high surface area along with high mechanical strength. As many are synthesised using what is known as a bottom-up approach, by allowing chemists the ability to control the desired physical properties. This key feature allows OMS to be synthesized to precise

parameters for optimal performance in specific applications. Li et al were able to produce large-sized mesoporous silica by changing parameters around solvent concentration and re-precipitation of silica spheres and the relationship between these[29]. Dong et al showed that recycled quartz could be used to produce silica spheres with well-defined lattice points typical of OMS. By controlling the hydrochloric acid concentration the structure and morphology could be tailored[30].

Another major advancement came with the invention of a range of different structural OMS then known as molecular sieves by Mobil, the oil exploration incorporation. Beck et al synthesised a family of mesoporous molecular sieves which varied on their crystal arrangement[31]. The family consisted of MCM-41 which formed a hexagonal arrangement of uniform mesopores synthesised in the range between 15 and 100 Å. MCM-48 which had displayed a well ordered cubic symmetry[31,32]. MCM-50 was also synthesised with a lamellar mesostructured.

Even within OMSs, there are a wide variety of materials which exist. Zhao et al from the university of California in Santa Barbara first synthesised a series of materials known as SBAs[33,34]. Compared with MCM-41, which is synthesised using cationic surfactants, SBAs use block copolymers. Both are however synthesised by a mechanism known as template assisted technique discussed in section 1.4.2[35]. These materials have become the most studied and used mesoporous silica of the past three decades especially the leading member of the SBA family called SBA-15. SBA-15 is arranged in a highly ordered hexagonal mesoporous structure with extremely large pore sizes along with much thicker pore walls when compared back to MCM-41. These can also be synthesised with very high surface areas up to greater than 1000 $m^2g^{-1}$[33,34]. SBA-11 consists of a cubic structure, SBA-12 with a 3-d hexagonal structure and SBA-16 with a cubic cage structure[33]. After synthesis of silica particles, removal of the block copolymer is critical for producing the porous structure. The removal of this is achieved in two ways; calcination or washing[36]. Thielemann et al showed that when removing the copolymer by washing that precise changes in volumes and mixtures of solvents can drastically change the physical properties

of the resulting SBA-15 material[37]. Rahmat et al also showed that sodium silicate could be utilised to produce SBA-15 which is typically manufactured with tetra-alkoxysilanes as a silica source[38]. It has also now become possible to synthesise SBA-15 with different morphologies as demonstrated by Gong et al in their application of oxygen sensing[39].

Other OMS exist although not as popular include Hexagonal mesoporous silicas (HMS) another branch of OMS and quite similar to that of MCM-41 was synthesised by Tanev et al using quaternary ammonium cations under strong acidic conditions to produce a much longer range order material compared with MCM-41[40]. Mesostructured cellular foam (MCF) which have attracted interest as consists of interconnected pore structure along with the large pores (size and volume) and high surface areas. They can offer advantages against other OMS in chromatography due to the larger pore sizes which allow for separation of large biomolecules while also increasing eluting time and retention of analytes[41,42]. Yan et al also developed an MCF adsorbent support which successfully captured large amount of carbon dioxide[43]. Zhang et al also showed its potential use as a drug delivery system using the controlled release of the drug simvastatin[44]. These publications display the wide variety of applications that OMSs and MCF has an impact on. Folded sheet materials (FSM) synthesised by Kuroda et al first in 1990, combined kanemite, a layered polysilicate ($NaHSi_2O_5.3H_2O$), with alkyl trimethylammonium salt solutions to produce layers of silica which condensed to form three dimensional networks of porous silica[45]. It was termed FSM-16[46].

Beyond OMS there are other silica materials which are called porous glasses. These were more used as supports for size-exclusion chromatography[47] in the 1980s whereas now are typically used in enzyme immobilisation and large-scale separations[48]. They are known as controlled porous glass (CPG). These glasses are typically far more disordered than silicas such as MCM-41 and SBA-15 and have much wider pore size distributions than those already mentioned[49]. CPG can be synthesised depending on the thermal treatment to produce porous supports which range in pore diameters from 30 Å (mesopores) to more than 1000 Å (micropores). The glass also behaves

in very similar ways as many of the silica materials already discussed due to silanol groups lining the surface of the porous wall network[50,51].

## 1.3 Properties of silica

### *1.3.1 Crystalline & Amorphous*

It must be stated from the offset that the absolute majority of porous silicas are amorphous. Unger stated when defining criterion of porosity that in a few instances after prolonged high-temperature treatment of silica, a small degree of crystallinity is observed[52]. Tranter et al synthesised a porous crystalline silica named 'Gubka' which translates as sponge from Russian, as a novel adsorbent[53]. After these examples, most other synthetic silicas are amorphous. Silicas such as spherical monodisperse Stober particles are completely amorphous with no defined internal structure but a web of siloxane and silanol groups. Other silicas such as SBA-15 are amorphous but have a regular crystal lattice point and consists of long-range order due to its mechanism of formation from micelles to the formation of a regular hexagonal pore structure[54]. Similarly with MCM-41, it displays a highly ordered hexagonal array of one dimensional pores but the make-up of the pore walls are completely amorphous[31,55].

Finally, silicon wafers which are by far the most used silica material across the world [56]. These wafers are present in every computer and phone across the planet and is produced at a scale which is unfathomable. Silicon dioxide wafers are ultra-flat and non-porous the exact opposite to all these materials which have been discussed in detail. What wafers do have in common is the same silicon tetrahedra which make up the same siloxane (Si-O-Si) and silanol (Si-OH) groups. This in turn gives it the similar possibilities for interactions and procedures and therefore potential applications to be included in this thesis.

### *1.3.2 Surface Chemistry*

The most important aspect of silica is its surface. The make-up of the surface will depend on what is achievable in terms of activity and the ability to carry out a function in an application. The silica surface is where all interactions with external forces occurs, be this on the surface inside the pores of high surface area silicas or ultra-flat silica wafers. The surface is predominately made up of mostly hydrophobic siloxane bonds and hydrophilic silanol groups. Silicon surface atoms can be joined by either a single hydroxyl species or multiple groups. These are termed isolated silanol (single), geminal (silanediol) and silanetriol of which the latter has not been experimentally found and is thought to only exist theoretically[52,57,58]. These highly polar active sites are the primary source of modification and interaction compared with the siloxane bridges which are considered less reactive. Zhuravlev in 1987, found that the average number of silanols on the surface of fully hydroxylated silica is 4.6 OH groups $nm^{-2}$ [59] The number is still widely accepted as correct. Zhuravlev also developed a model to continue to predict this density of hydroxyls as the material goes through various stages of various parameters (temperature, formation mechanism, water concentration). For instance, as silica is heated from 200 ˚C to over 1000 ˚C, silanol groups are lost from the surface by dehydroxylation to produce more siloxane bridges[60]. Rehydroxylation occurs when cooled and hydrated.

Another important property of surface silanols is their ability to form hydrogen bonds with adjacent silanols groups. Silanols which carry out these intramolecular interactions, are known as vicinal silanols. Vicinal silanols play an important role in reactivity as they are coupled with an adjacent silanol through hydrogen bonding. Reactivity is reduced when compared to a silanol which is isolated. This was demonstrated by Ong et al[61].

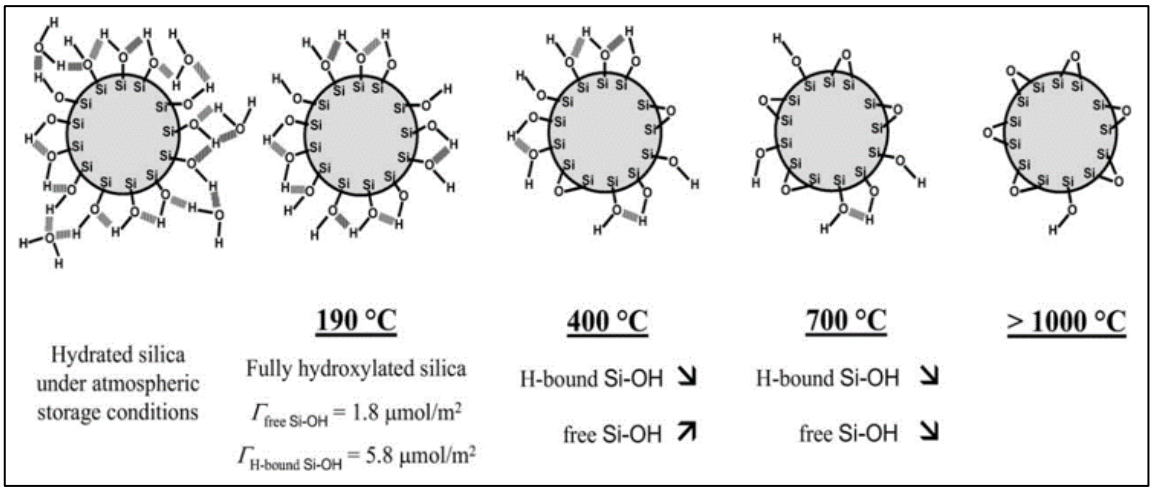


**Figure 1.3.1: Schematic illustration of changes associated with silanols as silica are heated. This figure is reproduced from Dugas et al[62].**

As demonstrated by Zhuravlev, the various silicon species can interact with differing environments in many ways. In a detailed publication, it was demonstrated that silica can be fully hydroxylated when treated in water or completely dehydroxylated by undergoing calcination to temperatures beyond 1100 ˚C. Water can be fully adsorbed to surface silanols by hydrogen bonding. Silica under vacuum was also studied and tracked the physiochemical properties from what is described as all the stages through which silica undergoes heating and cooling from room temperature to 1100 ˚C[63]. The dehydroxylation of silanols begins when the temperature of the silica begins to rise. Physisorbed water is removed in the range 150 – 200 ˚C. The removal of water from the surface and pores leaves behind the above mentioned silanol groups.

Most people not in the sphere of science have experienced the surface properties associated with silica materials. Silicas used as an adsorbent in packaging, utilises its immense hygroscopic property. The ability of silanols to hydrogen bond to water resulting in layers upon layers adsorbing to the silica's surface. Due to the high polarity of the surface hydroxyl groups, adsorption of other polar solvents is also extremely likely.

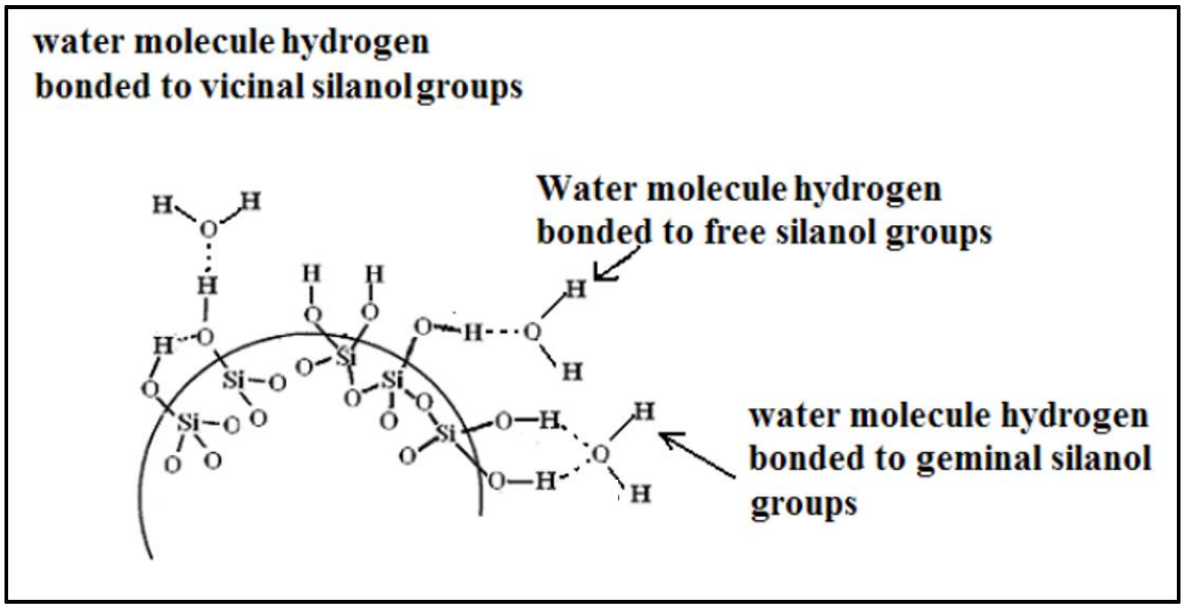


**Figure 1.3.2:** **Illustration showing hydrogen bonding between silanols and H-bond interaction of water with various silanol environments which include an isolated (free) silanol, vicinal silanol and geminal. This figure is modified from Christy et al[64,65].**

Grunberg et al examined the adsorption of water in the pores of both SBA-15 and MCM-41. The mechanism of water adsorption was found to be different due to the different pore sizes of both materials. SBA-15 has wider pores diameters than MCM-41 and thus after initial water coverage on the surface, growth of the water layer towards the pore axis. MCM-41 pores were filled with water by axial filling[66]. These reasons outline why water can also be a hinderance when working with silicas due to the high affinity for adsorption to the surface silanols. Functionalisation requires silanols to be predominantly free from interacting with water while also requiring some water present for the most common grafting methods of hydrolysis of the silane functional group[67]. Gartmann et al showed that the presence of water can lead to clustering of silanes which in turn leads to non-uniform grafting which can block pores and ultimately reduce the efficacy of the material[68]. This was also discussed by Bauer et al[69].

When discussing silica surface, it is imperative to mention silicon wafers and their place in studying the surface chemistry. All porous silica materials which have been discussed thus far, have in common a non-uniform surface with high surface areas. This is the opposite for silicon

wafer substrates which have been the base groundwork for understanding the surface chemistry and interactions of silica. The ability to measure surface changes on 'flat/uniform' surfaces is clear and observable when compared with the same measurements on porous materials. Techniques such as ellipsometry, atomic force microscopy (AFM) which can help identify silane layers readily are insignificant in the area of porous materials. This can be seen from simple measuring of the surface contact angles of silicon substrates and porous silicas[70,71]. Wafers, although sometimes easier to characterise, tend to need surface activation pre-grafting due to adsorption of organic molecules. This is carried out by many methods including acid-treatments, ultraviolet/ozonolysis or oxygen plasma treatments[72–80].

### *1.3.3 Pore structure*

The surface chemistry of silica materials is vital for many applications, but it is the pore structure which makes porous silicas absolutely critical in many sectors and in applications. In an ideal world, pores are synthesised with uniform shape and size with minimal defects. The use of the pore structure in porous silica materials is crucial in applications such as catalysis and chromatography[26,42,81–84]. As already discussed, the major advantage in terms of OMS is the ability to synthesis these materials with highly ordered pore structures such as one-dimensional hexagonal structure of MCM-41 with typical pore size ranging from 1-3 nm[85]. As MCM-41 is the standard in consistency of pore structures, other OMS are not always consistently produced. MCM-48 and SBA-15 for instance, consist of an interconnected micropore structure which can ultimately trap water and effect the material's ability to carry out its function in an application or impact its grafting ability. This was discussed by Grunberg et al where they found that water adsorption was stronger and more tightly bound in SBA-15 compared with MCM-41 due to surface defects. This further agrees with work carried out by Jun et al which demonstrated that these tiny micropores present in SBA-15 [86]which trap water in pores, do not seem to exist in MCM-41 mesoporous silicas as further outlined by Thommes et al[49]. Thielemann et al examined the changes on pore shape in SBA-15 by different washing procedures of which deduced that more

washing does not necessarily increase the homogeneity and order of the pores[37]. Gouze et al examined the role of pore size and wall porosity by comparing both MCM-41 and SBA-15. They concluded as MCM-41 consisted of smaller pore diameters lead to pore deformation and eventually clogging whereas SBA-15 is impacted much less due to the larger pore diameter[87]. SBA-15 is also known to have stronger and thicker pore walls which would agree with the findings[30,33].

With micron-sized spherical mesoporous silica particles, used typically in chromatography, the pore structure can be completely different to that experienced from OMS. These silica particles due to formation through the sol-gel route, produce pores which are completely random and sometimes internal. The interaction of analytes in chromatography within the pore structure needs careful consideration alongside other important parameters (particle size, packing uniformity, column, stationary phase chemistry, mobile phase etc.) which all impact successful chromatographic separations. Efforts to standardise the pore structure of these particles has come in the form of core-shell silica particles. These come from the synthesis of a solid core particle (sometimes non-porous) which grows controlled layers of porous silica onto the surface of the solid particle[88,89].

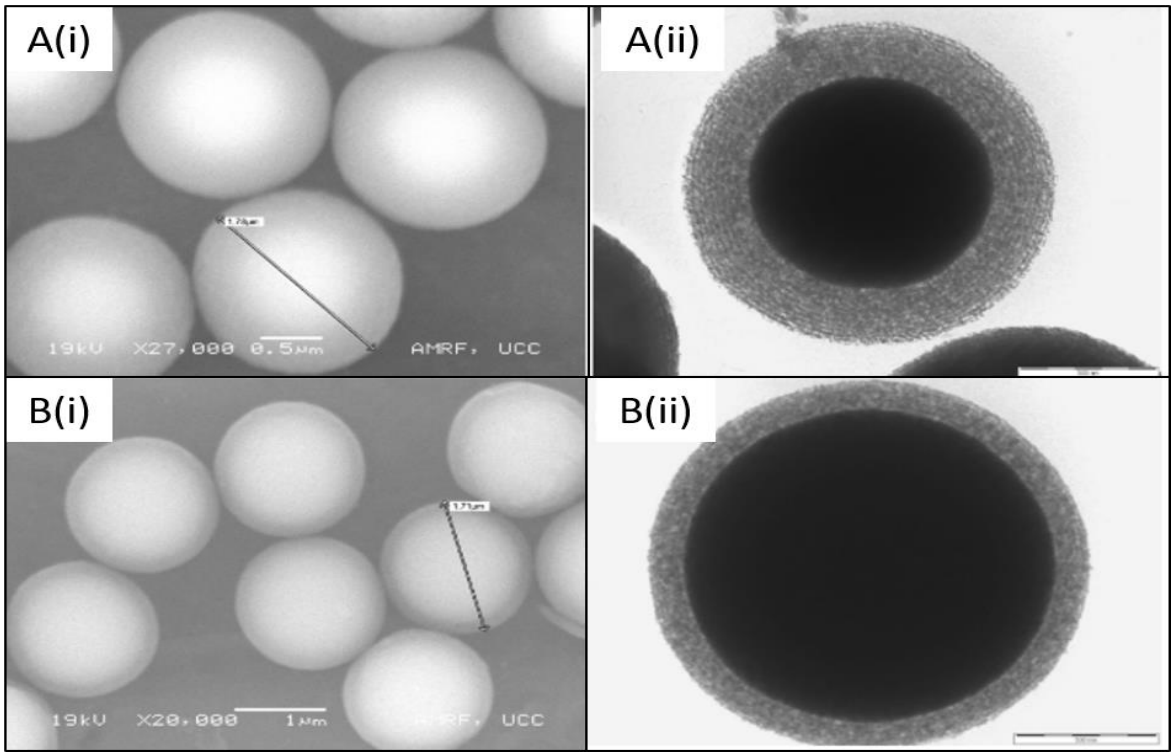


**Figure 1.3.3:** **Electron micrograph images of superficial porous silica particles. A(i) and B(i) show scanning electron microscopy images along with A(ii) and B(ii) showing transmission electron micrographs of two different core-shell particles synthesised with two varying outer shell layers. This figure is modified from Omamogho et al[89].**

## 1.4 Synthesis methods

### *1.4.1 Sol-gel method*

The method of sol-gel processing is thought to be straightforward and is readily used to produce silica particles of varying sizes, morphologies, and physical properties. The mechanism of formation on the other hand, is not simple, but a generally accepted scheme and simplified route is outlined below. The method utilises metal precursors (inorganic or organic) in aqueous or organic solvents which undergo hydrolysis and condensation to produce M-O-M bonds. The most common route to synthesizing silicas through the sol-gel route is by using a silica source derived from tetra-alkoxysilanes[74]. Tetra-ethoxysilane ($Si(OC_2H_5)_4$) and tetra-methoxysilane ($Si(OCH_3)_4$) more commonly abbreviated as TEOS and TMOS respectively, are the most often used in conjunction with an alcohol solvent system. Silicas can also be produced using other silicon sources which include sodium silicate along with other silicates[38].

The alkoxysilane is hydrolysed in water producing hydrated silica tetrahedra with the resulting alcohol dependant on what alkoxysilane is used[90–92].

$$Si(OR)_4 + 4H_2O \leftrightarrow Si(OH)_4 + 4ROH \quad \textbf{EQ.1}$$

The hydrated silica then interacts with another nearby hydrated silica and a water condensation reaction is seen.

$$2Si(OH)_4 \leftrightarrow (OH)_3Si - O - Si(OH)_3 + H_2O \quad \textbf{EQ.2}$$

This condensation reaction between the silica tetrahedra forms a siloxane bond (Si-O-Si) and in turn continues to aggregate by polycondensation reactions as long as neighbouring silanols are close enough to condense and expel water as it proceeds[58,93]. These hydrolysis and condensation reactions occur simultaneously throughout the solution mixture and form into colloids or sols to which the method gets its name. Depending on the parameters and materials, the silicic acid polymerizes into discrete particles that aggregate into various morphological networks. Polymerisation occurs in three different stages as described by Iler et al; [94]

- Polymerization of monomers into particles
- Growth of particles
- Linking of particles into chains, then networks that extend throughout the liquid medium, thickening it to a gel.

Smaller colloid particles will continue to aggregate with larger ones. Eventually stable sol particles collide, condense and agglomerate. The rate of aggregation will decrease exponentially with their increase in size. As the concentration of silanol groups increases, condensation of silanols continues in the development of a sol-gel by increasing the number of bridging bonds[95]. Stober et al synthesised monodisperse silica spheres with various particle size in 1968[19] in what is still considered the gold standard method for these types of particles. He showed by changing parameters such as temperature or by using longer chained alcohols one could achieve larger

spherical particles. Keane et al used a similar method with the addition of CTAB along with post treatment steps to produce spherical silica particles with larger size and greater pore volume[96]. Shimura et al modified the method to produce nanoporous spherical particles with much higher surface areas in the range 380-1060 $m^2$ $g^{-1}$[97]. Variables such as particle size, shape, porosity, and order can be tailored depending on temperature, pH, viscosity, and the kinetics of the hydrolysis step. Mackenzie et al highlighted the factors which impact mostly on porosity and pore size during synthesis[13].

Role of the catalyst is also very important in the sol-gel method. The method is typically carried out in either acidic or basic conditions[98]. Under acid conditions the overall route carries out an electrophilic reaction from the presence of the hydronium ion. The water attacks producing a positive charge on the protonated alkoxysilane in turn making the resulting alcohol an effective leaving group[93]. The lower the pH of the acid in turn increases the speed of the hydrolysis step. Under basic conditions, a nucleophilic substitution of hydroxyl ions with -OR groups occur where hydrolysis takes place to the alkoxysilane producing $OR^-$ group which in turn is then hydrated by water. This replenishes the hydroxyl ion for the process to be repeated. As one would expect the opposite from the acid-catalysed reactions, the higher the hydroxyl ion concentration the faster the rate of hydrolysis. Finally, other parameters are important and depend on the desired properties of the sol, of which include different acids/base, steric inductive effects of the substituents[93,95,98,99]. Hydrolysis is often the rate-determining step in base-catalysed particle growth.

### *1.4.2 Template assisted technique*

Often termed the liquid-crystal template approach which describes the formation of silica materials by the mechanism of an ordered crystallisation of silicate material between the formation of surfactant micelles in solution[55].

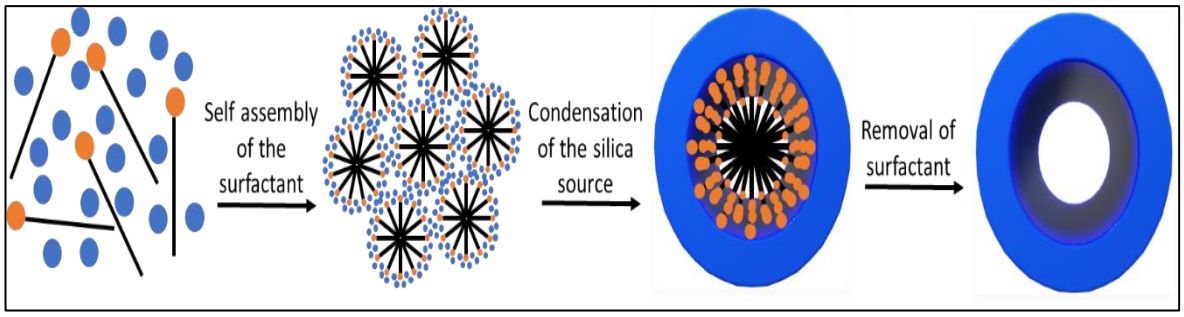


**Figure 1.4.1:** **Liquid-crystal template approach to the formation of silica. The figure shows the self-assembly of the surfactant (polar orange head with black non-polar long-chain alkyl group) with the silica source (blue spheres) in the opposite phase. The hydrolysis and polycondensation of the silica source, allowing for the controlled aggregation of silica to form a long ranged ordered silica framework. The final step of calcination of the particles, removes the organic surfactant producing porous silica.**

The mechanism first proposed by Chen et al described the formation of the surfactant micelles which interacts with the silicate source[100]. These randomly form into ordered rod-shaped micelles. The silica source when added undergoes hydrolysis and condensation and due to the polarity of the silica species and micelles, the silica follows the directing template along its outer surface forming silica tubes. These rod-like micelles with silica interacting on the outside wall then begin to co-condense with similar composites, in turn forming the highly favourable hexagonal arrangement of the silica framework[101–103]. Finally, to produce the mesoporous silica material, the now internal surfactant must be removed to leave behind the ordered porous framework. This is achieved by washing out the surfactant, calcination, or a mixture of both. A schematic in figure 1.4.1 shows a simple illustration of the mechanism of formation.

The resulting silica particles produce materials with highly regular pore channels of which can be tailored based on parameter changes to precise detail. These materials can be synthesised with very high surface areas and also exhibit high mechanical and thermal strength which offered them advantages over other materials in catalysis, storage, and others. Due to the mechanism of synthesis by the surfactant acting as a directing agent, the materials are produced with some crystallinity (regular lattice points) unlike most other silicas. It must be noted that the pore walls are completely amorphous but due to the highly ordered arrangement of the surface micelles, the

hydrolysis and condensation of the silica source is templated into producing a regular structure which displays long-range order.

Two of the most studied OMS, MCM-41[31,55] and SBA-15[33,34] are both synthesised using the liquid-crystal template approach. Kresge et al first reported the use of quaternary ammonium surfactants such as hexadecyl-trimethylammonium salt to synthesis MCM-41 and its counterparts [31,55]. They also highlight that by changing the surfactant one can change the width of the pore channels produced. Corma et al reported that the pore channels could be swelled and in turn change the pore size as well without the need to change surfactant[104]. Attard et al synthesised mesoporous silicas using non-ionic surfactants such as octa-ethylene glycol mono-hexadecyl ether ($C_{16}EO_8$)[105]. Most MCM-41 synthesis methods now utilise CTAB whereas SBA-15 use block co-polymers such as Pluronic 123 ($PEO_{20}PPO_{70}PEO_{20}$ - P123) [106]. Katiyar et al synthesised spherical and fibrous SBA-15 particles with larger pore sizes than typical SBA-15 materials by incorporating P123 along with CTAB and trimethylbenzene for adsorption of biomolecules in size selective separations[107].

### *1.4.3 Chemical etching technique*

Unlike the template assisted technique which uses a structure directing agent to produce porous silica materials, the chemical etching technique uses various etching agents to create the porous material[103]. Firstly, silica is typically synthesised by following a modified stober method to produce standard spherical particles (porous or non-porous). The etching agent as Chen et al showed can form the porous structure of silica while also changing the morphology of the nanostructures, in a controlled environment[108]. Sodium carbonate was used to synthesise the hollow mesoporous silica spheres and varying concentrations of ammonia was used to manufacture hollow/rattle-type mesoporous silica spheres. Zhang et al also use the wet chemical etching technique to control the morphology to produce ellipsoidal silica particles[109]. Rosu et al carried out a similar method as above by synthesising stober silica particles and then used a very

dilute (3mM) solution of sodium hydroxide. This is to ensure a slow and controlled etching of the silica surface[110].

## 1.5 Chemical modification

All silica supports or devices tend to be somewhat inert for use in many applications and thus some form of derivatisation is needed. The functionalisation tends to be dependent on the end application or intermediate stages driven by the functional group(s) critical at the end. Modification of the supports typically occurs in two ways by either direct in-situ modification or by a post-grafting method. Grafting of silica materials is typically carried out using silane based ligands which have some degree of functionality including amines[88–95], thiols[117–125], carboxylic[126] and aliphatic chains[106–111].

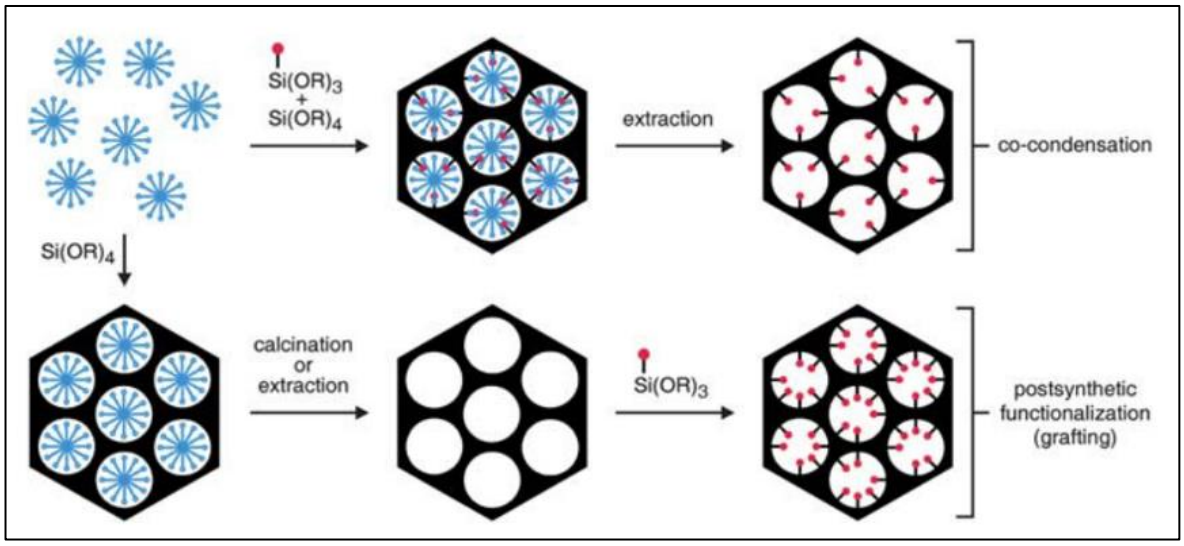


**Figure 1.5.1:** **Schematic process of mesoporous silica functionalisation. The schematic shows the co-condensation method along with post-grafting method. The template structure directing surfactant is represented by the blue micelles. The figure is reproduced from Bruhwiler et al[133].**

### *1.5.1 Direct synthesis modification*

This is also known as co-condensation method. This method of functionalisation utilises the idea of a one-pot synthesis. It follows the synthesis methods already described with the addition of

organosilanes with the desired functional groups. The difference here comes from the organosilane co-condenses with the tetra-alkoxysilane silica source as the porous material is forming. This leads to functional groups throughout the silica structure including the pores, the outer walls of the silica and the internal structure. Co-condensation functionalisation is employed during synthesis by the sol-gel[134–136] route and the template assisted technique[123,137,138]. Dobrowolski et al synthesised SBA-15 by co-condensation with 3-aminopropyl triethoxysilane (APTS) for applications in metal sorbents[139]. Hoang et al also synthesised SBA-15 by co-condensation with 3-mercaptopropyl trimethoxysilane (MPTMS)[117]. Zafarzadeh et al synthesised silica nanoparticles by a modified stober method by co-condensation with APTS for silica nanoparticles with optical properties[140]. A minor disadvantage of co-condensation functionalisation is sometimes due to while the silica structures are forming during the hydrolysis and condensation stages of synthesis, the organosilane can compete with the silica source and in turn weaken the internal structure impacting the rigidity of the structure [141].

### *1.5.2 Post-synthetic grafting*

The second more widely used method of functionalisation is post-synthesis grafting. The post-grafting of silicas is much more advantageous as it provides a more hydrothermally stable and can provide higher coverages than the co-condensation method[142]. Since the silica particles are already synthesised, grafting can only occur on the surface and therefore does not impact the internal structure of the materials. The mesostructured pores are maintained and if the desired functional R-group fits the pores even grafting can occur. Issues can arise where if the functional R-group is sterically hindered from entering the pores, grafting will occur on the outer surface and block functionalisation in the pores owning to diffusion issues and non-even grafting to the silica material[102].

Grafting of nearly all silicas, be they OMS, sol-gel spherical particles or high-spec silicon wafers, are carried out in variations of the same principals. Silanols on the surface act as active sites for

strong covalent attachment to more often than not organosilane derivatives. Just like in the formation of silica, predominantly alkoxy-organosilanes [$(R^1O)_3SiR$] are hydrolysed and undergo condensation with the silica material. This forms the covalent bond on the surface which acts as the anchor for the required functionality for the desired application. Chlorosilanes are also used to graft various functional groups to silica. They are commonly used for grafting of silica particles with end applications in chromatography and for further steps as intermediates to end-functional group synthesis[64,137]. It is also very common when grafting octadecylsilanes (ODS) to use spherical particles in chromatography columns to use halogenated silanes[143–147].

Key to successful grafting is to form a strong covalent bond between the support and the organosilane, but just as important is to ensure a homogenous coverage of the silane. Gartmann et al demonstrated that controlled functional group placement is crucial to successful silica support materials[148]. Grafting of silicon substrates, for obvious reasons, must also be carried out using post-synthetic functionalisation. Derivatisation of wafers includes similar functional groups already discussed including amines[149,150], thiols[120], polymer brushes[151–153] and a mixture of all as discussed by Vlachopoulou et al[154].

## 1.6 Applications

### *1.6.1 Catalysis*

For mesoporous silica materials, catalysis has been one of the big areas to which interest has been shown. Due to the wide range of possibilities to derivatise silicas has led them to be considered as viable devices for increasing efficiency in catalytic processes. Nearly all of the OMS discussed have been examined as options as catalysts. The advantages of high surface areas and relatively large pores is of such that the materials facilitate high mass transfer and high diffusion rates through the material offering better conversion to product rates[155,156]. The infiltration of metals into the silica support framework has shown silica to be useful in areas of CO oxidation, phenol hydrogenation, heck reaction and benzene hydrogenation just to mention a few[157–160].

Agirrezabal-Telleria et al functionalised mesoporous SBA-15 with varying sulfonic acids to carry out the cyclodehydration of xylose to furfural[161]. Crisci et al also grafted alkyl sulfonic acids to SBA-15 showing that the synthesised support was efficient and selective at the dehydration of fructose to 5-hydroxymethylfurfural (HMF)[162]. Pham et al carried out interesting dissolution studies on the ability to carry out catalysis of thiol modified silicas under basic conditions for potential use in water treatment[163]. Sadjadi et al also reviewed the ability to functionalised through intermediate steps, large organometallic complexes for encapsulating[164–168].

### *1.6.2 Enzyme Supports*

Enzyme immobilisation in terms of silica, is the process of multiple grafting stages to accommodate the use of silica as a support. Grafting typically begins with functionalisation with amines or thiols before continuing through intermediate stages to activation of the end material which has enzyme bound to the support[50,169]. The end goal typically is the separation or capture of specific proteins. Covalent attachment of the support to the protein is the most common method of immobilisation. It consists of strong binding through covalent links to the protein which offers stability and loss of leakage from the support. Other methods of immobilisation include encapsulation, cross-linking, adsorption, affinity and electrostatic interactions all of which have their advantages and disadvantages[170]. Enzymes such as *Lactobacillus rhamnosus* have been successfully immobilised on mesoporous silica supports for use as a catalyst device for lactic acid production[171]. Dezotti et al immobilised two enzymes (lignin peroxidases and horseradish peroxidase) to a silica support which they used for the removal of chlorolignins from eucalyptus effluent[172].

S.M.L. dos Santos et al synthesised mesoporous silicas SBA-15 and SBA-16 for adsorption of common biomolecules including bovine serum albumin (BSA), lysozyme (LYS) and cellulase (CEL) of which they showed high capacities of adsorption[173]. They also noted that the method

of synthesis was important in relating to adsorption capacity. Grafting procedures and protein immobilisation on silicon wafers was also shown[169,174–176] along with Kim et al[77].

### *1.6.3 Environmental*

The use of silica materials in the area of environmental chemistry has continued to grow with time due to its ability to be relatively stable in aqueous solutions. The use of mesoporous silica materials with their high surface areas and relative ease of functionalisation has benefited from its ability to carry out effective adsorption processes of water pollution including in wastewater treatment and specifically heavy metal extraction[177]. Grafting of these silica supports allows for the incorporation of functional groups which act as interacting binding sites for some heavy metals which can include copper (Cu), nickel (Ni), lead (Pb), mercury (Hg), cadmium (Cd) and zinc (Zn)[178–180]. Hernandez-Morales et al synthesised APTS grafted mesoporous SBA-15 by co-condensation method to remove lead from batch aqueous solutions concluding that highest sorption capacity achieved came from the material with the greatest amine loading[181]. Lee et al bi-functionalised porous silica with thiol and amine functional groups to enhance the properties of the porous silica. By adding functionality, the silica material could interact and adsorb other species than Hg (thiol groups selectively adsorb Hg) by increasing the hydrophilicity of the material with the addition of the amine groups[123]. Gupta et al used SBA-16 as a support which showed high selectivity for the removal of lead, mercury and cadmium[182]. More recently Kang et al functionalised silica gel with polyamines to measure the selectivity for di-valent ions which focused predominantly on Cu along with Ni, Co, Zn and Pb[183].

### *1.6.4 Gas sequestration*

Gas sequestration or more commonly carbon dioxide capture (not limited to) is a very popular topic in research due to global warming and rise in support for novel approaches to reduce and remove $CO_2$ from our atmosphere. Unlike in other applications, derivatisation of porous silica supports in this area is nearly always with nitrogen functional moieties as they selectively absorb

$CO_2$ to form carbamates[184]. Many of the discussed mesoporous silicas such as MCM-41, SBA-15, MCF and aerogels have been used[115]. Zelenak et al functionalised SBA-12 with different amino ligands which included 3-aminopropyl (APTS), 3-(methylamino) propyl and 3-(phenylamino) propyl and showed higher affinity for higher basicity of amine ligand[185]. In relation to pore size, Wang et al examined the relationship between $CO_2$ adsorption and pore diameter concluding that larger pore sizes had better $CO_2$ capture ability than smaller mesopore material[186].Mohamedali et al encapsulated imidazolium-based ionic liquids into mesoporous silicas, MCM-41 and SBA-15. These showed higher sorption rates for $CO_2$ with stable cyclic adsorption/regeneration performance[187].

### *1.6.5 Chromatography*

Of all the applications mentioned, chromatography is the largest and most widely used analytical tool in every quality control laboratory throughout the world. It consists of high-performance liquid chromatography (HPLC), size-exclusion chromatography (SEC), gas-liquid chromatography, ultra-high-pressure liquid chromatography (UHPLC) to name just a few. In all these variations of separations, silica is predominantly the backbone support material for these techniques. Silica has been used as the support material for at least the last 70-80 years[188–190]. The array of publications in areas of silanol coverage, bonding with different ligands, end-capping methods, columns, plate heights, mobile phases is so vast that each section could be the basis of many more thesis'. Many of the issues associated with chromatography come from a desire to carry out faster and more efficient separations. Taking just porous silica materials as an example has led to lots of innovation into the sector with huge companies such as Agilent, Waters, Phenomenex and Sigma leading the way. Smaller companies and research groups look to develop novel materials or niche supports for very specific separations. In a very recent publication from Pantsulaia et al, they described using core-shell porous silicas for the specific separation of enantiomers using polysaccharide based chiral selectors[191]. Nakamura et al discuss the use of different derivatised silica stationary phases by examining retention of analytes in reversed phase

liquid chromatography (RPLC). They grafted C18 and phenyl hexyl ligands to the porous silica and discussed the relationship between the aqueous and silane layers at the surface[192].

### *1.6.6 Drug delivery*

Silica particles have long been studied as vectors for safe and effective drug delivery systems (DDS) and as imaging devices. A review by Natarajan et al discussed the wide range of drugs which have been loaded to mesoporous silicas including Ibuprofen, doxorubicin and nicotinamide to name a few[193]. Zhang et al synthesised MCF silica and examined the release of a poorly soluble drug called simvastin. They discussed the importance of the physical properties of the silica material for DDS and controlling the release of the drug better[44]. Yang et al examined adsorption and release of aspirin on mesoporous MCM-41which was also loaded with luminescent composite particles ($CaWO_4$:Ln – Ln = $Eu^{3+}$, $Dy^{3+}$, $Sm^{3+}$, $Er^{3+}$) which allowed to measure the amount of aspirin incorporated on the support and its subsequent release[142].

The materials have also been used as slow release mechanisms to control the amount of a drug over time for better therapies. Slowing et al examined mesoporous silica nanoparticles as controlled drug delivery release system. These systems use a concept known as gatekeeping which encapsulates the drug loaded mesoporous silica and under specific stimuli responses will release the drug over time at specific sites. Drugs such as vancomycin and neurotransmitters such as ATP have been discussed. This technology is particularly useful when the drug is toxic (anti-cancer drugs)[194]. Kim et al for simultaneous use as a drug delivery vehicle and in bioimaging (magnetic resonance and fluorescence imaging) synthesised core-shell particles with the incorporation of iron oxide nanoparticles. The hydrophobic core with porous outer shell which incorporates the iron oxide nanoparticles (encapsulated in PEG) was used in-vivo to image tumour sites and to determine the effect of drug loading to specific sites[195].

### *1.6.7 Devices*

Devices which incorporate $SiO_2$ are typically carried out on wafer substrates. In terms of porous silica materials there is plenty of research into novel devices using the well understood chemistries and processes which have been widely discussed thus far in this chapter. Two areas which interlink and sometimes co-exist are in the development of sensors and storage devices. Yamada et al fabricated nitrogen oxide sensors onto wafers using mesoporous silicate films of the typical synthesis method described for the manufacture of SBA-15 using block co-polymer ($PEO_{20}PPO_{70}PEO_{20}$ - P123) and TEOS with hydrochloric acid. The films produced showed different performances as sensors based on the orientation of the porous film which had a major impact on the accessibility of the gas through the sensor[188]. Radu et al examined the use of mesoporous silica MCM-41nanospheres by functionalisation with polylactic acid which acts as a sensor for the selective detection of amino-containing neurotransmitters[197]. Amonette et al studied the use of aerogels as sensors due the benefit of extremely high porosity, by discussing sensors which function on humidity, oxygen, hydrocarbons, acid and alkaline gases along with other niche sensor devices[198]. Ravaro et al synthesised mesoporous silica via the sol-gel route and incorporated cadmium telluride (CdTe) quantum dots on the silica surface. The oxygen sensors produced successful optical properties when exposed to varying oxygen levels owning to the success of the silica support[199]. Yin et al used the incorporation of platinum salts into mesoporous silica to produce platinum nanoparticles heavily dispersed throughout the pore framework to act as a high performing hydrogen storage device, especially at room temperature[36].

## 1.7 Aims

While the use of silica materials in applications mentioned in section 1.6, is far from its infancy with the extensive body of research accumulated over the past decades. It is still a critical area with a continuing increase in interest to solve many issues currently experienced in these

applications. Of all the synthesis methods carried out, silica materials produced, functional groups grafted etc., behind all the research there is a common desire for increased efficiencies and robustness of processes. With so many researchers focusing on changing properties on silica and developing new devices to aide with old tasks, the thought was to take a step back and re-focus. Many issues in chromatography come from low coverages of ligands and unwanted interactions. Issues in immobilisation can be due to longevity and stability. Issues in drug delivery, storage and environmental devices is development. With a step back and re-focusing on the basic ideas of all these problems, greater impact could be made on increasing knowledge on pre-treatment methods of silica. The aims of this extensive body of work was focused on this idea in chapter 3. Zhuravlev has shown many times, that the silanol concentration on nearly all silicas is always the same. With the basic methods of grafting, all quite similar and the core chemistry at the silica surface is the same under all of the materials discussed, the thought of increasing silanol availability which in turn would increase efficiency and potential robustness of materials would increase. This was achieved by examination of surface pre-treatment steps by refluxing ordered mesoporous silicas in various solutions and then determine the effect on grafting due to this cleaning step. Chapter 4 deals with the functionalisation of mesoporous silicas with polymers. The aim of this chapter was to first understand the grafting of poly-2-vinyl pyridine to two mesoporous silicas, MCM-41 and SBA-15. Once this is optimised, the infiltration of cerium metal salt was examined. The ultimate aim of the chapter is to examine the potential application of using grafted mesoporous silicas as supports for metal uptake for applications in catalysis and environmental services. The aim of Chapter 5 is to deal with the use of silica particles in conjunction with silicon substrates to produce potential new devices for food packaging with enhanced properties in anti-microbial activity. This was examined by grafting amine loaded mesoporous silicas with silicon surfaces grafted aliphatic epoxides, covalently attaching the two. This new device could have antimicrobial activity which could open possibilities in applications of food storage and extension of its shelf-life.

## 1.8 References

[1] R.M. Barrer, Synthesis of a zeolitic mineral with chabazite-like sorptive properties, J. Chem. Soc. (1948) 127–132. https://doi.org/https://doi.org/10.1039/JR9480000127.

[2] X. Guan, H. Li, Y. Ma, M. Xue, Q. Fang, Y. Yan, V. Valtchev, S. Qiu, Chemically stable polyarylether-based covalent organic frameworks, Nat. Chem. 11 (2019) 587–594. https://doi.org/10.1038/s41557-019-0238-5.

[3] S.-Y. Jiang, S.-X. Gan, X. Zhang, H. Li, Q.-Y. Qi, F.-Z. Cui, J. Lu, X. Zhao, Aminal-Linked Covalent Organic Frameworks through Condensation of Secondary Amine with Aldehyde, J. Am. Chem. Soc. 141 (2019) 14981–14986. https://doi.org/10.1021/jacs.9b08017.

[4] J.J. Pesek, M.T. Matyska, Modified aluminas as chromatographic supports for high-performance liquid chromatography, J. Chromatogr. A. 952 (2002) 1–11. https://doi.org/10.1016/S0021-9673(00)00176-X.

[5] K.C.-W. Wu, Y. Yamauchi, C.-Y. Hong, Y.-H. Yang, Y.-H. Liang, T. Funatsu, T. Makoto, Biocompatible, surface functionalized mesoporous titania nanoparticles for intracellular imaging and anticancer drug delivery, Chem. Commun. (2011) 5232–5234.

[6] H.K. Chae, D.I. Siberio-Perez, J. Kim, Y. Go, M. Eddaoudi, A.J. Matzger, M. O'Keeffe, O.M. Yaghi, A Route to High Surface Area, Porosity and Inclusion of Large Molecules in Crystals, Nature. 427 (2004) 523–527. https://doi.org/10.1038/nature02294.1.

[7] H.-C. Zhou, S. Kitagawa, Metal–Organic Frameworks (MOFs), Chem. Soc. Rev. 43 (2014) 5415–5418. https://doi.org/10.1039/C4CS90059F.

[8] N.A. Khan, Z. Hasan, S.H. Jhung, Adsorptive removal of hazardous materials using metal-organic frameworks (MOFs): A review, J. Hazard. Mater. 244–245 (2013) 444–456.

https://doi.org/10.1016/j.jhazmat.2012.11.011.

[9] R.L.J. Burwell, International Union of Pure and Applied Chemistry Physical Chemistry Division Commission on Colloid and Surface Chemistry Manual of Symbolsand Terminology for Physicochemical Quantities and Units-Appendix Ii, Pure Appli. Chem. 46 (1976) 71–90.

[10] M.J. Wilson, Dissolution and formation of quartz in soil environments: A review, Soil Sci. Annu. 71 (2020) 99–110. https://doi.org/10.37501/soilsa/122398.

[11] M. del C. Gutiérrez-Castorena, W.R. Effland, Pedogenic and Biogenic Siliceous Features, in: Interpret. Micromorphol. Featur. Soils Regoliths, 2010: pp. 471–496. https://doi.org/10.1016/B978-0-444-53156-8.00021-0.

[12] J. Čurlík, J. Forgáč, Mineral forms and silica diagenesis in weathering silcretes of volcanic rocks in Slovakia, Geol. Carpathica. 47 (1996) 107–118.

[13] J.D. Mackenzie, Applications of the sol-gel process, J. Non. Cryst. Solids. 100 (1988) 162–168. https://doi.org/10.1016/0022-3093(88)90013-0.

[14] L. Wa, L. Fengyun, Z. Fanlu, C. Mengjing, C. Qiang, H. Jue, Z. Weijun, M. Mingwei, Preparation of silica aerogels using CTAB/SDS as template and their efficient adsorption, Appl. Surf. Sci. 353 (2015) 1031–1036. https://doi.org/10.1016/j.apsusc.2015.06.204.

[15] K. Nakanishi, Pore Structure Control of Silica Gels Based on Phase Separation, J. Porous Mater. 4 (1997) 67–112. https://doi.org/10.1023/A:1009627216939.

[16] F. Ilhan, E.F. Fabrizio, L. McCorkle, D.A. Scheiman, A. Dass, A. Palczer, M.B. Meador, J.C. Johnston, N. Leventis, Hydrophobic monolithic aerogels by nanocasting polystyrene on amine-modified silica, J. Mater. Chem. 16 (2006) 3046. https://doi.org/10.1039/b604323b.

[17] S. Sivasankar, S. Chu, Optical bonding using silica nanoparticle sol-gel chemistry, Nano Lett. 7 (2007) 3031–3034. https://doi.org/10.1021/nl071492h.

[18] R. Deshpande, D.-W. Hua, D.M. Smith, C.J. Brinker, Pore structure evolution in silica gel during aging/drying. III. Effects of surface tension, J. Non. Cryst. Solids. 144 (1992) 32–44. https://doi.org/10.1016/S0022-3093(05)80380-1.

[19] W. Stöber, A. Fink, E. Bohn, Controlled growth of monodisperse silica spheres in the micron size range, J. Colloid Interface Sci. 26 (1968) 62–69. https://doi.org/10.1016/0021-9797(68)90272-5.

[20] I. Halasz, I. Sebestian, New stationary phase for chromatography, Angew. Chemie - Int. Ed. 81 (1969) 147–153. https://doi.org/10.1016/j.chroma.2004.10.012.

[21] H. Giesche, K.K. Unger, U. Esser, B. Eray, U. Trudinger, J. Gutenberg-universitit, J.N. Kinkel, R. Division, E. Merck, Packing technology, column bed structure and chromatographic performance of 1-2 um non-porous silicas in HPLC, J. Chromatogr. 465 (1989) 39–57.

[22] K.S. Rao, K. El-Hami, T. Kodaki, K. Matsushige, K. Makino, A novel method for synthesis of silica nanoparticles, J. Colloid Interface Sci. 289 (2005) 125–131. https://doi.org/10.1016/j.jcis.2005.02.019.

[23] D. Čakara, M. Kobayashi, M. Skarba, M. Borkovec, Protonation of silica particles in the presence of a strong cationic polyelectrolyte, Colloids Surfaces A Physicochem. Eng. Asp. 339 (2009) 20–25. https://doi.org/10.1016/j.colsurfa.2009.01.011.

[24] M.R. Buchmeiser, New synthetic ways for the preparation of high-performance liquid chromatography supports, J. Chromatogr. A. 918 (2001) 233–266. https://doi.org/10.1016/S0021-9673(00)00129-1.

[25] V.K. Langsi, B. a. Ashu-Arrah, J.D. Glennon, Sub-2-μm seeded growth mesoporous thin shell particles for high-performance liquid chromatography: synthesis, functionalisation and characterisation, J. Chromatogr. A. (2015). https://doi.org/10.1016/j.chroma.2015.04.034.

[26] R. Hayes, A. Ahmed, T. Edge, H. Zhang, Core-shell particles: Preparation, fundamentals and applications in high performance liquid chromatography, J. Chromatogr. A. 1357 (2014) 36–52. https://doi.org/10.1016/j.chroma.2014.05.010.

[27] J. Nawrocki, The silanol group and its role in liquid chromatography, J. Chromatogr. A. 779 (1997) 29–71. https://doi.org/10.1016/S0021-9673(97)00479-2.

[28] B. Sun, S. Pokhrel, D.R. Dunphy, H. Zhang, Z. Ji, X. Wang, M. Wang, Y.P. Liao, C.H. Chang, J. Dong, R. Li, L. Mädler, C.J. Brinker, A.E. Nel, T. Xia, Reduction of Acute Inflammatory Effects of Fumed Silica Nanoparticles in the Lung by Adjusting Silanol Display through Calcination and Metal Doping, ACS Nano. 9 (2015) 9357–9372. https://doi.org/10.1021/acsnano.5b03443.

[29] X. Li, D. Wu, J. Wang, W. Zhu, Y. Luo, C. Han, W. Ma, S. He, Synthesis of large-sized mesoporous silica spheres by pseudomorphic transformation of commercial silica spheres, Microporous Mesoporous Mater. 226 (2016) 309–315. https://doi.org/10.1016/j.micromeso.2016.02.010.

[30] X. Dong, Y. Wang, H. Dan, Z. Hong, K. Song, Q. Xian, Y. Ding, A facile route to synthesize mesoporous SBA-15 silica spheres from powder quartz, Mater. Lett. 204 (2017) 97–100. https://doi.org/10.1016/j.matlet.2017.05.115.

[31] J.S. Beck, J.C. Vartuli, W.J. Roth, M.E. Leonowicz, C.T. Kresge, K.D. Schmitt, C.T.-W. Chu, D.H. Olson, E.W. Sheppard, S.B. McCullen, J.B. Higgins, J.L. Schlenkert, A New Family of Mesoporous Molecular Sieves Prepared with Liquid Crystal Templates, J. Am.

Chem. Soc. (1992) 10834–10843.

[32] a Carlsson, M. Kaneda, Y. Sakamoto, O. Terasaki, R. Ryoo, S.H. Joo, The structure of MCM-48 determined by electron crystallography, J. Electron Microsc. (Tokyo). 48 (1999) 795–798. https://doi.org/10.1093/oxfordjournals.jmicro.a023751.

[33] D. Zhao, J. Feng, Q. Huo, N. Melosh, H. Glenn, B.F. Chmelka, G.D. Stucky, G.H. Fredrickson, F. Chmelka, Triblock Copolymer Syntheses of Mesoporous 50 to 300 Angstrom Silica with Periodic Pores, Science (80-. ). 279 (1998) 548–552.

[34] D. Zhao, Q. Huo, J. Feng, B.F. Chmelka, G.D. Stucky, Tri-, Tetra-, and Octablock Copolymer and Nonionic Surfactant Syntheses of Highly Ordered, Hydrothermally Stable, Mesoporous Silica Structures, J. Am. Chem. Soc. 120 (1998) 6024–6036.

[35] N. Rahmat, A.Z. Abdullah, A.R. Mohamed, A review: Mesoporous Santa Barbara amorphous-15, types, synthesis and its applications towards biorefinery production, Am. J. Appl. Sci. 7 (2010) 1579–1586. https://doi.org/10.3844/ajassp.2010.1579.1586.

[36] Y. Yin, Z.-F. Yang, Z.-H. Wen, A.-H. Yuan, X.-Q. Liu, Z.-Z. Zhang, H. Zhou, Modification of as Synthesized SBA-15 with Pt nanoparticles: Nanoconfinement Effects Give a Boost for Hydrogen Storage at Room Temperature, Sci. Rep. 7 (2017) 4509. https://doi.org/10.1038/s41598-017-04346-9.

[37] J.P. Thielemann, F. Girgsdies, R. Schlögl, C. Hess, Pore structure and surface area of silica SBA-15: influence of washing and scale-up, Beilstein J. Nanotechnol. 2 (2011) 110–118. https://doi.org/10.3762/bjnano.2.13.

[38] N. Rahmat, F. Hamzah, N. Sahiron, M. Mazlan, M.M. Zahari, Sodium silicate as source of silica for synthesis of mesoporous SBA-15, IOP Conf. Ser. Mater. Sci. Eng. 133 (2016). https://doi.org/10.1088/1757-899X/133/1/012011.

[39] T. Gong, Y. Li, H. Zhang, J. Zhou, G. Xie, B. Lei, J. Zhuang, Y. Liu, H. Zhang, Synthesis of SBA-15 with different morphologies for oxygen sensing, Microporous Mesoporous Mater. (2020) 110001. https://doi.org/10.1016/j.micromeso.2020.110001.

[40] P.T. Tanev, T.J. Pinnavaia, A neutral templating route to mesoporous molecular sieves, Science (80-. ). 267 (1995) 865–867.

[41] S. Chen, X. Zhang, Q. Han, M.Y. Ding, Synthesis of highly dispersed mesostructured cellular foam silica sphere and its application in high-performance liquid chromatography, Talanta. 101 (2012) 396–404. https://doi.org/10.1016/j.talanta.2012.09.047.

[42] Y. Han, S.S. Lee, J.Y. Ying, Siliceous mesocellular foam for high-performance liquid chromatography: Effect of morphology and pore structure, J. Chromatogr. A. 1217 (2010) 4337–4343. https://doi.org/10.1016/j.chroma.2010.04.041.

[43] X. Yan, L. Zhang, Y. Zhang, K. Qiao, Z. Yan, S. Komarneni, Amine-modified mesocellular silica foams for CO2 capture, Chem. Eng. J. 168 (2011) 918–924. https://doi.org/10.1016/j.cej.2011.01.066.

[44] Y. Zhang, J. Zhang, T. Jiang, S. Wang, Inclusion of the poorly water-soluble drug simvastatin in mesocellular foam nanoparticles: Drug loading and release properties, Int. J. Pharm. 410 (2011) 118–124. https://doi.org/10.1016/j.ijpharm.2010.07.040.

[45] T. Yanagisawa, T. Shimizu, K. Kuroda, C. Kato, The preparation of alkyltrimethylammonium-kanemite complexes and their conversion to microporous materials, Bull. Chem. Soc. Jpn. 63 (1990) 988–992. https://doi.org/10.1246/bcsj.63.988.

[46] E. Da'na, Adsorption of heavy metals on functionalized-mesoporous silica: A review, Microporous Mesoporous Mater. 247 (2017) 145–157. https://doi.org/10.1016/j.micromeso.2017.03.050.

[47] J.A. Schwarz, C.I. Contescu, Surfaces of Nanoparticles and Porous Materials (Google eBook), 1999. https://doi.org/doi:10.1201/9780824746681.fmatt.

[48] G. Guiochon, Advances and Perspectives in Liquid Chromatography, 1980.

[49] M. Thommes, R. Köhn, M. Fröba, Sorption and pore condensation behavior of pure fluids in mesoporous MCM-48 silica, MCM-41 silica, SBA-15 silica and controlled-pore glass at temperatures above and below the bulk triple point, Appl. Surf. Sci. 196 (2002) 239–249. https://doi.org/10.1016/S0169-4332(02)00062-4.

[50] P. Zucca, E. Sanjust, Inorganic Materials as Supports for Covalent Enzyme Immobilization: Methods and Mechanisms, Molecules. 19 (2014) 14139–14194. https://doi.org/10.3390/molecules190914139.

[51] Ö. Alptekin, S.S. Tükel, D. Yildirim, D. Alagöz, Characterization and properties of catalase immobilized onto controlled pore glass and its application in batch and plug-flow type reactors, J. Mol. Catal. B Enzym. 58 (2009) 124–131. https://doi.org/10.1016/j.molcatb.2008.12.004.

[52] K.K. Unger, Porous Silica Its Properties and Use as Support in Column Liquid Chromatography, Elsevier, 1979.

[53] T.J. Tranter, A.S. Aloy, N. V. Sapozhnikova, D.A. Knecht, T.A. Todd, Porous crystalline silica (Gubka) as a inorganic support matrix for novel sorbents, Mater. Res. Soc. Symp. - Proc. 713 (2002) 907–913. https://doi.org/10.1557/proc-713-jj11.68.

[54] J. Wang, H. Ge, W. Bao, Synthesis and characteristics of SBA-15 with thick pore wall and high hydrothermal stability, Mater. Lett. 145 (2015) 312–315. https://doi.org/10.1016/j.matlet.2015.01.113.

[55] C. T. Kresge, M.E. Leonowicz, W.J. Roth, J.C. Vartuli, J.S. Beck, Ordered mesoporous

molecular sieves synthesizeed by a liquid-crystal template mechanism, Nature. 359 (1992) 710–713.

[56] C.F. Pirri, G. Material, M. Masi, C. Cavallotti, W. Henrion, A. Roseler, S. Agnello, R. Boscaino, M. Cannas, M. Cazzanelli, L. Pavesi, C.A. Dimitriadis, Silicon Based Materials and Devices., n.d.

[57] G.E. Maciel, D.W. Sindorf, Silicon-29 Nuclear Magnetic Resonance Study of the Surface of Silica Gel by Cross Polarization and Magic-Angle Spinning, J. Am. Chem. Soc. 102 (1980) 7606–7607. https://doi.org/10.1021/ja00545a056.

[58] H. Bergna, W. Roberts, Colloidal Silica: Fundamentals and Applications, CRC Press Taylor & Francis Group, 2007. papers2://publication/uuid/5C5D42D6-7FC8-488A-AB81-151CFB1FF4A9.

[59] L.T. Zhuravlev, Concentration of hydroxyl groups on the surface of amorphous silicas, Langmuir. 3 (1987) 316–318. https://doi.org/10.1021/la00075a004.

[60] L.T. Zhuravlev, V. V. Potapov, Density of silanol groups on the surface of silica precipitated from a hydrothermal solution, Russ. J. Phys. Chem. A. 80 (2006) 1119–1128. https://doi.org/10.1134/S0036024406070211.

[61] S. Ong, X. Zhao, K.B. Eisenthal, Polarization of water molecules at a charged interface: second harmonic studies of the silica/water interface, Chem. Phys. Lett. 191 (1992) 327–335. https://doi.org/10.1016/0009-2614(92)85309-X.

[62] V. Dugas, Y. Chevalier, Surface hydroxylation and silane grafting on fumed and thermal silica, J. Colloid Interface Sci. 264 (2003) 354–361. https://doi.org/10.1016/S0021-9797(03)00552-6.

[63] L.T. Zhuravlev, The surface chemistry of amorphous silica. Zhuravlev model, Colloids

Surfaces A Physicochem. Eng. Asp. 173 (2000) 1–38. https://doi.org/10.1016/S0927-7757(00)00556-2.

[64] A.A. Christy, The nature of silanol groups on the surfaces of silica, modified silica and some silica based materials, Adv. Mater. Res. 998–999 (2014) 3–10. https://doi.org/10.4028/www.scientific.net/AMR.998-999.3.

[65] A.A. Christy, The nature of rest silanol groups on the surfaces of silica based solid phase extraction materials, Adv. Mater. Res. 650 (2013) 66–71. https://doi.org/10.4028/www.scientific.net/AMR.650.66.

[66] B. Grünberg, T. Emmler, E. Gedat, I. Shenderovich, G.H. Findenegg, H.H. Limbach, G. Buntkowsky, Hydrogen bonding of water confined in mesoporous silica MCM-41 and SBA-15 studied by 1H solid-state NMR, Chem. - A Eur. J. 10 (2004) 5689–5696. https://doi.org/10.1002/chem.200400351.

[67] N. Gartmann, C. Schütze, H. Ritter, D. Brühwiler, The effect of water on the functionalization of mesoporous silica with 3-aminopropyltriethoxysilane, J. Phys. Chem. Lett. 1 (2010) 379–382. https://doi.org/10.1021/jz9002795.

[68] N. Gartmann, D. Brühwiler, Functional group distributions on mesoporous silica, Chimia (Aarau). 65 (2011) 250–252. https://doi.org/10.2533/chimia.2011.250.

[69] F. Bauer, S. Czihal, M. Bertmer, U. Decker, S. Naumov, S. Wassersleben, D. Enke, Water-based functionalization of mesoporous siliceous materials, Part 1: Morphology and stability of grafted 3-aminopropyltriethoxysilane, Microporous Mesoporous Mater. 250 (2017) 221–231. https://doi.org/10.1016/j.micromeso.2016.01.046.

[70] J. Kim, P. Seidler, L.S. Wan, C. Fill, Formation, structure, and reactivity of amino-terminated organic films on silicon substrates, J. Colloid Interface Sci. 329 (2009) 114–

119. https://doi.org/10.1016/j.jcis.2008.09.031.

[71] F. Bernardoni, A.Y. Fadeev, Adsorption and wetting characterization of hydrophobic SBA-15 silicas, J. Colloid Interface Sci. 356 (2011) 690–698. https://doi.org/10.1016/j.jcis.2011.01.033.

[72] P. Borowicz, M. Latek, W. Rzodkiewicz, A. Łaszcz, A. Czerwinski, J. Ratajczak, Deep-ultraviolet Raman investigation of silicon oxide: Thin film on silicon substrate versus bulk material, Adv. Nat. Sci. Nanosci. Nanotechnol. 3 (2012). https://doi.org/10.1088/2043-6262/3/4/045003.

[73] J. McMurry, Organic Chemistry, Eighth, 2012. https://doi.org/10.1016/B0-08-043751-6/08302-X.

[74] C.J. Brinker, R. Sehgal, S.L. Hietala, R. Deshpande, D.M. Smith, D. Loy, C.S. Ashley, Sol-gel strategies for controlled porosity inorganic materials, J. Memb. Sci. 94 (1994) 85–102. https://doi.org/10.1016/0376-7388(93)E0129-8.

[75] N.S.K. Gunda, M. Singh, L. Norman, K. Kaur, S.K. Mitra, Optimization and characterization of biomolecule immobilization on silicon substrates using (3-aminopropyl)triethoxysilane (APTES) and glutaraldehyde linker, Appl. Surf. Sci. 305 (2014) 522–530. https://doi.org/10.1016/j.apsusc.2014.03.130.

[76] A. Stein, Advances in microporous and mesoporous solids - Highlights of recent progress, Adv. Mater. 15 (2003) 763–775. https://doi.org/10.1002/adma.200300007.

[77] D. Kim, A.E. Herr, Protein immobilization techniques for microfluidic assays, Biomicrofluidics. 7 (2013) 1–47. https://doi.org/10.1063/1.4816934.

[78] M. Zhu, M.Z. Lerum, W. Chen, How to Prepare Reproducible, Homogeneous, and Hydrolytically Stable Aminosilane-derived Layers on Silica, Langmuir. 23 (2012) 416–

423. https://doi.org/10.1021/la203638g.

[79] D. Harris, Quantitative Chemical Analysis, 2007. http://www.amazon.com/dp/0716761254.

[80] J. Rużyłło, Electrochemical Society. Electronics Division., F. Electrochemical Society. Meeting (192nd : 1997 : Paris, Cleaning Technology in Semiconductor Device Manufacturing, 1998.

[81] L. Nováková, H. Vlčková, A review of current trends and advances in modern bio-analytical methods: Chromatography and sample preparation, Anal. Chim. Acta. 656 (2009) 8–35. https://doi.org/10.1016/j.aca.2009.10.004.

[82] I. Novak, D. Berek, B. Buszewski, J. Garaj, Influence of pore structure of silica packing on HPLC column characteristics, Chem. Pap. 44 (1990).

[83] V. Udayakumar, A. Pandurangan, Synthesis of Hf / SBA-15 Lewis acid catalyst for converting glycerol to value- added chemicals Synthesis of Hf / SBA-15 Lewis acid catalyst for converting glycerol to value-added chemicals, J. Porous Mater. (2016). https://doi.org/10.1007/s10934-016-0337-2.

[84] H. Zhang, J. Sun, D. Ma, G. Weinberg, D.S. Su, X. Bao, Engineered complex emulsion system: Toward modulating the pore length and morphological architecture of mesoporous silicas, J. Phys. Chem. B. 110 (2006) 25908–25915. https://doi.org/10.1021/jp065760w.

[85] A. Liberman, N. Mendez, W.C. Trogler, A.C. Kummel, Synthesis and surface functionalization of silica nanoparticles for nanomedicine, Surf. Sci. Rep. 69 (2014) 132–158. https://doi.org/10.1016/j.surfrep.2014.07.001.

[86] S. Jun, Sang Hoon Joo, R. Ryoo, M. Kruk, M. Jaroniec, Z. Liu, T. Ohsuna, O. Terasaki, Synthesis of new, nanoporous carbon with hexagonally ordered mesostructure [5], J. Am.

Chem. Soc. 122 (2000) 10712–10713. https://doi.org/10.1021/ja002261e.

[87] B. Gouze, J. Cambedouzou, S. Parrès-Maynadié, D. Rébiscoul, How hexagonal mesoporous silica evolves in water on short and long term: Role of pore size and silica wall porosity, Microporous Mesoporous Mater. 183 (2014) 168–176. https://doi.org/10.1016/j.micromeso.2013.08.041.

[88] V. González-Ruiz, A.I. Olives, M.A. Martín, Core-shell particles lead the way to renewing high-performance liquid chromatography, TrAC - Trends Anal. Chem. 64 (2015) 17–28. https://doi.org/10.1016/j.trac.2014.08.008.

[89] J.O. Omamogho, J.P. Hanrahan, J. Tobin, J.D. Glennon, Structural variation of solid core and thickness of porous shell of 1.7μm core-shell silica particles on chromatographic performance: Narrow bore columns, J. Chromatogr. A. 1218 (2011) 1942–1953. https://doi.org/10.1016/j.chroma.2010.11.067.

[90] P.P. Ghimire, M. Jaroniec, Renaissance of Stöber method for synthesis of colloidal particles: New developments and opportunities, J. Colloid Interface Sci. 584 (2021) 838–865. https://doi.org/10.1016/j.jcis.2020.10.014.

[91] R. Aelion, A. Loebel, F. Eirich, The hydrolysis and polycondensation of tetra alkoxysilanes, Recl. Des Trav. Chim. Des Pays-Bas. 69 (1950) 61–75. https://doi.org/10.1002/recl.19500690109.

[92] R. Aelion, A. Loebel, F. Eirich, Hydrolysis of Ethyl Silicate, J. Am. Chem. Soc. 72 (1950) 5705–5712. https://doi.org/10.1021/ja01168a090.

[93] C. Brinker, G. Scherer, Sol-gel science: the physics and chemistry of sol-gel processing, (1990).

[94] R.K. Iler, The Chemistry of Silica, John Wiley & Sons, Ltd., 1979.

[95] L. Hench, Sol- Gel Silica, 1998.

[96] D. a. Keane, J.P. Hanrahan, M.P. Copley, J.D. Holmes, M. a. Morris, A modified Stober process for the production of mesoporous Sub 2 micron silica microspheres; Applications in HPLC, J. Porous Mater. 17 (2010) 145–152. https://doi.org/10.1007/s10934-009-9274-7.

[97] N. Shimura, M. Ogawa, Growth of nanoporous silica spherical particles by the Stöber method combined with supramolecular templating approach, Bull. Chem. Soc. Jpn. 78 (2005) 1154–1159. https://doi.org/10.1246/bcsj.78.1154.

[98] E.J.. Pope, J.D. Mackenzie, Sol-Gel Processing of Silica II. The role of the catalyst, J. Non. Cryst. Solids. 87 (1986) 185–198. https://doi.org/10.1016/S0022-3093(86)80078-3.

[99] R.A. Assink, B.D. Kay, Sol-gel kinetics I. Functional group kinetics, J. Non. Cryst. Solids. 99 (1988) 359–370. https://doi.org/10.1016/0022-3093(88)90441-3.

[100] C.Y. Chen, S.L. Burkett, H.X. Li, M.E. Davis, Studies on mesoporous materials II. Synthesis mechanism of MCM-41, Microporous Mater. 2 (1993) 27–34. https://doi.org/10.1016/0927-6513(93)80059-4.

[101] Z.A. Alothman, A review: Fundamental aspects of silicate mesoporous materials, Materials (Basel). 5 (2012) 2874–2902. https://doi.org/10.3390/ma5122874.

[102] J. Sangeetha, S. Asokan, Mesoporous Silica: A Review, Int. J. Pharm. Drug Anal. 6 (2018) 1–12.

[103] S. Kumar, M.M. Malik, R. Purohit, Synthesis Methods of Mesoporous Silica Materials, Mater. Today Proc. 4 (2017) 350–357. https://doi.org/10.1016/j.matpr.2017.01.032.

[104] A. Corma, Q. Kan, M.T. Navarro, J. Pérez-Pariente, F. Rey, Synthesis of MCM-41 with

Different Pore Diameters without Addition of Auxiliary Organics, Chem. Mater. 9 (1997) 2123–2126. https://doi.org/10.1021/cm970203v.

[105] G.S. Attard, J.C. Glyde, C.G. Goltner, Liquid-crystalline phases as templates for the synthesis of mesoporous silica, Nature. 2 (1995) 75–8. https://doi.org/https://doi.org/10.1038/378366a0.

[106] S. Ruthstein, V. Frydman, S. Kababya, M. Landau, D. Goldfarb, Study of the Formation of the Mesoporous Material SBA-15 by EPR Spectroscopy, J. Phys. Chem. B. 107 (2003) 1739–1748. https://doi.org/10.1021/jp021964a.

[107] A. Katiyar, S. Yadav, P.G. Smirniotis, N.G. Pinto, Synthesis of ordered large pore SBA-15 spherical particles for adsorption of biomolecules, J. Chromatogr. A. 1122 (2006) 13–20. https://doi.org/10.1016/j.chroma.2006.04.055.

[108] Y. Chen, H. Chen, L. Guo, Q. He, F. Chen, J. Zhou, J. Feng, J. Shi, Hollow/rattle-type mesoporous nanostructures by a structural difference-based selective etching strategy, ACS Nano. 4 (2010) 529–539. https://doi.org/10.1021/nn901398j.

[109] H. Zhang, Y. Zhou, Y. Li, T.J. Bandosz, D.L. Akins, Synthesis of hollow ellipsoidal silica nanostructures using a wet-chemical etching approach, J. Colloid Interface Sci. 375 (2012) 106–111. https://doi.org/10.1016/j.jcis.2012.02.046.

[110] C. Rosu, A.J. Gorman, R. Cueto, K.M. Dooley, P.S. Russo, Sculpting the internal architecture of fluorescent silica particles via a template-free approach, J. Colloid Interface Sci. 467 (2016) 321–334. https://doi.org/10.1016/j.jcis.2016.01.007.

[111] M. Hiraoui, M. Guendouz, N. Lorrain, A. Moadhen, L. Haji, M. Oueslati, Spectroscopy studies of functionalized oxidized porous silicon surface for biosensing applications, Mater. Chem. Phys. 128 (2011) 151–156.

https://doi.org/10.1016/j.matchemphys.2011.02.052.

[112] M. Lazghab, K. Saleh, P. Guigon, Functionalisation of porous silica powders in a fluidised-bed reactor with glycidoxypropyltrimethoxysilane (GPTMS) and aminopropyltriethoxysilane (APTES), Chem. Eng. Res. Des. 88 (2010) 686–692. https://doi.org/10.1016/j.cherd.2009.11.005.

[113] X. Wang, L. Chen, Q. Guo, Development of hybrid amine-functionalized MCM-41 sorbents for CO2capture, Chem. Eng. J. 260 (2015) 573–581. https://doi.org/10.1016/j.cej.2014.08.107.

[114] M. Shen, H. Cai, X. Wang, X. Cao, K. Li, S.H. Wang, R. Guo, L. Zheng, G. Zhang, X. Shi, Facile one-pot preparation, surface functionalization, and toxicity assay of APTS-coated iron oxide nanoparticles, Nanotechnology. 23 (2012) 105601. https://doi.org/10.1088/0957-4484/23/10/105601.

[115] R. Kishor, A.K. Ghoshal, Amine-Modified Mesoporous Silica for CO2 Adsorption: The Role of Structural Parameters, Ind. Eng. Chem. Res. 56 (2017) 6078–6087. https://doi.org/10.1021/acs.iecr.7b00890.

[116] N. Hiyoshi, K. Yogo, T. Yashima, Adsorption characteristics of carbon dioxide on organically functionalized SBA-15, Microporous Mesoporous Mater. 84 (2005) 357–365. https://doi.org/10.1016/j.micromeso.2005.06.010.

[117] V.D. Hoang, T.P. Dang, Q.K. Dinh, H.P. Nguyen, A.T. Vu, The synthesis of novel hybrid thiol-functionalized nano-structured SBA-15, Adv. Nat. Sci. Nanosci. Nanotechnol. 1 (2010). https://doi.org/10.1088/2043-6262/1/3/035011.

[118] P.F. Siril, N.R. Shiju, D.R. Brown, K. Wilson, Optimising catalytic properties of supported sulfonic acid catalysts, Appl. Catal. A Gen. 364 (2009) 95–100.

https://doi.org/10.1016/j.apcata.2009.05.032.

[119] N. Zucchetto, D. Brühwiler, Strategies for Localizing Multiple Functional Groups in Mesoporous Silica Particles through a One-Pot Synthesis, Chem. Mater. 30 (2018) 7280–7286. https://doi.org/10.1021/acs.chemmater.8b03603.

[120] U.L.F. Bexell, Surface Characterisation Using ToF-SIMS, AES and XPS of Silane Films and Organic Coatings Deposited on Metal Substrates, 2003. http://uu.diva-portal.org/smash/get/diva2:162811/FULLTEXT01.

[121] J. Liu, X. Feng, G.E. Fryxell, L.Q. Wang, A.Y. Kim, K.M. Kemner, Functionalized monolayers on ordered mesoporous supports, Science (80-. ). 276 (1997) 923–926. https://doi.org/10.1126/science.276.5314.923.

[122] K.K. Sharma, A. Anan, R.P. Buckley, W. Ouellette, T. Asefa, Toward efficient nanoporous catalysts: Controlling site-isolation and concentration of grafted catalytic sites on nanoporous materials with solvents and colorimetric elucidation of their site-isolation, J. Am. Chem. Soc. 130 (2008) 218–228. https://doi.org/10.1021/ja074128t.

[123] B. Lee, Y. Kim, H. Lee, J. Yi, Synthesis of functionalized porous silicas via templating method as heavy metal ion adsorbents: The introduction of surface hydrophilicity onto the surface of adsorbents, Microporous Mesoporous Mater. 50 (2001) 77–90. https://doi.org/10.1016/S1387-1811(01)00437-1.

[124] T. Materne, F. de Buyl, G.L. Witucki, Organosilane Technology in Coating Applications : Review and Perspectives, Dow Corning. (2012) 1–16. https://doi.org/10.1017/CBO9781107415324.004.

[125] F. Sevimli, A. Yilmaz, Surface functionalization of SBA-15 particles for amoxicillin delivery, Microporous Mesoporous Mater. 158 (2012) 281–291.

https://doi.org/10.1016/j.micromeso.2012.02.037.

[126] H. Chaudhuri, S. Dash, A. Sarkar, SBA-15 functionalised with high loading of amino or carboxylate groups as selective adsorbent for enhanced removal of toxic dyes from aqueous solution, New J. Chem. 40 (2016) 3622–3634. https://doi.org/10.1039/c5nj02816g.

[127] N. Tanaka, K. Kimata, K. Iwaguchi, S. Onishi, K. Jinno, R. Eksteen, K. Hosoya, M. Araki, Chromatographic Characterization of Silica C18 Packing Materials. Correlation between a Preparation Method and Retention Behavior of Stationary Phase, J. Chromatogr. Sci. 27 (1989) 721–728. https://doi.org/10.1093/chromsci/27.12.721.

[128] J.D. Sunseri, W.T. Cooper, J.G. Dorsey, Reducing residual silanol interactions in reversed-phase liquid chromatography: Thermal treatment of silica before derivatization, J. Chromatogr. A. 1011 (2003) 23–29. https://doi.org/10.1016/S0021-9673(03)01070-7.

[129] H. Minakuchi, K. Nakanishi, N. Soga, N. Ishizuka, N. Tanaka, Octadecylsilylated porous silica rods as separation media for reversed-phase liquid chromatography., Anal. Chem. 68 (1996) 3498–3501. https://doi.org/10.1021/ac960281m.

[130] L. Yang, Y. Wang, G. Luo, Y. Dai, Preparation and functionalization of mesoporous silica spheres as packing materials for HPLC, Particuology. 6 (2008) 143–148. https://doi.org/10.1016/j.partic.2008.03.006.

[131] N.M. Scully, L.O. Healy, T. O'Mahony, J.D. Glennon, B. Dietrich, K. Albert, Effect of silane reagent functionality for fluorinated alkyl and phenyl silica bonded stationary phases prepared in supercritical carbon dioxide, J. Chromatogr. A. 1191 (2008) 99–107. https://doi.org/10.1016/j.chroma.2008.02.052.

[132] E.M. Borges, M.R. Euerby, An appraisal of the chemical and thermal stability of silica based reversed-phase liquid chromatographic stationary phases employed within the

pharmaceutical environment, J. Pharm. Biomed. Anal. 77 (2013) 100–115. https://doi.org/10.1016/j.jpba.2013.01.013.

[133] D. Brühwiler, Postsynthetic functionalization of mesoporous silica., Nanoscale. 2 (2010) 887–892. https://doi.org/10.1039/c0nr00039f.

[134] L. Gabrielli, L. Russo, A. Poveda, J.R. Jones, F. Nicotra, J. Jiménez-Barbero, L. Cipolla, Epoxide opening versus silica condensation during sol-gel hybrid biomaterial synthesis, Chem. - A Eur. J. 19 (2013) 7856–7864. https://doi.org/10.1002/chem.201204326.

[135] H. Yang, X. Lu, Z. Xin, Facile Fabrication of Lilium Pollen-like Organosilica Particles, Langmuir. 36 (2020) 571–575. https://doi.org/10.1021/acs.langmuir.9b02627.

[136] F. Branda, B. Silvestri, G. Luciani, A. Costantini, The effect of mixing alkoxides on the Stöber particles size, Colloids Surfaces A Physicochem. Eng. Asp. 299 (2007) 252–255. https://doi.org/10.1016/j.colsurfa.2006.11.048.

[137] M. Dulski, M. Laskowska, S. Sułowicz, T. Krzykawski, O. Pastukh, P.M. Zieliński, P. Pawlik, A. Nowak, Ł. Laskowski, The impact of the functionalization of silica mesopores on the structural and biological features of SBA-15, Microporous Mesoporous Mater. (2020) 110453. https://doi.org/10.1016/j.micromeso.2020.110453.

[138] J. a. Melero, G.D. Stucky, R. van Grieken, G. Morales, Direct syntheses of ordered SBA-15 mesoporous materials containing arenesulfonic acid groups, J. Mater. Chem. 12 (2002) 1664–1670. https://doi.org/10.1039/b110598c.

[139] R. Dobrowolski, M. Oszust-Cieniuch, J. Dobrzyńska, M. Barczak, Amino-functionalized SBA-15 mesoporous silicas as sorbents of platinum (IV) ions, Colloids Surfaces A Physicochem. Eng. Asp. 435 (2013) 63–70. https://doi.org/10.1016/j.colsurfa.2012.12.001.

[140] M. Jafarzadeh, I.A. Rahman, C.S. Sipaut, Optical properties of amorphous organo-modified silica nanoparticles produced via co-condensation method, Ceram. Int. 36 (2010) 333–338. https://doi.org/10.1016/j.ceramint.2009.09.010.

[141] A. Vinu, K.Z. Hossain, K. Ariga, Recent advances in functionalization of mesoporous silica., J. Nanosci. Nanotechnol. 5 (2005) 347–371. https://doi.org/10.1166/jnn.2005.089.

[142] P. Yang, Z. Quan, C. Li, H. Lian, S. Huang, J. Lin, Fabrication, characterization of spherical CaWO4:Ln @MCM-41(Ln = Eu3+, Dy3+, Sm3+, Er3+) composites and their applications as drug release systems, Microporous Mesoporous Mater. 116 (2008) 524–531. https://doi.org/10.1016/j.micromeso.2008.05.016.

[143] B. Buszewski, L. Nondek, A. Jurášek, D. Berek, Preparation of silanized silica with high ligand density. The effect of silane structure, Chromatographia. 23 (1987) 442–446. https://doi.org/10.1007/BF02311822.

[144] B. Buszewski, A. Jurášek, J. Garaj, L. Nondek, I. Novak, D. Berek, The Effect of the Reaction Medium on the Coverage Density of C 18 Chemically Bonded Phase, J. Liq. Chromatogr. (2006) 2325–2336.

[145] X.S. Zhao, G.Q. Lu, a K. Whittaker, G.J. Millar, H.Y. Zhu, Comprehensive study of surface chemistry of MCM-41 using Si-29 CP/MAS NMR, FTIR, pyridine-TPD, and TGA, J. Phys. Chem. B. 101 (1997) 6525–6531. https://doi.org/10.1021/jp971366+.

[146] C.H. Lochmuller, M.T. Kersey, Effect of Thermal Pretreatment on the Surface Reactivity, Langmuir. 4 (1988) 572–578. https://doi.org/10.1021/la00081a013.

[147] J. Zou, S.M. Kauzlarich, Functionalization of silicon nanoparticles via silanization: Alkyl, halide and ester, J. Clust. Sci. 19 (2008) 341–355. https://doi.org/10.1007/s10876-008-0182-9.

[148] N. Gartmann, D. Brühwiler, Controlling and Imaging the Functional-Group Distribution on Mesoporous Silica, Angew. Chemie Int. Ed. 48 (2009) 6354–6356. https://doi.org/10.1002/anie.200902436.

[149] N. Majoul, S. Aouida, B. Bessaïs, Progress of porous silicon APTES-functionalization by FTIR investigations, Appl. Surf. Sci. 331 (2015) 388–391. https://doi.org/10.1016/j.apsusc.2015.01.107.

[150] J. Kim, P. Seidler, C. Fill, L.S. Wan, Investigations of the effect of curing conditions on the structure and stability of amino-functionalized organic films on silicon substrates by Fourier transform infrared spectroscopy, ellipsometry, and fluorescence microscopy, Surf. Sci. 602 (2008) 3323–3330. https://doi.org/10.1016/j.susc.2008.09.001.

[151] C. Cummins, M.T. Shaw, M.A. Morris, Area Selective Polymer Brush Deposition, Macromol. Rapid Commun. 38 (2017) 1–6. https://doi.org/10.1002/marc.201700252.

[152] R. Lundy, P. Yadav, N. Prochukhan, E.C. Giraud, T.F. O'Mahony, A. Selkirk, E. Mullen, J. Conway, M. Turner, S. Daniels, P.G. Mani-Gonzalez, M. Snelgrove, J. Bogan, C. McFeely, R. O'Connor, E. McGlynn, G. Hughes, C. Cummins, M.A. Morris, Precise Definition of a "monolayer Point" in Polymer Brush Films for Fabricating Highly Coherent TiO2Thin Films by Vapor-Phase Infiltration, Langmuir. 36 (2020) 12394–12402. https://doi.org/10.1021/acs.langmuir.0c02512.

[153] R. Lundy, P. Yadav, A. Selkirk, E. Mullen, T. Ghoshal, C. Cummins, M.A. Morris, R. Lundy, P. Yadav, A. Selkirk, E. Mullen, T. Ghoshal, C. Cummins, Optimizing polymer brush coverage to develop highly coherent sub-5nm oxide films by ion inclusion Optimizing polymer brush coverage to develop highly coherent sub- 5nm oxide films by ion inclusion, Chem. Mater. (2019). https://doi.org/10.1021/acs.chemmater.9b02856.

[154] M.E. Vlachopoulou, A. Tserepi, P. Pavli, P. Argitis, M. Sanopoulou, K. Misiakos, A low

temperature surface modification assisted method for bonding plastic substrates, J. Micromechanics Microengineering. 19 (2009). https://doi.org/10.1088/0960-1317/19/1/015007.

[155] A. Taguchi, F. Schüth, Ordered mesoporous materials in catalysis, 2005. https://doi.org/10.1016/j.micromeso.2004.06.030.

[156] D. Kryszak, K. Stawicka, M. Trejda, V. Calvino-Casilda, R. Martin-Aranda, M. Ziolek, Development of basicity in mesoporous silicas and metallosilicates, Catal. Sci. Technol. 7 (2017) 5236–5248. https://doi.org/10.1039/c7cy00927e.

[157] U. Junges, W. Jacobs, I. Voigt-Martin, B. Krutzsch, F. Schüth, MCM-41 as a support for small platinum particles: A catalyst for low-temperature carbon monoxide oxidation, J. Chem. Soc. Chem. Commun. (1995) 2283–2284. https://doi.org/10.1039/C39950002283.

[158] A. Lewandowska, S. Monteverdi, M. Bettahar, M. Ziolek, MCM-41 mesoporous molecular sieves supported nickel - Physico-chemical properties and catalytic activity in hydrogenation of benzene, J. Mol. Catal. A Chem. 188 (2002) 85–95. https://doi.org/10.1016/S1381-1169(02)00339-4.

[159] C.M. Yang, M. Kalwei, F. Schüth, K.J. Chao, Gold nanoparticles in SBA-15 showing catalytic activity in CO oxidation, Appl. Catal. A Gen. 254 (2003) 289–296. https://doi.org/10.1016/S0926-860X(03)00490-3.

[160] M.Á. Aramendía, V. Borau, C. Jiménez, J.M. Marinas, F.J. Romero, Supramolecular templated synthesis of platinum-supported silica, Chem. Commun. (1999) 873–874. https://doi.org/10.1039/a901924c.

[161] I. Agirrezabal-Telleria, J. Requies, M.B. Güemez, P.L. Arias, Pore size tuning of functionalized SBA-15 catalysts for the selective production of furfural from xylose, Appl.

Catal. B Environ. 115–116 (2012) 169–178. https://doi.org/10.1016/j.apcatb.2011.12.025.

[162] A.J. Crisci, M.H. Tucker, M. Lee, S.G. Jang, J.A. Dumesic, S.L. Scott, Acid-Functionalized SBA-15-Type Silica Catalysts for Carbohydrate Dehydration, ACS Catal. 1 (2011) 719–728. https://doi.org/10.1021/cs2001237.

[163] A.L.T. Pham, D.L. Sedlak, F.M. Doyle, Dissolution of mesoporous silica supports in aqueous solutions: Implications for mesoporous silica-based water treatment processes, Appl. Catal. B Environ. 126 (2012) 258–264. https://doi.org/10.1016/j.apcatb.2012.07.018.

[164] V.H.A. Pinto, J.S. Rebouças, G.M. Ucoski, E.H. de Faria, B.F. Ferreira, R.A. Silva San Gil, S. Nakagaki, Mn porphyrins immobilized on non-modified and chloropropyl-functionalized mesoporous silica SBA-15 as catalysts for cyclohexane oxidation, Appl. Catal. A Gen. 526 (2016) 9–20. https://doi.org/10.1016/j.apcata.2016.07.018.

[165] A. Najafian, R. Rahimi, S. Zargari, M. Mahjoub-Moghaddas, A. Nazemi, Synthesis and photocatalytic activity of V-doped mesoporous TiO2 photosensitized with porphyrin supported by SBA-15, Res. Chem. Intermed. 42 (2016) 3441–3458. https://doi.org/10.1007/s11164-015-2222-z.

[166] R.J. Kalbasi, F. Zamani, Synthesis and characterization of Ni nanoparticles incorporated into hyperbranched polyamidoamine-polyvinylamine/SBA-15 catalyst for simple reduction of nitro aromatic compounds, RSC Adv. 4 (2014) 7444–7453. https://doi.org/10.1039/c3ra44662j.

[167] L.D. Zanatta, I.A. Barbosa, F.B. Zanardi, P.C. De Sousa Filho, L.B. Bolzon, A.P. Ramos, O.A. Serra, Y. Iamamoto, Hydrocarbon oxidation by iron-porphyrin immobilized on SBA-15 as biomimetic catalyst: Role of silica surface, RSC Adv. 6 (2016) 104886–104896. https://doi.org/10.1039/c6ra18395f.

[168] S. Sadjadi, M.M. Heravi, Current advances in the utility of functionalized SBA mesoporous silica for developing encapsulated nanocatalysts: State of the art, RSC Adv. 7 (2017) 30815–30838. https://doi.org/10.1039/c7ra04833e.

[169] H.H.P. Yiu, P.A. Wright, Enzymes supported on ordered mesoporous solids: a special case of an inorganic–organic hybrid, J. Mater. Chem. 15 (2005) 3690. https://doi.org/10.1039/b506090g.

[170] S. Datta, L.R. Christena, Y.R.S. Rajaram, Enzyme immobilization: an overview on techniques and support materials, 3 Biotech. (2012) 1–9. https://doi.org/10.1007/s13205-012-0071-7.

[171] Z. Zhao, X. Xie, Z. Wang, Y. Tao, X. Niu, X. Huang, L. Liu, Z. Li, Immobilization of Lactobacillus rhamnosus in mesoporous silica-based material: An efficiency continuous cell-recycle fermentation system for lactic acid production, J. Biosci. Bioeng. 121 (2016) 645–651. https://doi.org/10.1016/j.jbiosc.2015.11.010.

[172] M. Dezott, L.H. Innocentini-Mei, N. Durán, Silica immobilized enzyme catalyzed removal of chlorolignins from eucalyptus kraft effluent, J. Biotechnol. 43 (1995) 161–167. https://doi.org/10.1016/0168-1656(95)00110-7.

[173] S.M.L. Dos Santos, K.A.B. Nogueira, M. De Souza Gama, J.D.F. Lima, I.J. Da Silva Júnior, D.C.S. De Azevedo, Synthesis and characterization of ordered mesoporous silica (SBA-15 and SBA-16) for adsorption of biomolecules, Microporous Mesoporous Mater. 180 (2013) 284–292. https://doi.org/10.1016/j.micromeso.2013.06.043.

[174] S.K. Vashist, E. Lam, S. Hrapovic, K.B. Male, J.H.T. Luong, Immobilization of antibodies and enzymes on 3-aminopropyltriethoxysilane-functionalized bioanalytical platforms for biosensors and diagnostics, Chem. Rev. 114 (2014) 11083–11130. https://doi.org/10.1021/cr5000943.

[175] N. Aissaoui, L. Bergaoui, J. Landoulsi, P. Vi, Silane Layers on Silicon Surfaces : Mechanism of Interaction , Stability , and Influence on Protein Adsorption, Langmuir. (2012) 656–665. https://doi.org/10.1021/la2036778.

[176] P.K. Jal, S. Patel, B.K. Mishra, Chemical modification of silica surface by immobilization of functional groups for extractive concentration of metal ions, Talanta. 62 (2004) 1005–1028. https://doi.org/10.1016/j.talanta.2003.10.028.

[177] L. Mercier, T.J. Pinnavaia, Access in Mesoporous Materials: Advantages of a Uniform Pore Structure in the Design of a Heavy Metal Ion Adsorbent for Environmental Remediation, Adv. Mater. 6 (1997) 500–503. https://doi.org/10.1186/1556-276X-6-107.

[178] S. Hao, A. Verlotta, P. Aprea, F. Pepe, D. Caputo, W. Zhu, Optimal synthesis of amino-functionalized mesoporous silicas for the adsorption of heavy metal ions, Microporous Mesoporous Mater. 236 (2016) 250–259. https://doi.org/10.1016/j.micromeso.2016.09.008.

[179] S.J.L. Billinge, E.J. McKimmy, M. Shatnawi, H.J. Kim, V. Petkov, D. Wermeille, T.J. Pinnavaia, Mercury binding sites in thiol-functionalized mesostructured silica, J. Am. Chem. Soc. 127 (2005) 8492–8498. https://doi.org/10.1021/ja0506859.

[180] V. Antochshuk, O. Olkhovyk, M. Jaroniec, I.S. Park, R. Ryoo, Benzoylthiourea-modified mesoporous silica for mercury(II) removal, Langmuir. 19 (2003) 3031–3034. https://doi.org/10.1021/la026739z.

[181] V. Hernández-Morales, R. Nava, Y.J. Acosta-Silva, S.A. MacÍas-Sánchez, J.J. Pérez-Bueno, B. Pawelec, Adsorption of lead (II) on SBA-15 mesoporous molecular sieve functionalized with -NH2 groups, Microporous Mesoporous Mater. 160 (2012) 133–142. https://doi.org/10.1016/j.micromeso.2012.05.004.

[182] R. Gupta, S.K. Gupta, D.D. Pathak, Selective adsorption of toxic heavy metal ions using guanine-functionalized mesoporous silica [SBA-16-g] from aqueous solution, Microporous Mesoporous Mater. 288 (2019) 109577. https://doi.org/10.1016/j.micromeso.2019.109577.

[183] J.K. Kang, S.C. Lee, H.Y. Jang, S.B. Kim, Synthesis of poly(ethyleneimine)-functionalized mesoporous silica gel with dual loading of host ion and crosslinking for enhanced heavy metal removal in multinary solutions, Microporous Mesoporous Mater. 311 (2021) 110698. https://doi.org/10.1016/j.micromeso.2020.110698.

[184] X. Wang, Q. Guo, J. Zhao, L. Chen, Mixed amine-modified MCM-41 sorbents for CO2 capture, Int. J. Greenh. Gas Control. 37 (2015) 90–98. https://doi.org/10.1016/j.ijggc.2015.03.018.

[185] V. Zelenak, D. Halamova, L. Gaberova, E. Bloch, P. Llewellyn, Amine-modified SBA-12 mesoporous silica for carbon dioxide capture: Effect of amine basicity on sorption properties, Microporous Mesoporous Mater. 116 (2008) 358–364. https://doi.org/10.1016/j.micromeso.2008.04.023.

[186] L. Wang, M. Yao, X. Hu, G. Hu, J. Lu, M. Luo, M. Fan, Amine-modified ordered mesoporous silica: The effect of pore size on CO2 capture performance, Appl. Surf. Sci. 324 (2015) 286–292. https://doi.org/10.1016/j.apsusc.2014.10.135.

[187] M. Mohamedali, H. Ibrahim, A. Henni, Imidazolium based ionic liquids confined into mesoporous silica MCM-41 and SBA-15 for carbon dioxide capture, Microporous Mesoporous Mater. 294 (2020) 109916. https://doi.org/10.1016/j.micromeso.2019.109916.

[188] E. Glueckauf, Theory of chromatography, Trans. Faraday Soc. 51 (1955) 1540. https://doi.org/10.1002/9783527619610.ch2.

[189] G.A. Howard, A.J.. Martin, The separation of the C12-C18 fatty acids by reversed-phase partition chromatography., Biochem. J. 46 (1950) 532–538.

[190] J.J. Kirkland, Controlled surface porosity supports for high-speed gas and liquid chromatography, Anal. Chem. 41 (1969) 218–220. https://doi.org/10.1021/ac60270a054.

[191] S. Pantsulaia, K. Targamadze, N. Khundadze, Q. Kharaishvili, A. Volonterio, M. Chitty, T. Farkas, B. Chankvetadze, Potential and current limitations of superficially porous silica as a carrier for polysaccharide-based chiral selectors in separation of enantiomers in high-performance liquid chromatography, J. Chromatogr. A. 1625 (2020) 0–9. https://doi.org/10.1016/j.chroma.2020.461297.

[192] K. Nakamura, S. Saito, M. Shibukawa, Intrinsic difference between phenyl hexyl- and octadecyl-bonded silicas in the solute retention selectivity in reversed-phase liquid chromatography with aqueous mobile phase, J. Chromatogr. A. 1628 (2020) 461450. https://doi.org/10.1016/j.chroma.2020.461450.

[193] S.K. Natarajan, S. Selvaraj, Mesoporous silica nanoparticles: Importance of surface modifications and its role in drug delivery, RSC Adv. 4 (2014) 14328–14334. https://doi.org/10.1039/c4ra00781f.

[194] I.I. Slowing, J.L. Vivero-Escoto, C.W. Wu, V.S.Y. Lin, Mesoporous silica nanoparticles as controlled release drug delivery and gene transfection carriers, Adv. Drug Deliv. Rev. 60 (2008) 1278–1288. https://doi.org/10.1016/j.addr.2008.03.012.

[195] J. Kim, H.S. Kim, N. Lee, T. Kim, H. Kim, T. Yu, I.C. Song, W.K. Moon, T. Hyeon, Multifunctional uniform nanoparticles composed of a magnetite nanocrystal core and a mesoporous silica shell for magnetic resonance and fluorescence imaging and for drug delivery, Angew. Chemie - Int. Ed. 47 (2008) 8438–8441. https://doi.org/10.1002/anie.200802469.

[196] T. Yamada, H.S. Zhou, H. Uchida, M. Tomita, Y. Ueno, T. Ichino, I. Honma, K. Asai, T. Katsube, Surface photovoltage NO gas sensor with properties dependent on the structure of the self-ordered mesoporous silicate film, Adv. Mater. 14 (2002) 812–815. https://doi.org/10.1002/1521-4095(20020605)14:11<812::AID-ADMA812>3.0.CO;2-W.

[197] D.R. Radu, C.-Y. Lai, J.W. Wiench, M. Pruski, V.S.-Y. Lin, Gatekeeping layer effect: a poly(lactic acid)-coated mesoporous silica nanosphere-based fluorescence probe for detection of amino-containing neurotransmitters., J. Am. Chem. Soc. 126 (2004) 1640–1. https://doi.org/10.1021/ja038222v.

[198] J.E. Amonette, J. Matyáš, Functionalized silica aerogels for gas-phase purification, sensing, and catalysis: A review, Microporous Mesoporous Mater. 250 (2017) 100–119. https://doi.org/10.1016/j.micromeso.2017.04.055.

[199] L.P. Ravaro, P.C. Ford, A.S.S. de Camargo, Optical oxygen sensing by MPA-capped CdTe quantum dots immobilized in mesoporous silica, Microporous Mesoporous Mater. 303 (2020) 110237. https://doi.org/10.1016/j.micromeso.2020.110237.

# *Chapter 2*

# *Experimental*

## 2.1 Synthesis of silicas

### *2.1.1 Preparation of mesoporous silica SBA-15*

The synthesis of mesoporous silica SBA-15 consisted of the following procedure. 8.0 g of Pluronic 123 ($PEO_{20}PPO_{70}PEO_{20}$) was stirred in 60 mL of deionised (DI) water at 40 ˚C until it was fully dissolved. 116.5 mL of 2M hydrochloric acid was added followed by the dropwise addition of TEOS. The reaction solution was then sealed and autoclaved at 90 ˚C for 48 hours with no stirring. The resulting precipitate was filtered and washed with DI water. The solid was dried and calcined in a furnace at 550 ˚C for 6 hours. This method of preparation was followed from Zhao et at[1].

### *2.1.2 Preparation of mesoporous silica MCM-41*

The synthesis of mesoporous silica MCM-41 consisted of the following procedure. 4.8 g of hexadecyltrimethylammonium bromide (CTAB) was dissolved in 240 g of DI water by stirring. 16 mL of ammonium hydroxide solution was added when all the CTAB was dissolved and no foam was seen. After 10 min, 20 mL of TEOS was added slowly. The solution mixture was stirred overnight for 18 hours and then filtered. It was washed thoroughly with equal aliquots of ethanol and DI water, three times each. The resulting solid was calcined for 8 hours in a furnace at 550 ˚C. The method of preparation was followed from Kumar et al[2].

## 2.2 Preparation of piranha acid solution

The use of piranha acid requires great care and attention. It was also prepared as required for cleaning of the mesoporous silica and silicon wafer substrates. It reacts strongly with organics. It consists of a mixture of sulfuric acid ($H_2SO_4$) and hydrogen peroxide ($H_2O_2$) and was prepared in a ratio of 3:1 for sulfuric acid to hydrogen peroxide[3–5]. Typical quantities were as follows; 30 mL of $H_2SO_4$ was placed in a round-bottom flask to which 10 mL of $H_2O_2$ was added dropwise over the course of 15 minutes. The solution was then used as required.

## 2.3 Characterisation techniques

### *2.3.1 Electron microscopy*

Electron microscopy consists of the most commonly used techniques employed to visually image and characterise materials, not just in the area of silica materials. Higher resolving power is achieved compared with conventional microscopy as the wavelength of the electron is 10,000 times shorter. Electron microscopy is made up of scanning electron microscopy (SEM) and transmission electron microscopy (TEM). TEM imaging is the phenomenon of electrons tunnelling through a sample and in terms of porous silicas requires a tiny sample amount for imaging. Samples are dispersed in HPLC grade water and dropped on copper grids to which some sample will stick. TEM allows the imaging of the pore structure although of a very small sample size. SEM imaging uses the scattering of secondary and back-scattered electrons. The electron beam is scanned across the sample surface and produces images which show the morphology of the silica materials. SEM was carried out using a Karl Zeiss Ultra Plus field emission (in-lens detection) with Gemini column. TEM was carried out using a JOEL 2100 operating at 200 kV. All images were acquired in bright-field mode.

### *2.3.2 Nitrogen sorption analysis*

The characterisation of porous materials is impossible without $N_2$ sorption analysis to measure the physical properties of the synthesised porous silica materials. Physisorption analysis examines the adsorption and desorption isotherms of nitrogen at 77 K to the surface of the porous material. The adsorption-desorption isotherm over a range of $P/P_0$ against quantity of $N_2$ allows the determination of the porous structure, be they micro, meso or macro pores. Methods such as the Brunauer-Emmet-Teller (BET) and Barret-Joyner-Halenda (BJH) allow for the calculation and measurements of surface areas and pore volume/size distribution respectively[6,7]. The instrument used was a Micromeritics Tristar II surface area analyser. The specific surface area was calculated using the multi-point BET method in the relative pressure range $P/P_0$ = 0.05-0.3. The specific pore volume, pore diameter and pore size distribution were calculated based on the

desorption plot using the BJH method. Sorption analysis was carried out at 77 K and was degassed under $N_2$ prior to analysis for 5 hours at 200 ˚C.

### *2.3.3 Fourier-transform Infrared spectroscopy (FT-IR)*

Infrared spectroscopy is an important tool to help identify characteristic molecular functional groups which are present in samples. Infrared wavelengths are radiated at a sample which interacts by absorbing quantised levels of energy. This allows oscillations of specific frequencies to occur for particular functional groups. These specific frequencies produce a spectrum which is displayed in wavenumbers ($cm^{-1}$) which is the reciprocal of the wavelength in cm against absorption or transmittance. Infrared spectroscopy is split between near-IR (12800-4000 $cm^{-1}$), middle-IR (4000-200 $cm^{-1}$) and far-IR (200-10 $cm^{-1}$). Most infrared spectroscopy occurs in the range of 4000-400 $cm^{-1}$. In Chapter 3 and 4, the instrument used was a Bruker Tensor II (mid-range extended with diamond UATR) and the spectra collected used an attenuated total reflection infrared accessory. Spectra were recorded in the range 4000-250 $cm^{-1}$. In chapter 5 a Varian 660-IR spectrometer using a diamond crystal ATR Golden Gate was used. Spectra were recorded in the range 4000-500 $cm^{-1}$. All the data was taken as the average of 32 scans at 2 $cm^{-1}$ resolution.

### *2.3.4 X-ray photoelectron spectroscopy (XPS)*

X-ray photoelectron spectroscopy is a qualitative and quantitative technique which measures the kinetic energy of electrons which are emitted from a samples surface after x-ray photons are bombarded onto a sample's surface. Typically, soft x-rays from aluminium, magnesium or silver sources are used. As the method emits photoelectrons from the sample's atomic core, information on chemical states, atomic states and elemental composition can be determined. Kinetic energy of photoelectrons is converted to binding energy of which is displayed in spectra. Core lines relating to atomic states are displayed at specific binding energies which allows for qualitative analysis. Electrons which are emitted from the surface without any loss in kinetic energy produce narrow specific peaks which are followed by background of electrons which loose energy through

inelastic scattering. Ultra-high vacuum is required for XPS analysis as the photon energy must only interact with the surface of interest. For also this reason, XPS is a completely surface sensitive technique with characterisation only possible for a depth of 10 nm. It is the most important technique for surface science characterisation. XPS was carried out at ultra-high vacuum ($<5x10^{-10}$ mbar) on a VG Scientific ESCA lab Mk II system equipped with a hemispherical analyser using Al Kα lines (1486.6 eV). The photoelectrons were collected at an angle of 90˚ from the surface of the sample. The pass energy of the survey scans was 200 eV.

### *2.3.5 Nuclear magnetic resonance (NMR) spectroscopy*

Nuclear magnetic resonance (NMR) spectroscopy utilises nuclei's behaviour to react in a magnetic field. The technique functions as the nuclei are subjected to a magnetic field, if the correct frequency related to specific chemical environments occurs, the spin of the nuclei flips to its higher energy level. This causes a resonance of that particular frequency which in turn produces a peak on a spectrum relating to a particular chemical environment. The frequency of the resonance is both equally dependant on the external magnetic field (force applied), $B_0$ and the identity of the nuclei involved. Some magnetic nuclei which are most determined are $^{1}H$, $^{2}H$, $^{13}C$ and $^{29}Si$. The use of solid-state magic angle spinning (MASNMR) was used for analysis. This is a technique where the material is rotated on an axis to the magnetic field at a 'magic angle' of 54.74˚. This allows anisotropic dipole interactions to be suppressed to allow for greater resolution of nuclei states. MASNMR was carried out using a Bruker AVANCE II HD instrument, using a 3.2 mm HX cross-polarisation MAS probe. $^{2}H$ spectra used a one pulse sequence with a temperature of 20 ˚C and a spin rate of 10 kHz. $^{29}Si$ spectra used a standard cross polarisation sequence with a magnitude of 60 kHz for the Si radio frequency field, 50 kHz for the proton decoupling field with a contact time of 1 ms and a spin rate of 5 kHz at a temperature of 20 ˚C. $^{13}C$ spectra had a standard cross polarisation pulse sequence in a 60 kHz C field. The proton decoupling field was 50 kHz with a contact time of 3 ms and a spin rate of 10 kHz. The sample temperature was set at 20 ˚C.

### *2.3.6 Elemental analysis*

A technique also known as microanalysis, is used typically to measure the composition of compounds i.e. empirical formulas. It does this by complete combustion (up to 1800 ˚C) of a sample in oxygen rich environment which leads to the conversion of different gases relating to the elemental composition. In the case of carbon, hydrogen, and nitrogen (CHN) analysis, carbon in the sample produces $CO_2$, hydrogen produces $H_2O$ and nitrogen can be $NO_x$ or $N_2$. These gases are detected typically by a thermal conductivity detector. The instrument used was an Elementar vario EL cube elemental analyser.

### *2.3.7 X-ray diffraction (XRD)*

X-ray diffraction is a technique used to measure or identify the crystal structure of materials along with measuring the size and shape of the material. The premise of XRD is x-ray electromagnetic radiation is transmitted at a sample and depending on the wavelength of the incident x-ray and the angle to which it is emitted from the atoms in the crystal causes a special interference effect called diffraction. The interference occurs when x-rays interact with each other. When the waves are in alignment, they are said to be constructive and amplify the signal producing peaks. When the waves are not aligned, they are said to be destructive and no signal is produced. As the wavelength of the incident x-ray interacts with well-defined planes of crystal structures, the specific angle of the scattered beam from the lattice points amplify the signal and produce the x-ray pattern. The principal of the technique follows Bragg's law;

$$\mathbf{n\lambda = 2dsin\theta} \qquad \textbf{EQ.2.1}$$

The instrument used to carry out XRD was completed on a Bruker D8 Advance diffractometer equipped with an un-monochromated Cu-$K_\alpha$ source with a 1D detector which includes an energy discriminator which filters out Cu-$K_\beta$. Samples were ran in the low angle range from 0.5˚ to 5˚ ($0.5^\circ \leq \theta \geq 5.0^\circ$).

### *2.3.8 Contact angle measurements*

Atoms and molecules interact differently at the surface than they do at the bulk of the material. For this reason, contact angle measurements are an important tool to measure surface properties. The technique works by releasing a drop of a liquid with known properties and parameters onto a surface and then using a high-speed camera to measure/record the contact angle of the resulting droplet. This is called static contact angle. If the resulting angle is below 90˚ it is said to be wetting and if above is said to be non-wetting. This can lead one to determine if the surface of materials is hydrophilic or hydrophobic or allow the tracking of a process of functionalisation of a surface. Dynamic contact angle is the measuring of the contact angle as liquid is added to the surface and as the droplet is moving. Dynamic contact angle and surface free energy were calculated from the advancing and receding water contact angles and were recorded on three different regions of each sample as outlined by Lundy et al[8]. Silica particles were pressed to a pressure of two tonnes into disks before contact angle measurements. Water and diiodomethane were used as liquids and the values used were as follows;

$H_2O$ $\gamma lvD/\gamma lvP$ = 21.8/50.8 mJ $m^{-2}$ & $CH_2I_2$ $\gamma lvD/\gamma lvP$ = 48.5/2.3 mJ $m^{-2}$.

In chapter 3, 150 nL of the liquid was dispensed on the material surface at a flow rate of 15 $nLs^{-1}$. In chapter 5, 60 nL of the liquid was dispensed on the material surface at a flow rate of 5 $nLs^{-1}$. Both used a microinjection syringe pump (SMARTouch, World Precision Instruments, Sarasota, FL, USA) with a 35-gauge needle and images were captured with a monochrome industrial camera (DMK 27AUR0135, The Imaging Source, Bremen, Germany). Contact angles were calculated using a piecewise polynomial fit (ImageJ, ver. 1.46, DropSnake plugin). Surface energy calculations were determined using Fowkes' theory.

### *2.3.9 Thermo-gravimetric analysis (TGA-DTG)*

Thermogravimetric analysis is the technique of tracking the change in weight of a sample or material as a function of temperature or time. The technique is quantitative and qualitative and is

carried out by placing the sample in a TGA pan which hanged from a balance and enclosed inside a chamber. As the analysis proceeds, the weight loss is measured as a function of the temperature or time increase. The technique is widely used to measure decomposition of samples or evolution of water from porous materials. TGA was carried out using a Model TGA 2950 high-resolution thermogravimetric analyser V5.4a, on a temperature level from 30 to 800 °C with a warming speed of 5 °C $min^{-1}$ under nitrogen flow.

### *2.3.10 Atomic force microscopy (AFM)*

Atomic force microscopy (AFM) is again a surface sensitive technique which uses a cantilever tip which is rastered over the surface of substrate samples to give topographic information on the sample. The tip is brought near the surface and the potential is measured based on the distance between the two. A mix of attractive and repulsive forces cause the tip to hover or contact the surface allowing the topography to me determined. The AFM instrument used was a Park system, XE-7, made in South Korea. Measurement were performed in non-contact mode with high resolution, silicon micro-cantilever tips. Topographic images were recorded at a resonance frequency of 270-300 kHz.

## 2.4 References

[1] D. Zhao, Q. Huo, J. Feng, B.F. Chmelka, G.D. Stucky, Tri-, Tetra-, and Octablock Copolymer and Nonionic Surfactant Syntheses of Highly Ordered, Hydrothermally Stable, Mesoporous Silica Structures, J. Am. Chem. Soc. 120 (1998) 6024–6036.

[2] S. Kumar, M.M. Malik, R. Purohit, Synthesis Methods of Mesoporous Silica Materials, Mater. Today Proc. 4 (2017) 350–357. https://doi.org/10.1016/j.matpr.2017.01.032.

[3] J. Rużyłło, Electrochemical Society. Electronics Division., F. Electrochemical Society. Meeting (192nd : 1997 : Paris, Cleaning Technology in Semiconductor Device Manufacturing, 1998.

[4] N.S.K. Gunda, M. Singh, L. Norman, K. Kaur, S.K. Mitra, Optimization and characterization of biomolecule immobilization on silicon substrates using (3-aminopropyl)triethoxysilane (APTES) and glutaraldehyde linker, Appl. Surf. Sci. 305 (2014) 522–530. https://doi.org/10.1016/j.apsusc.2014.03.130.

[5] N. Aissaoui, L. Bergaoui, J. Landoulsi, P. Vi, Silane Layers on Silicon Surfaces : Mechanism of Interaction , Stability , and Influence on Protein Adsorption, Langmuir. (2012) 656–665. https://doi.org/10.1021/la2036778.

[6] S. Brunauer, P.H. Emmett, E. Teller, Adsorption of Gases in Multimolecular Layers, J. Am. Chem. Soc. 60 (1938) 309–319. https://doi.org/citeulike-article-id:4074706\rdoi: 10.1021/ja01269a023.

[7] E.P. Barrett, L.G. Joyner, P.P. Halenda, The determination of pore volume and area distributions in porous substances. Computations from nitrogen isotherms, J. Am. Chem. Soc. 73 (1951) 373–380.

[8] R. Lundy, C. Byrne, J. Bogan, K. Nolan, M.N. Collins, E. Dalton, R. Enright, Exploring the Role of Adsorption and Surface State on the Hydrophobicity of Rare Earth Oxides, ACS Appl. Mater. Interfaces. 9 (2017) 13751–13760.

# *Chapter 3*

# *Hydroxylation methods for mesoporous silica and their impact on surface functionalisation*

## 3.1 Abstract

Silica supports used e.g. in chromatography, separation and bioassay lack complete efficacy unless they are surface functionalised. Thus, chemistries are grafted to the surface to enhance their properties and capacity in specific applications. Here, various strategies are examined for 'cleaning' and hydroxylation of SBA-15 mesoporous silica (as a high surface area exemplar) to sponsor efficient functionalisation through maximising surface hydroxyl groups as the surface binding sites. Cleaning process effects on the mesoporous silica were studied using transmission electron microscopy (TEM) and scanning electron microscopy (SEM). The physical properties were characterised using $N_2$ sorption and x-ray diffraction (XRD). The bulk and surface compositions were characterised by Fourier-transform infrared (FTIR) spectroscopy and $^{29}Si$ nuclear magnetic resonance (NMR) spectroscopy. Contact angle measurements were also taken, and the surface energy components calculated. Finally, the mesoporous silica was functionalised with 3-(aminopropyl) triethoxysilane (APTS) to determine the impact of these cleaning methods on grafting. Elemental analysis along with NMR ($^{13}C$ and $^{1}H$) were used to determine the impact. This study provides a facile approach to prepare organosilicas for potential higher loading capacities.

## 3.2 Introduction

Ordered mesoporous silica (OMS) substrates and particulates are a primary focus of research due to a wide variety of application areas including adsorbents[1,2], drug delivery[3], catalysis[4,5], therapeutics and imaging[6], sensors[7], gas capture[8,9] and storage[10,11]. Interest derives from advantages such as variations of pore morphology[12,13], high mechanical stability[14–16], adjustable pore sizes[17–19] and high surface areas. Silica supports have particular relevance due to ease of functionalisation by silane reagents. Due to their high surface area, OMS materials offer

opportunities for study and developing greater understanding of mechanism as their high surface area allows for easier detection of surface species.

In silica functionalisation, grafting of various alkyl or other functional groups takes place at surface hydroxyl sites[20,21] be this for any application. Functionalisation is dependent on the presence of surface silanol sites [Si-O-H] [22] with sites such as siloxane bridges [Si-O-Si] largely inactive. Grafting of organosilanes (most notably 3-(aminopropyl) triethoxysilane or APTS)[15,23] is the most widely studied method of functionalisation and acts as a precursor to a significant number of intermediate or terminal functional groups (-$NH_2$, -SH, -COOH)[24,25]. Similar methodologies are used for chromatography, enzyme immobilisation and small molecule separations[26–28]. For gas sensing and storage, primary amine groups of e.g. APTS provide sites for storage of gases including carbon dioxide[8,29].

Key to effective functionalisation is a strong covalent bond between the support and the organosilane to increase efficiency and lifetime of the material. Optimal conditions for functionalisation are vital for reaching the maximum silane capacity and performance. Cleaning methods are thought to play a crucial role in surface grafting, by removal of contaminants and hydroxylation of the surface for silane attachment[30]. Such methods parallel the cleaning of silicon wafers in the semiconductor industry[31–34]. These cleaning methods include washing and refluxing in piranha solution (sulphuric acid and hydrogen peroxide combine with the formation of peroxymonosulfuric acid) and other solutions, along with ultraviolet light and ozonolysis[35–37]. Other methods from the semiconductor industry are hydrofluoric acid wash and plasma cleaning but these result in surface damage or add preparation complexity to physical particles. In industry, grafting methods can be lengthy, complex, intricate, and unreliable at scale and it is postulated that process efficiency could be increased using effective pre-treatments.

This work, the first of its kind, was to determine the impact of various silica pre-treatment steps to define the relationship between cleaning, rehydroxylation, and changes in silane attachment. To achieve this, OMS was synthesised and characterised. The silica was then cleaned by several methods and studied. This cleaned material was then functionalised, characterised, and compared to silica material which was not cleaned prior to functionalisation.

## 3.3 Materials & Methods

### *3.3.1 Materials*

Pluronic 123 (poly(ethylene glycol)-block-poly(propylene glycol)-block-poly(ethylene glycol), tetraethyl orthosilicate (>99%), hydrochloric acid (ACS reagent 37%), 3-(aminopropyl) triethoxysilane (99%), sulphuric acid (ACS reagent 95-98%), nitric acid (ACS reagent 70%), hydrogen peroxide solution (30%), 2-propanol (CHROMASOLV, for high performance liquid chromatography [HPLC], 99.9%), dimethyl sulfoxide (anhydrous 99.9%) were purchased from Sigma Aldrich, Ireland.

### *3.3.2 Synthesis of SBA-15*

The preparation of silica SBA-15 followed procedure reported by Zhao et al [34]. 8.0 g of Pluronic 123 was stirred in 60 mL of deionised (DI) water at 40 °C until fully dissolved. 116.5 ml of 2M HCl was added followed by dropwise addition of 17.6 ml TEOS (tetraethyl orthosilicate). The reaction solution was transferred into a sealed bottle and autoclaved at 90 °C for 48 hours without stirring. The white product was filtered and washed with DI water. The solid was dried and calcined at 550 °C for 6 hours. The term SBA-15 refers to a calcined material. Within this chapter, SBA was synthesised once and therefore no replicates were made.

### *3.3.3 Cleaning of mesoporous silicas*

1 g of SBA-15 was measured into a flask and 10 ml of nitric acid was added. The solution was refluxed at 100 °C for 60 min. The mixture was filtered and rinsed with DI water. In a similar manner, SBA-15 was treated with piranha solution (3:1 ratio of $H_2SO_4$ to $H_2O_2$[38]). The mesoporous silica was refluxed for 60 min at 100 °C. Acid mixtures were diluted to 150 ml with DI water and then filtered and rinsed with DI water. Ultraviolet ozonolysis ($UV/O_3$) was examined as it is widely used to remove any organics on silicon wafer substrates[25] and silicon slabs[39]. SBA-15 was placed on a glass plate and evenly spread as a thin layer to ensure the same level of cleaning throughout the sample. As controls, samples underwent no cleaning method and also after reflux in de-ionized (DI) as acid treated samples. All samples were dried in an oven at 110 °C for 60 min for further study/use.

### *3.3.4 Functionalisation of mesoporous silica with silane*

The cleaned materials were functionalised with APTS using the following method. 1 g of dried silica (cleaned/not) was placed in a flask containing 9.0 % (v/v) solution of APTS in dimethyl sulfoxide (1.0 mL of APTS in 10 mL DMSO)[40]. The reaction was carried out at 90 °C for 60 min. The functionalised silica was then filtered, washed with DMSO, propan-2-ol and DI water. The amine grafted SBA-15 was then dried in the oven at 80 °C until used.

### *3.3.5 Characterisation techniques*

#### 3.3.5.1 Electron microscopy

Scanning electron microscopy (SEM) was carried out using a Karl Zeiss Ultra Plus field emission SEM (in-lens detection) with Gemini column to provide detailed external surface morphology. The samples were placed on carbon tape and then to a stainless-steel stub before being placed in the instrument's chamber. It was operated at 5 KeV. Transmission electron microscopy (TEM)

provided detailed images of the internal structure of the synthesised mesoporous silica. The samples were sonicated in HPLC grade water and dropped on support films of lacey carbon with 200 mesh copper grids. The TEM used was a JOEL 2100 operating at 200 kV. All images were acquired in bright field mode.

#### 3.3.5.2 Contact angle measurements & Surface energy calculations

Samples were pressed into disks to a pressure of 2 tonnes and advancing contact angle (CA) measurements were recorded on a custom-built system of each sample using 60 Hz sampling rate high speed camera to examine the changes after the various stages outlined in the introduction. Water (polar) and diiodomethane (non-polar) were used to measure the contact angle of the droplets. A droplet size of 150 nL was used at a rate of 15 $nLs^{-1}$ using a 35-gauge needle for all disks and both solvents. ImageJ software (dropsnake as a plugin) was used to process the images and measure the advancing contact angle. Surface energy calculations were determined using Fowkes' theory.

#### 3.3.5.3 Fourier transform infra-red (FT-IR)

Fourier transform infra-red spectroscopy was performed using a Bruker Tensor II (mid-range extended with diamond UATR) and was collected using an attenuated total reflection infrared accessory. Spectra of the SBA-15 at various stages of the process were recorded in the range 250 to 4000 $cm^{-1}$.

#### 3.3.5.4 $N_2$ adsorption-desorption isotherms

The surface area, pore diameter, pore volume and pore size distributions were calculated using $N_2$ sorption technique on a Micromeritics Tristar II surface area analyser (Micrometrics, Norcross, GA, USA). The specific surface area was calculated using the multi-point Brunauer, Emmett and Teller (BET) method [41] in the relative pressure range $P/P_0$ = 0.05-0.3. The specific pore volume,

pore diameter and pore size distribution curves were calculated based on the Barrett-Joyner-Halenda (BJH) method [42]. The sorption analysis carried out was measured at 77 K. Each sample was degassed under nitrogen for five hours at 200 ˚C prior to analysis.

#### 3.3.5.5 Elemental analysis

Elemental analysis (Elementar vario EL cube elemental analyser) was used to determine the percentage carbon and nitrogen in the sample. All analyses were in triplicate.

#### 3.3.5.6 Nuclear Magnetic Resonance (NMR)

Standard liquid phase NMR was carried out along with solid state, magic angle spinning, MASNMR. The method followed for liquid phase NMR was described by Thomé et al[43]. An NMR stock solution was produced by adding acetic anhydride (190 µL, 2.0 mmol) into a 10 mL volumetric flask and was filled with $D_2O$. Both phases were combined before filling up to the mark. For the NMR measurements, the mass of the mesoporous material (bare, cleaned, or functionalised) was weighed (100 mg) into a microtube with cap. The NMR stock solution was added (100 µL) followed by 400 µL of 40 wt% NaOD/$D_2O$. The microtube was shaken for 30 min and allowed to stand for another 30 min to ensure full dissolution of the mesoporous silica materials. The solution was transferred to an NMR tube.

MASNMR data were recorded on a Bruker AVANCE II HD, using a 3.2 mm HX cross-polarisation (CP) magic angle spinning (MAS) probe. The proton spectra used a one pulse sequence with a temperature of 20 ˚C and a spin rate of 10 kHz. The silicon spectra used a standard cross polarisation sequence with a magnitude of 60 kHz for the Si radio frequency field, 50 kHz for the proton decoupling field with a contact time of 1 ms and a spin rate of 5 kHz with a temperature of 20 ˚C. The carbon spectra had a standard cross polarisation pulse sequence in a 60

kHz C field. The proton decoupling field was 50 kHz with a contact time of 3 ms and a spin rate of 10 kHz. The sample temperature was set at 20 ˚C.

#### 3.3.5.7 X-ray diffraction (XRD)

X-ray diffraction (XRD) patterns have been recorded with a Bruker D8 Advance diffractometer equipped with an un-monochromated Cu-$K_\alpha$ source with a 1D detector which includes an energy discriminator which filters out Cu-$K_\beta$. Samples were ran in the low angle range from 0.5˚ to 5˚ ($0.5^\circ \leq \theta \geq 5.0^\circ$).

## 3.4 Results and Discussion

### *3.4.1 Characterisation of SBA-15*

The $N_2$ adsorption and desorption isotherm (see figure 3A.1) of the synthesized and calcined SBA-15 (SBA-cal) is type IV with a typical hysteresis loop and a defined step seen at $P/P_0$ of 0.4-0.6 that demonstrated the material contains mesopores. The surface area of the produced material was measured at 612 $m^2g^{-1}$. The pore volume and pore diameter were determined from the desorption plot which measured 0.56 $cm^3\ g^{-1}$ and 48 Å respectively. These results are seen in table 3.1.

**Table 3.1. Physical properties of SBA-15, samples cleaned by the four methods and their corresponding properties after grafting with 3-aminopropyl triethoxysilane.**

| Sample | Cleaning Time | BET Surface Area | Pore Diameter ($P_{Ddes}$) | Pore Volume ($P_{Vdes}$) | BET Surface Area | Pore Diameter ($P_{Ddes}$) | Pore Volume ($P_{Vdes}$) |
|---|---|---|---|---|---|---|---|
| | h | $m^2g^{-1}$ | Å | $cm^3g^{-1}$ | $m^2g^{-1}$ | Å | $cm^3g^{-1}$ |
| | **Cleaning** | | | | **Functionalised** | | |
| SBA-15 | - | 612 | 48 | 0.56 | 152 | 51 | 0.23 |
| Nitric | 1 | 585 | 50 | 0.57 | 193 | 47 | 0.28 |
| | 24 | 542 | 51 | 0.56 | 151 | 54 | 0.21 |
| Piranha | 1 | 564 | 49 | 0.55 | 148 | 47 | 0.21 |
| | 24 | 488 | 52 | 0.58 | 108 | 46 | 0.15 |
| UV/Ozone | 1 | 608 | 48 | 0.56 | 211 | 44 | 0.29 |
| | 24 | 606 | 49 | 0.57 | 201 | 54 | 0.3 |
| Water | 1 | 548 | 50 | 0.56 | 162 | 44 | 0.22 |
| | 24 | 487 | 51 | 0.57 | 158 | 54 | 0.24 |

Typical spectra for calcinated OMS SBA-15 material was observed in figure 3A.2. The $SiO_2$ framework symmetric and anti-symmetrical vibrations were seen at 803 and 1063 $cm^{-1}$. The torsion vibrations of the Si-O-Si framework is also seen at 446 $cm^{-1}$[44]. Silanol peaks (Si-OH) are also observed and derive from the vibrational bending mode at 962 $cm^{-1}$[45]. Adsorbed water is also seen in the data with a sharp peak at 1637 $cm^{-1}$ along with a broad peak seen at approximately 3400 $cm^{-1}$. Finally, there is also a minor feature at 3740 $cm^{-1}$ due to the presence of silanol groups[44].

SEM images of different magnifications are seen in figure 3.1. The morphologies of the particles are of no defined shape but rather a range of different sizes and shapes as seen in figure 3.1 (ii) where morphologies of rods, spheres and pyramids can be seen. The particle size demonstrated from the SEM images also show that all particles are smaller than 100 μm (length of the largest dimension). TEM images (fig. 3.1(iv-v), show highly ordered parallel pore channels. The images also show the ordered hexagonal pore structure as the pores emerge from the surface. Using imaging software, the average pore diameter measured was 5.0 nm and pore walls were measured at 4.8 nm in close agreement with the results obtained with $N_2$ sorption measurements.

The $Si^{29}$ MASNMR spectrum showed three peaks present as seen in figure 3A.3. The peak positions seen are -91.4, -100.5 and -109.2 ppm which can be assigned to the $Q_2$, $Q_3$ and $Q_4$ peaks respectively[46]. The peaks represent the number of oxygen bonds to that silicon atom. This is demonstrated in figure 3A.3. The integrals of the peaks show the relative concentrations for the three different silicon environments.

Powder X-ray diffraction was completed on SBA-15. It is shown in figure 3A.4 and shows the low angled spectrum of the sample with the standard (1 0 0), (1 1 0) and (2 0 0) reflections typical of a hexagonal mesoscopic structure [47,48].

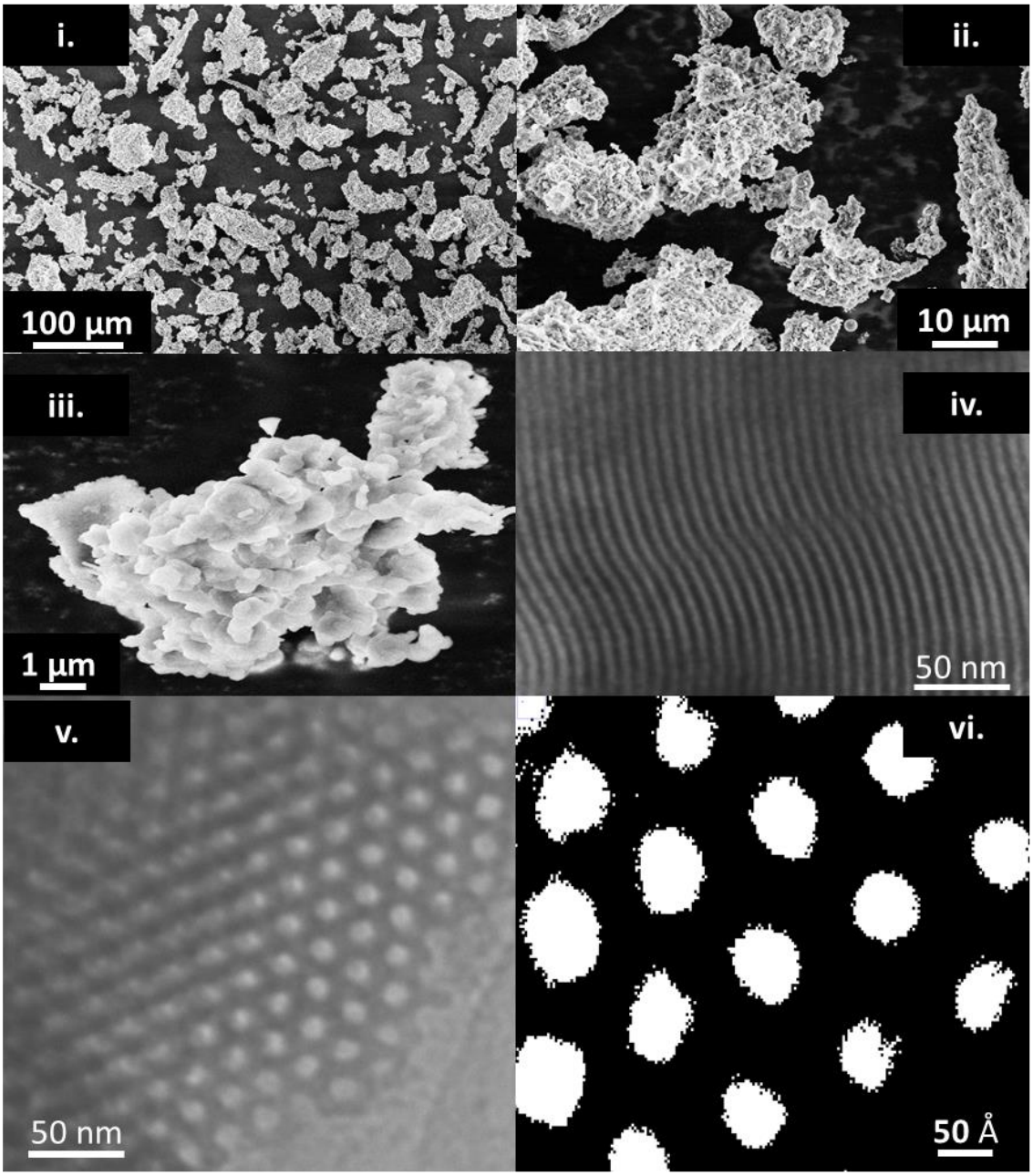


**Figure 3.1:** **Electron microscopy of synthesized mesoporous silica, SBA-15: Scanning electron microscopy (SEM) images of varying magnification; (i) 100 µm; (ii) 10 µm; (iii) 1 µm; Transmission electron microscopy (TEM) images showing the pore structures of (iv) lateral direction and (v) hexagonal pore structure. Imaging software (ImageJ) was used on TEM images to demonstrate and measure (vi) the pore diameter and pore wall thickness of the mesoporous SBA-15.**

### *3.4.2 Analysis of Cleaned SBA*

As previously discussed, four cleaning methods are examined in this study allowing comparison to as-calcined material. $N_2$ sorption results are reported in table 3.1. Figure 3.2 displays the direct impact of cleaning from the different methods by showing a reduction in surface areas. It was observed that the surface area decreased after cleaning with the different methods. This is a negative effect on the materials as one of the key attributes of OMS materials are high surface area. It is worth noting that extended cleaning times of 1 to 24 h, cause further decreases in surface area and higher pore diameter for all methods are seen.

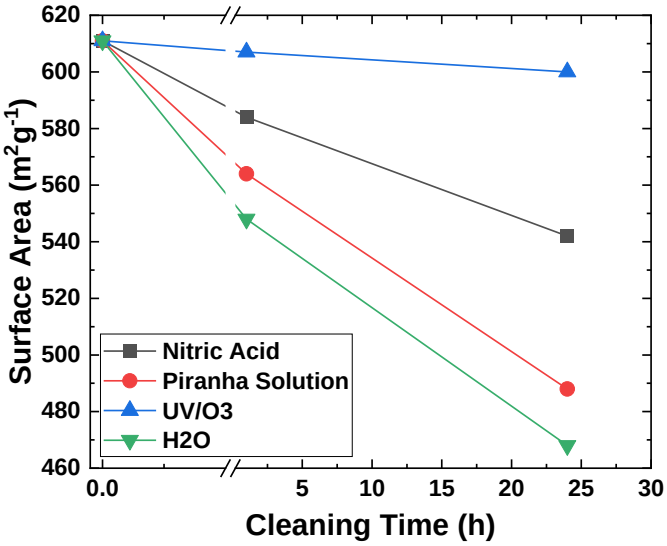


**Figure 3.2: Surface area measurements using BET method. It demonstrates the changes in surface area due to the different cleaning methods taken at 1 h and 24 h. The samples are nitric acid (square/black), piranha solution (circle/red), UV/ozone (triangle/blue) and water (nabla/green).**

The surface area decreases are assigned to pore volume and pore diameter increase suggestive of some pore etching and a possible secondary reaction step of condensation cross-linking of surface silanol groups[49–51]. For all four cleaning methods there is an increase in pore size of 2-4 Å

compared to virgin SBA-15. The surface area decreased noticeably less for ultraviolet/ozonolysis cleaning consistent with a non-chemical, non-acidic method. Cleaning in water and piranha solution causes the most significant decrease in surface area. This could be due to two different reasons. With piranha and nitric acid solutions, it is suggested that the strongly oxidising conditions completely removes any organics and may have an etching effect. With water it is suggested that this is an absorption effect. Cleaning might cause physisorption of water and blocking of smaller pores. These pores may not be cleared by degassing. Smaller pore sizes may result from multilayers of water condensing on cleaned pore walls.

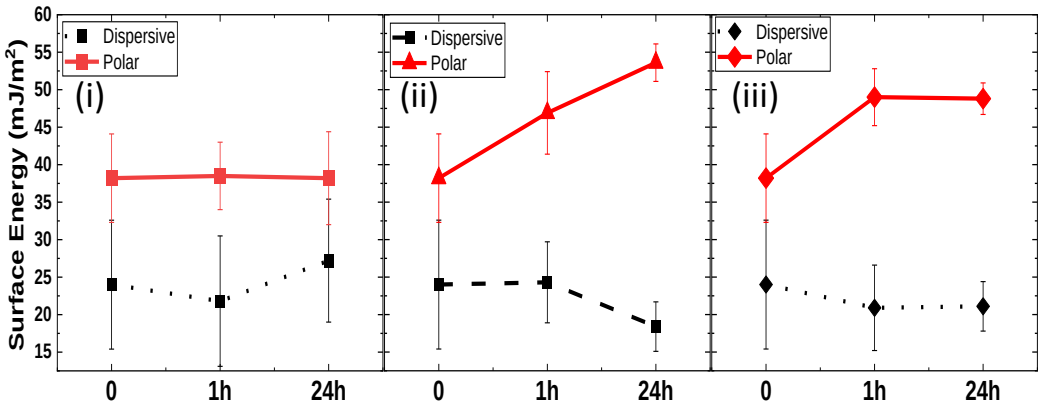


**Figure 3.3: Surface energy measurements for cleaned SBA-15 samples broken down into their polar and dispersive interactions. These are based on their corresponding contact angle measurements using the Owens-Wendt approach. The figure shows (i) Nitric acid (ii) Piranha solution (iii) UV/Ozone. Data points represent a minimum of 3 replicates.**

Contact angles of the cleaned samples are reported in table 3.2 together with the calculated surface energy measurements which show the polar and dispersive interactions. The contact angles measured in both water and diiodomethane have a degree of variation between measurements of the same sample. This is because of the non-uniform and highly porous surface of the pressed disk. The results still show the influence of cleaning on the mesoporous silica. The surface energy calculations are displayed in figure 3.3. The figure for nitric acid (i) illustrates that there is little measurable difference in the polar contributions or dispersive interactions. This would indicate

that there is no significant change in hydroxyl availability. The same trend is not seen with the other cleaning methods. The piranha solution (ii) and UV/ozone (iii) show a significant increase in the polar contributions after cleaning. This suggests more surface hydroxyl groups available for interaction compared to original SBA-15. For the piranha cleaned material there is a continual increase of surface energy from 47 to 54 mJ $m^{-2}$ for the polar contributions. For the UV/ozone cleaned samples, a plateau in polar contributions of 49 $mJm^{-2}$ after a 1-hour and 24-hour cleaning cycle. In both cases, little measurable change in dispersive interactions was observed from both.

**Table 3.2: Contact angle measurements and surface energy calculations for SBA-15 and cleaned samples. Data points represent a minimum of three replicates.**

| Sample | Time (h) | Contact Angle Measurements (θ) | | | | Surface Energy ($mJ/m^2$) | | | |
|---|---|---|---|---|---|---|---|---|---|
| | | $H_2O$ (°) | ± | $CH_2I_2$ (°) | ± | Dispersive | ± | Polar | ± |
| SBA-15 | -- | 32.5 | 6.2 | 44.6 | 10.3 | 24 | 5.9 | 38.2 | 8.6 |
| Water | 1 | 49.1 | 6.2 | 54.7 | 8.5 | 20.9 | 5.6 | 29.5 | 8.7 |
| | 24 | 33.9 | 4.6 | 36.4 | 3.2 | 28.2 | 2.1 | 34.1 | 4.2 |
| Nitric | 1 | 35.1 | 7.7 | 49.5 | 6.8 | 21.8 | 4.5 | 38.5 | 8.7 |
| | 24 | 27.8 | 6.4 | 37 | 12.1 | 27.2 | 6.2 | 38.2 | 8.2 |
| Piranha | 1 | 12 | 1.1 | 40.5 | 11.8 | 24.3 | 5.5 | 46.9 | 5.4 |
| | 24 | 8.5 | 2.3 | 52.2 | 4.9 | 18.4 | 2.5 | 53.6 | 3.3 |
| UV/Ozone | 1 | 15.7 | 5.6 | 47.8 | 6.9 | 20.9 | 3.8 | 49 | 5.7 |
| | 24 | 15.7 | 3.6 | 47.4 | 3.7 | 21.1 | 2.1 | 48.8 | 3.3 |

$^1$H NMR data are presented in table 3A.2. The integral of the standard acetate protons was used to normalise the change in HOD amount. In the process of silica dissolution in NaOD/$D_2O$, siloxane (Si-O-Si) bridges are cleaved by the NaOD and produces a deuterated silanol (Si-OD). Silanols (isolated or geminal) also interact with the NaOD/$D_2O$ by deprotonation and add to the total HOD content which would also include any deuterated amine. The HOD integral is based on the acetate concentration is shown in figure 3.4. The figure displays the HOD concentration increases after cleaning with water (2.87 & 3.14 a.u.), piranha solution (2.65 & 2.91 a.u.) and nitric acid (2.67 & 2.92 a.u.).

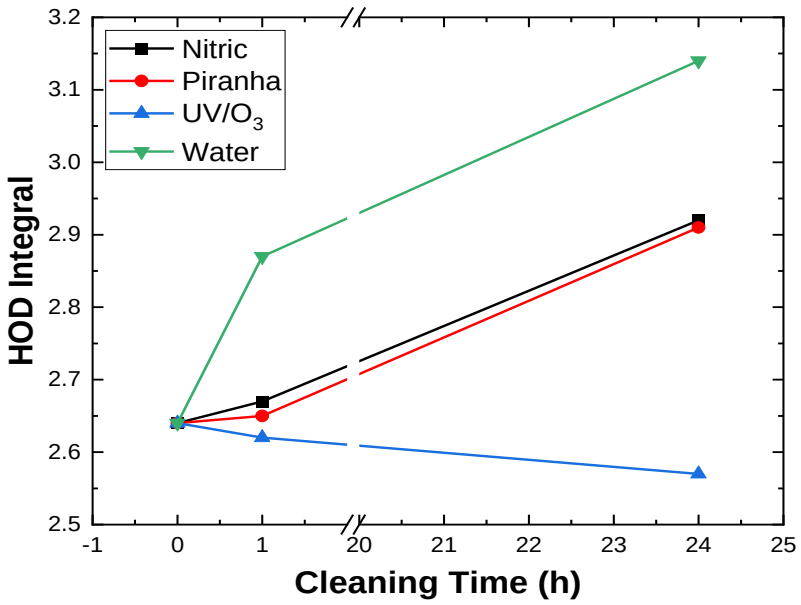


**Figure 3.4:** **$^1$H NMR of HOD integral plotted against the cleaning time of the various cleaning methods which include nitric acid (black), piranha solution (red), ultraviolet/ozonolysis (blue) and water (green).**

There is a decrease in HOD after UV/$O_3$ (2.62 & 2.57 a.u.) and this could be due to damage to the surface silanols and the material by the ozone radicals produced during cleaning. The increase in HOD seen is due to an increase in free silanols after cleaning. Another suggestive reason for

the increase in HOD could be due to adsorbed water. Piranha and nitric acid are wet methods and any water present would lead to an increase in concentration of HOD. This could also be the reason as to why water shows higher HOD compared with piranha solution and nitric acid.

Following cleaning experiments, several different outcomes are seen using MASNMR. Details of this are shown in table 3.3 which displays the relative percentages of the peaks present after cleaning. Data is displayed in this form for sample to sample comparisons. Firstly, it shows the relative concentrations of the three silicon species for SBA-15 which displays 17 %, 69 % and 14 % for Q4, Q3 and Q2 peaks, respectively. The percentages are normalised and achieved by assuming no change occurs to the Q4 siloxanes concentration as this is expected to remain unchanged because of chemical inertness. Interesting results are seen in table 3A.1 showing the normalised data based on the data in table 3.3. Cleaning with wet methods show a decrease in the isolated and geminal silanols. This could be explained by the fact that water is involved in all three methods and that water cannot be fully removed unless calcined again and under vacuum[49].

**Table 3.3.** **$^{29}$Si solid-state NMR relative percentages of the various peaks.**

| Sample Name | % Q Peak | | | | | |
|---|---|---|---|---|---|---|
| | **Q4** | **Q3** | **Q2** | **Q4** | **Q3** | **Q2** |
| **SBA-cal** | 17 | 69 | 14 | - | | |
| **SBA-APTS** | - | | | 48 | 49 | 4 |
| | **Cleaned** | | | **Functionalised** | | |
| **Nitric 1h** | 18 | 70 | 12 | 48 | 47 | 5 |
| **Nitric 24h** | 22 | 69 | 9 | 50 | 45 | 5 |
| **Piranha 1h** | 20 | 68 | 11 | 56 | 42 | 2 |
| **Piranha 24h** | 20 | 70 | 10 | 47 | 49 | 4 |
| **UVO3 1h** | 16 | 69 | 16 | 49 | 48 | 3 |
| **UVO3 24h** | 16 | 72 | 13 | 49 | 49 | 2 |
| **Water 1h** | 18 | 68 | 14 | 50 | 48 | 3 |
| **Water 24h** | 19 | 69 | 12 | 48 | 49 | 3 |

The opposite is seen when cleaned with ultraviolet/ozonolysis. An increase in Q3 and Q2 could indicate that either the surface is being rehydroxylated or that the $UV/O_3$ is damaging the surface of the silica. The latter would help explain why lower grafting is seen compared with the other methods. Further, following the $UV/O_3$ treatment the surface could be passivated by $CO_2$ or hydrocarbon adsorption as seen for activated carbon and many plastic surfaces[52,53].

FTIR was used to examine all cleaned SBA-15 samples. In figure 3.5 it can be seen that there are clear changes in the intensity of the silanol peak (962 $cm^{-1}$ [45,54]). The peaks were normalised from the beginning of the peak and compared. The spectra show that after cleaning there was an increase in peak intensity. This suggests a potential increase in number of silanols. For this study, this number was not quantified but compared to as-calcined SBA-15 material. The data show

there are slight differences in intensities for each cleaning method. For instance, after cleaning in piranha solution, the highest intensity was seen indicating the highest number of silanol groups present. Another point to note is that cleaning for 1 h and cleaning for 24 h showed the same intensity for each of the four methods. This indicates that cleaning times could be reduced to 1 h or less.

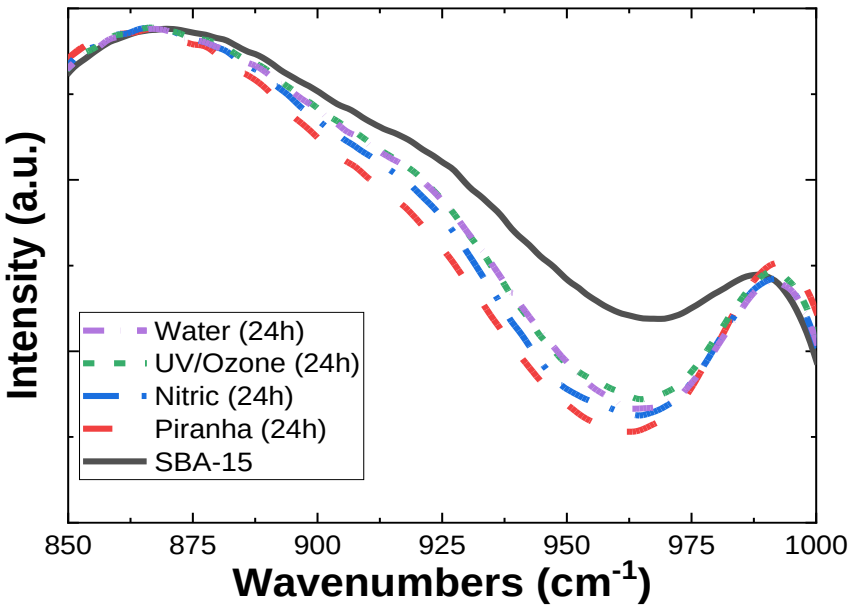


**Figure 3.5:** **FTIR Spectra of cleaned SBA-15 and calcined SBA-15. The figure shows a wavenumber (962cm$^{-1}$) associated with the presence of silanols in the material. The impact is seen by normalising the peak and showing the increase in its relative intensity to the calcined SBA-15 sample. Included are calcined SBA-15 (line/black), piranha solution (dash/red), nitric acid (dash-dot/blue), UV/ozone (dash-dash-dot/green) and water (dash-dot-dash/magenta).**

XRD was also used to examine the changes in the structure of the cleaned SBA-15. In figure 3A.4 there was no change in the pore structure after either the 1h cleaning or the 24h cleaning of each of the four cleaning methods. This was interesting as (especially with piranha for the 24h cleaned sample) it supports the suggestion that effects are largely due to pore size expansion rather than morphological changes.

### *3.4.3 Impact of Cleaning on Functionalisation*

#### 3.4.3.1 $N_2$ Sorption (Surface Area & Pore Properties)

As shown previously, cleaning reduces the surface area of the SBA-15 material and so too does functionalisation, which can be assigned to the grafting of APTS in and around the pores. The results are shown in table 3.1. The large reduction in pore volume showed that functionalisation is occurring for all samples. The largest decrease seen between the original silica material and the related cleaned SBA-15 is from the 24 h piranha grafted sample. Here the final material has a pore volume of just 0.15 $cm^3g^{-1}$ and a surface area of 108 $m^2g^{-1}$. All other pore volumes approximately fall in between a range of 0.21-0.3 $cm^3g^{-1}$ and surface areas 150-200 $m^2g^{-1}$.

Figure 3A.5 tracks the quantity of $N_2$ adsorbed through the different stages of the study from as calcined SBA-15 to piranha cleaned and grafted SBA-15. The isotherms shift to lower relative pressure as the SBA-15 material is progressed through the stages. This shows a decrease in $N_2$ adsorbed firstly due to cleaning using piranha solution and then a further reduction due to grafting from APTS.

#### 3.4.3.2 Elemental analysis

The main purpose for potentially cleaning silicas is to increase efficiency and robustness of grafting applications. Table 3.4 displays the results following grafting with APTS. Unbonded SBA-15 (control sample) showed a percentage carbon and nitrogen of 0.05 and 0.03 %, respectively. For all grafted samples, the percentage carbon ranged from 6.7 to 8.7 % and percentage nitrogen ranged from 2.0 to 2.8 %. To show the impact of cleaning, functionalisation on bare SBA-15 occurred with percentage carbon and nitrogen values showing 6.95 and 2.27 % respectively.

**Table 3.4: Elemental analysis for carbon and nitrogen content for SBA-15 and cleaned samples after functionalisation with APTS. All samples were ran in triplicate.**

| Sample | Time (h) | % C | ± | % N | ± |
|---|---|---|---|---|---|
| Control | - | 0.05 | 0.02 | 0.03 | 0.02 |
| SBA-15 | 0 | 6.947 | 0.227 | 2.271 | 0.085 |
| Nitric Acid | 1 | 7.317 | 0.046 | 2.53 | 0.017 |
| | 24 | 7.775 | 0.049 | 2.135 | 0.048 |
| Piranha Solution | 1 | 7.724 | 0.031 | 2.446 | 0.012 |
| | 24 | 8.68 | 0.495 | 2.81 | 0.141 |
| Water | 1 | 6.928 | 0.443 | 2.479 | 0.153 |
| | 24 | 6.71 | 0.156 | 2.01 | 0.12 |
| UV/Ozone | 1 | 6.94 | 0.128 | 2.1 | 0.081 |
| | 24 | 7.417 | 0.086 | 2.61 | 0.105 |

Percentage carbon shown in figure 3.6, demonstrates an increase on the control sample (no clean/black) for both nitric acid and piranha solution. The UV/ozone and water samples show no increase in percentage carbon for 1hour cleaned sample. The UV/ozone sample cleaned for 24 hours showed an increase from the control and a slight increase on the 1hour sample. The water sample produced a lower percentage carbon than the control sample and the 1hour water cleaned sample. The piranha solution, nitric acid and the UV/ozone cleaned samples all increased their percentage carbon and therefore their grafting potential with longer cleaning times. The highest grafting achieved was with piranha solution cleaned SBA-15. It had the most effective grafting for the 1hour and the 24hour cleaned sample. This 24h value was seen at 8.68 %.

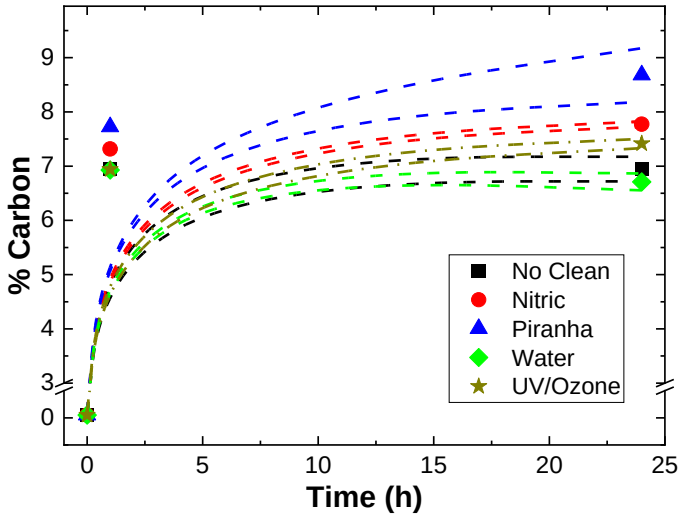


**Figure 3.6:** **Elemental analysis of various SBA-15 samples functionalised with APTS. The percentage carbon is measured for SBA-15 which was not cleaned (square/black) and cleaned samples by nitric acid (circle/red), piranha solution (triangle/blue), water (diamond/green) and UV/ozone (star/gold). The error range for each sample is also included as each sample was tested in triplicate.**

Analysis of the percentage nitrogen results are seen in figure 3.7. Again, the piranha solution achieved the highest percentage nitrogen (2.81 %) for the 24h cleaned sample compared with all other samples. The nitric acid cleaned sample had the highest percentage nitrogen for 1hour durations at 2.53 %. Water also showed a high percentage nitrogen for the 1hour sample (2.48 %) which was slightly above the piranha solution cleaned sample (2.45 %). The control no clean sample showed a percentage nitrogen of 2.27 % which was higher than the 1hour UV/ozone sample whose percentage nitrogen was 2.10 %. As already mentioned, the piranha cleaned sample grafted the largest quantity of APTS. As cleaning time increased, a decrease was seen from both water (2.01 %) and nitric acid cleaned (2.14 %) samples. Both samples fell below the control sample. Also interesting was the large increase in the UV/ozone sample which was just below the piranha solution at 2.61 %. However, we suggest that this is largely due to adventitious adsorption as mentioned.

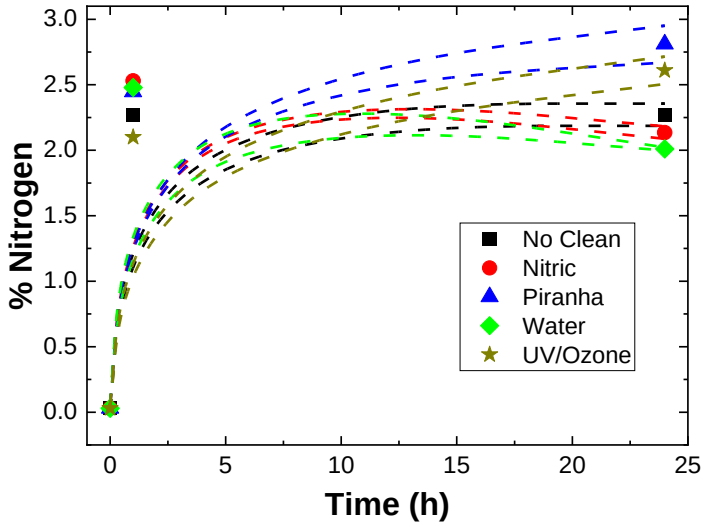


**Figure 3.7:** **Elemental analysis of various SBA-15 samples functionalised with APTS. The percentage nitrogen is measured for SBA-15 which was not cleaned (square/black) and cleaned samples by nitric acid (circle/red), piranha solution (triangle/blue), water (diamond/green) and UV/ozone (star/gold). The error range for each sample is also included as each sample was tested in triplicate.**

Note that statistical analysis was used to verify these conclusions. A significant P-value was determined from the percentage carbon results presented above. The P-value of the piranha sample cleaned for 24 hours was shown to be significantly different. It had a P-value of 0.035 which showed this to be significantly different to the control sample. The other samples after 24hour cleaning had P-values of 11.2, 39.2 and 16.0 for nitric acid, water, and UV/ozone cleaning, respectively.

### 3.4.3.3 NMR

After functionalisation, the presence of T peaks proves that successful grafting of APTS has occurred[55]. This can be seen in figure 3A.6. The results in this study show $T^2$ and $T^3$ peaks which indicate the aminopropyl group grafted to a central silicon with two adjacent O-Si (seen at -58 ppm) with one O-H and the aminopropyl group grafted to the central silicon with three

adjacent O-Si species (seen at -66 ppm), respectively[4]. The relative concentrations percentages are shown in table 3.3. The data shows grafting occurs at the isolated and geminal silanols. If the same assumptions as before are taken some comparisons can be made between samples. After grafting the relationship between Q4 siloxane and Q3 isolated silanols changes from typically 1:3.5 to 1:1. This dramatic difference shows the impact of grafting on the surface hydroxyl groups. Similarly, after cleaning the ratio between Q4 to Q2 is just less than 1:1. Cleaning methods such as piranha and nitric acid have a ratio closer to 2:1 in terms of Q4:Q2. After grafting this ratio changes to a minimum of 9:1 showing the significant change occurring to the geminal silanols. The degree of modification is also calculated by dividing the sum of the integral of the T peaks by the sum of the Q integrals[43]. The value for the degree of modification was consistent with an average at 37.5 %.

NMR was carried out using both $^{1}H$ and $^{13}C$ probes. $^{1}H$ NMR results show that grafting has occurred as the presence of the alpha, beta and gamma protons are seen. Labelling of hydrogens can be seen from table 3A.2 where the positions of the peaks are described. An example spectrum can be seen in figure 3A.7. The two control samples SBA-15 (SBA-cal) and the SBA-15 which was grafted but not cleaned (SBA-APTS) are included. Examining the samples which are cleaned and then functionalised, the data shows that some increase their HOD amount and some decrease. Interestingly, nitric acid samples increase their HOD concentration, but piranha samples remain pretty much identical to the related cleaned samples. Whereas ultraviolet/ozonolysis and water samples decrease in their HOD concentrations. Higher grafting is occurring for piranha solution and nitric acid cleaned samples compared with the others. This agrees with the elemental analysis presented above. More APTS means more amine groups and as these become deuterated in excess $D_2O$, this will add to the HOD contributions.

Carbon NMR was also carried out and the results are displayed in table 3A.3. A spectrum can be seen in figure 3A.8. The integrations are normalised to the methyl carbon and it is seen that the

alpha and gamma carbons have a higher number detected when compared to the beta carbon. The values obtained are quite similar to each other, but it is clear that the piranha cleaned samples show higher carbon concentrations along with the water cleaned samples. Also worth noting that full hydrolysis of the silane is occurring during functionalisation seen from the fact that there are no carbon peaks detected where one would expect ethoxy related carbon peaks (17 and 57 ppm)[43]. This shows some insight into the mechanism of the grafting process.

## 3.5 Conclusion

The aim of the study was to gain insight into the effects of cleaning of a silica material such as SBA-15. SBA-15, a mesoporous silica, was synthesised and characterised. The physical properties were as cited and as expected.

Cleaning of the silica surface does occur in acid. Piranha solution and nitric acid do change the surface and increase availability of surface hydroxyl groups. IR spectroscopy showed that cleaning of the material increased the intensity of the silanol peak for all methods described. Cleaning also demonstrated an increase in polar contribution to the surface energies in turn making the surfaces more hydrophilic. Cleaning did have an impact on the physical properties of the material by decreasing surface areas. Piranha solution was the most effective at these. Water cleans the silica surface but not to the same extent as piranha and nitric acid. Ultraviolet/ozonolysis cleans but is less effective due to a damaged surface and/or due to air passivation blocking silanol sites. The other three methods do not show this as water is adsorbed to the surface. These results therefore tell that the mesoporous silica is cleaned by removing adsorbates and increasing availability of silanols for functionalisation as opposed to producing more silanol groups. This was shown by NMR.

After functionalisation of the cleaned samples investigated, the cleaning methods were shown to significantly enhance the grafting of 3-(aminopropyl) triethoxysilane. Elemental analysis showed

piranha solution to be the most effective at increasing the APTS load. Decreases in pore volume and diameter indicates that grafting is occurring inside the pore framework. MASNMR showed that grafting occurs at the isolated and geminal sites and can dramatically change the surface composition to a 1:1 ratio of siloxane bridges to isolated silanols. Full hydrolysis of the APTS also occurred during grafting as no ethoxy carbons were detected using $^{13}C$ NMR. The potential for enhancing the grafting ability of silica materials by introducing a cleaning or pre-treatment step which impacts positively on potential lifetime and efficiency of the material has been shown.

## 3.6 References

[1] L.E. Blue, J.W. Jorgenson, 1.1μm Superficially porous particles for liquid chromatography Part 2: Column Packing and chromatographic performance, J. Chromatogr. A. 1380 (2015) 71–80. https://doi.org/10.1016/j.chroma.2014.12.055.

[2] V.K. Langsi, B. a. Ashu-Arrah, J.D. Glennon, Sub-2-μm seeded growth mesoporous thin shell particles for high-performance liquid chromatography: synthesis, functionalisation and characterisation, J. Chromatogr. A. (2015). https://doi.org/10.1016/j.chroma.2015.04.034.

[3] S.K. Natarajan, S. Selvaraj, Mesoporous silica nanoparticles: Importance of surface modifications and its role in drug delivery, RSC Adv. 4 (2014) 14328–14334. https://doi.org/10.1039/c4ra00781f.

[4] A.J. Crisci, M.H. Tucker, M. Lee, S.G. Jang, J.A. Dumesic, S.L. Scott, Acid-Functionalized SBA-15-Type Silica Catalysts for Carbohydrate Dehydration, ACS Catal. 1 (2011) 719–728. https://doi.org/10.1021/cs2001237.

[5] T. Yokoi, Y. Kubota, T. Tatsumi, Amino-functionalized mesoporous silica as base catalyst and adsorbent, Appl. Catal. A Gen. 421–422 (2012) 14–37. https://doi.org/10.1016/j.apcata.2012.02.004.

[6] J. Kim, H.S. Kim, N. Lee, T. Kim, H. Kim, T. Yu, I.C. Song, W.K. Moon, T. Hyeon, Multifunctional uniform nanoparticles composed of a magnetite nanocrystal core and a mesoporous silica shell for magnetic resonance and fluorescence imaging and for drug delivery, Angew. Chemie - Int. Ed. 47 (2008) 8438–8441. https://doi.org/10.1002/anie.200802469.

[7] M. Punzet, D. Baurecht, F. Varga, H. Karlic, C. Heitzinger, Determination of surface concentrations of individual molecule-layers used in nanoscale biosensors by in situ ATR-FTIR spectroscopy, Nanoscale. 4 (2012) 2431. https://doi.org/10.1039/c2nr12038k.

[8] V. Zelenak, D. Halamova, L. Gaberova, E. Bloch, P. Llewellyn, Amine-modified SBA-12 mesoporous silica for carbon dioxide capture: Effect of amine basicity on sorption properties, Microporous Mesoporous Mater. 116 (2008) 358–364. https://doi.org/10.1016/j.micromeso.2008.04.023.

[9] M. Pardakhti, T. Jafari, Z. Tobin, B. Dutta, E. Moharreri, N. Saveh Shemshaki, S.L. Suib, R. Srivastava, Trends in Solid Adsorbent Materials Development for CO 2 Capture , ACS Appl. Mater. Interfaces. 11 (2019) 34533–34559. https://doi.org/10.1021/acsami.9b08487.

[10] Y. Yin, Z.-F. Yang, Z.-H. Wen, A.-H. Yuan, X.-Q. Liu, Z.-Z. Zhang, H. Zhou, Modification of as Synthesized SBA-15 with Pt nanoparticles: Nanoconfinement Effects Give a Boost for Hydrogen Storage at Room Temperature, Sci. Rep. 7 (2017) 4509. https://doi.org/10.1038/s41598-017-04346-9.

[11] H.K. Chae, D.I. Siberio-Perez, J. Kim, Y. Go, M. Eddaoudi, A.J. Matzger, M. O'Keeffe, O.M. Yaghi, A Route to High Surface Area, Porosity and Inclusion of Large Molecules in Crystals, Nature. 427 (2004) 523–527. https://doi.org/10.1038/nature02294.1.

[12] D. Kumar, K. Schumacher, C. Du Fresne von Hohenesche, M. Grün, K.K. Unger, MCM-41, MCM-48 and related mesoporous adsorbents: their synthesis and characterisation, Colloids Surfaces A Physicochem. Eng. Asp. 187–188 (2001) 109–116. https://doi.org/10.1016/S0927-7757(01)00638-0.

[13] D. Zhao, Q. Huo, J. Feng, B.F. Chmelka, G.D. Stucky, Tri-, Tetra-, and Octablock Copolymer and Nonionic Surfactant Syntheses of Highly Ordered, Hydrothermally Stable, Mesoporous Silica Structures, J. Am. Chem. Soc. 120 (1998) 6024–6036.

[14] E.M. Borges, M.R. Euerby, An appraisal of the chemical and thermal stability of silica based reversed-phase liquid chromatographic stationary phases employed within the pharmaceutical environment, J. Pharm. Biomed. Anal. 77 (2013) 100–115. https://doi.org/10.1016/j.jpba.2013.01.013.

[15] P. Zucca, E. Sanjust, Inorganic Materials as Supports for Covalent Enzyme Immobilization: Methods and Mechanisms, Molecules. 19 (2014) 14139–14194. https://doi.org/10.3390/molecules190914139.

[16] J. Wang, H. Ge, W. Bao, Synthesis and characteristics of SBA-15 with thick pore wall and high hydrothermal stability, Mater. Lett. 145 (2015) 312–315. https://doi.org/10.1016/j.matlet.2015.01.113.

[17] A. Katiyar, S. Yadav, P.G. Smirniotis, N.G. Pinto, Synthesis of ordered large pore SBA-15 spherical particles for adsorption of biomolecules, J. Chromatogr. A. 1122 (2006) 13–20. https://doi.org/10.1016/j.chroma.2006.04.055.

[18] J.P. Thielemann, F. Girgsdies, R. Schlögl, C. Hess, Pore structure and surface area of silica SBA-15: influence of washing and scale-up, Beilstein J. Nanotechnol. 2 (2011) 110–118. https://doi.org/10.3762/bjnano.2.13.

[19] M. Thommes, R. Köhn, M. Fröba, Sorption and pore condensation behavior of pure fluids in mesoporous MCM-48 silica, MCM-41 silica, SBA-15 silica and controlled-pore glass at temperatures above and below the bulk triple point, Appl. Surf. Sci. 196 (2002) 239–

249. https://doi.org/10.1016/S0169-4332(02)00062-4.

[20] L. Snyder, J. Kirkland, J.W. Dolan, Introduction to modern liquid chromatography, 2009.

[21] K.K. Unger, Porous Silica Its Properties and Use as Support in Column Liquid Chromatography, Elsevier, 1979.

[22] H. Bergna, W. Roberts, Colloidal Silica: Fundamentals and Applications, CRC Press Taylor & Francis Group, 2007. papers2://publication/uuid/5C5D42D6-7FC8-488A-AB81-151CFB1FF4A9.

[23] M. Lazghab, K. Saleh, P. Guigon, Functionalisation of porous silica powders in a fluidised-bed reactor with glycidoxypropyltrimethoxysilane (GPTMS) and aminopropyltriethoxysilane (APTES), Chem. Eng. Res. Des. 88 (2010) 686–692. https://doi.org/10.1016/j.cherd.2009.11.005.

[24] D.R. Hristov, L. Rocks, P.M. Kelly, S.S. Thomas, A.S. Pitek, P. Verderio, E. Mahon, K.A. Dawson, Tuning of nanoparticle biological functionality through controlled surface chemistry and characterisation at the bioconjugated nanoparticle surface, Sci. Rep. 5 (2015) 1–8. https://doi.org/10.1038/srep17040.

[25] N.S.K. Gunda, M. Singh, L. Norman, K. Kaur, S.K. Mitra, Optimization and characterization of biomolecule immobilization on silicon substrates using (3-aminopropyl)triethoxysilane (APTES) and glutaraldehyde linker, Appl. Surf. Sci. 305 (2014) 522–530. https://doi.org/10.1016/j.apsusc.2014.03.130.

[26] D. a. Keane, J.P. Hanrahan, M.P. Copley, J.D. Holmes, M. a. Morris, A modified Stober process for the production of mesoporous Sub 2 micron silica microspheres; Applications in HPLC, J. Porous Mater. 17 (2010) 145–152. https://doi.org/10.1007/s10934-009-9274-

7.

[27] F. Gritti, G. Guiochon, Comparison between the loading capacities of columns packed with partially and totally porous fine particles. What is the effective surface area available for adsorption?, J. Chromatogr. A. 1176 (2007) 107–122. https://doi.org/10.1016/j.chroma.2007.10.076.

[28] J.O. Omamogho, J.P. Hanrahan, J. Tobin, J.D. Glennon, Structural variation of solid core and thickness of porous shell of 1.7μm core-shell silica particles on chromatographic performance: Narrow bore columns, J. Chromatogr. A. 1218 (2011) 1942–1953. https://doi.org/10.1016/j.chroma.2010.11.067.

[29] J.J. Lee, C.-J. Yoo, C.-H. Chen, S.E. Hayes, C. Sievers, C.W. Jones, Silica Supported Sterically Hindered Amines for CO2 Capture, Langmuir. 34 (2018) acs.langmuir.8b02472. https://doi.org/10.1021/acs.langmuir.8b02472.

[30] J. Nawrocki, The silanol group and its role in liquid chromatography, J. Chromatogr. A. 779 (1997) 29–71. https://doi.org/10.1016/S0021-9673(97)00479-2.

[31] F. Gao, A. V. Teplyakov, Challenges and opportunities in chemical functionalization of semiconductor surfaces, Appl. Surf. Sci. 399 (2017) 375–386. https://doi.org/10.1016/j.apsusc.2016.12.083.

[32] C. Cummins, D. Borah, S. Rasappa, A. Chaudhari, T. Ghoshal, B.M.D. O'Driscoll, P. Carolan, N. Petkov, J.D. Holmes, M.A. Morris, Self-assembly of polystyrene-block-poly(4-vinylpyridine) block copolymer on molecularly functionalized silicon substrates: Fabrication of inorganic nanostructured etchmask for lithographic use, J. Mater. Chem. C. 1 (2013) 7941–7951. https://doi.org/10.1039/c3tc31498g.

[33] J.. Cras, C.. Rowe-Taitt, D.. Nivens, F.. Ligler, Comparison of chemical cleaning methods of glass in preparation for silanization, Biosens. Bioelectron. 14 (1999) 683–688. https://doi.org/10.1016/S0956-5663(99)00043-3.

[34] J. Ruzyłło, Electrochemical Society. Electronics Division., F. Electrochemical Society. Meeting (192nd : 1997 : Paris, Cleaning Technology in Semiconductor Device Manufacturing, 1998.

[35] R.G. Acres, A. V. Ellis, J. Alvino, C.E. Lenahan, D.A. Khodakov, G.F. Metha, G.G. Andersson, Molecular structure of 3-aminopropyltriethoxysilane layers formed on silanol-terminated silicon surfaces, J. Phys. Chem. C. 116 (2012) 6289–6297. https://doi.org/10.1021/jp212056s.

[36] A. Sarkar, T. Daniels-Race, Electrophoretic Deposition of Carbon Nanotubes on 3-Amino-Propyl-Triethoxysilane (APTES) Surface Functionalized Silicon Substrates, Nanomaterials. 3 (2013) 272–288. https://doi.org/10.3390/nano3020272.

[37] C.J. Brinker, R. Sehgal, S.L. Hietala, R. Deshpande, D.M. Smith, D. Loy, C.S. Ashley, Sol-gel strategies for controlled porosity inorganic materials, J. Memb. Sci. 94 (1994) 85–102. https://doi.org/10.1016/0376-7388(93)E0129-8.

[38] N. Aissaoui, L. Bergaoui, J. Landoulsi, P. Vi, Silane Layers on Silicon Surfaces : Mechanism of Interaction , Stability , and Influence on Protein Adsorption, Langmuir. (2012) 656–665. https://doi.org/10.1021/la2036778.

[39] J. Landoulsi, M.J. Genet, S. Fleith, Y. Touré, I. Liascukiene, C. Méthivier, P.G. Rouxhet, Organic adlayer on inorganic materials: XPS analysis selectivity to cope with adventitious contamination, Appl. Surf. Sci. 383 (2016) 71–83.

https://doi.org/10.1016/j.apsusc.2016.04.147.

[40] K.K. Sharma, A. Anan, R.P. Buckley, W. Ouellette, T. Asefa, Toward efficient nanoporous catalysts: Controlling site-isolation and concentration of grafted catalytic sites on nanoporous materials with solvents and colorimetric elucidation of their site-isolation, J. Am. Chem. Soc. 130 (2008) 218–228. https://doi.org/10.1021/ja074128t.

[41] S. Brunauer, P.H. Emmett, E. Teller, Adsorption of Gases in Multimolecular Layers, J. Am. Chem. Soc. 60 (1938) 309–319. https://doi.org/citeulike-article-id:4074706\rdoi: 10.1021/ja01269a023.

[42] E.P. Barrett, L.G. Joyner, P.P. Halenda, The determination of pore volume and area distributions in porous substances. Computations from nitrogen isotherms, J. Am. Chem. Soc. 73 (1951) 373–380.

[43] A.G. Thomé, F. Schroeter, P. Bottke, J. Wittayakun, F. Roessner, Facile determination of the degree of modification of ordered mesoporous silica by liquid phase NMR, Microporous Mesoporous Mater. 274 (2018) 342–346. https://doi.org/10.1016/j.micromeso.2018.08.034.

[44] I.A. Rahman, M. Jafarzadeh, C.S. Sipaut, Synthesis of organo-functionalized nanosilica via a co-condensation modification using (gamma)-aminopropyltriethoxysilane (APTES), Ceram. Int. 35 (2009) 1883–1888. https://doi.org/10.1016/j.ceramint.2008.10.028.

[45] V. Hernández-Morales, R. Nava, Y.J. Acosta-Silva, S.A. MacÍas-Sánchez, J.J. Pérez-Bueno, B. Pawelec, Adsorption of lead (II) on SBA-15 mesoporous molecular sieve functionalized with -NH2 groups, Microporous Mesoporous Mater. 160 (2012) 133–142. https://doi.org/10.1016/j.micromeso.2012.05.004.

[46] K. Albert, E. Bayer, Review - Characterization spectroscopy, J. Chromatogr. 544 (1991) 345–370.

[47] M. Dulski, M. Laskowska, S. Sułowicz, T. Krzykawski, O. Pastukh, P.M. Zieliński, P. Pawlik, A. Nowak, Ł. Laskowski, The impact of the functionalization of silica mesopores on the structural and biological features of SBA-15, Microporous Mesoporous Mater. (2020) 110453. https://doi.org/10.1016/j.micromeso.2020.110453.

[48] Y. Wang, M. Noguchi, Y. Takahashi, Y. Ohtsuka, Synthesis of SBA-15 with different pore sizes and the utilization as supports of high loading of cobalt catalysts, Catal. Today. 68 (2001) 3–9. https://doi.org/10.1016/S0920-5861(01)00317-0.

[49] L.T. Zhuravlev, The surface chemistry of amorphous silica. Zhuravlev model, Colloids Surfaces A Physicochem. Eng. Asp. 173 (2000) 1–38. https://doi.org/10.1016/S0927-7757(00)00556-2.

[50] M. Sulpizi, M.P. Gaigeot, M. Sprik, The silica-water interface: How the silanols determine the surface acidity and modulate the water properties, J. Chem. Theory Comput. 8 (2012) 1037–1047. https://doi.org/10.1021/ct2007154.

[51] W.J. Van Ooij, D.Q. Zhu, G. Prasad, S. Jayaseelan, Y. Fu, N. Teredesai, Silane based chromate replacements for corrosion control, paint adhesion, and rubber bonding, Surf. Eng. 16 (2000) 386–396. https://doi.org/10.1179/026708400101517369.

[52] E. Costa Calleja, G. and Domingo, F., Adsorption of Gaseous Hydrocarbons on AC, AIChE J. 31 (1985) 9982–9991.

[53] X. Yuan, J.G. Lee, H. Yun, S. Deng, Y.J. Kim, J.E. Lee, S.K. Kwak, K.B. Lee, Solving two environmental issues simultaneously: Waste polyethylene terephthalate plastic bottle-

derived microporous carbons for capturing CO2, Chem. Eng. J. 397 (2020) 125350. https://doi.org/10.1016/j.cej.2020.125350.

[54] F. Sevimli, A. Yilmaz, Surface functionalization of SBA-15 particles for amoxicillin delivery, Microporous Mesoporous Mater. 158 (2012) 281–291. https://doi.org/10.1016/j.micromeso.2012.02.037.

[55] M. Ostwal, R.P. Singh, S.F. Dec, M.T. Lusk, J.D. Way, 3-Aminopropyltriethoxysilane functionalized inorganic membranes for high temperature CO2/N2 separation, J. Memb. Sci. 369 (2011) 139–147. https://doi.org/10.1016/j.memsci.2010.11.053.

## 3.7 Appendix – Chapter 3

**Table 3A.1. Normalised MASNMR. Data has been normalised to the Q4 peak for each sample.**

| Sample Name | Q4 | Q3 | Q2 | Q4 | Q3 | Q2 |
|---|---|---|---|---|---|---|
| | Cleaned | | | Functionalised | | |
| SBA-cal | 100 | 406 | 82 | | - | |
| SBA-APTS | | - | | 100 | 102 | 8 |
| Nitric 1h | 100 | 389 | 67 | 100 | 98 | 10 |
| Nitric 24h | 100 | 314 | 41 | 100 | 90 | 10 |
| Piranha 1h | 100 | 340 | 55 | 100 | 75 | 4 |
| Piranha 24h | 100 | 350 | 50 | 100 | 104 | 9 |
| UVO3 1h | 100 | 431 | 100 | 100 | 98 | 6 |
| UVO3 24h | 100 | 450 | 81 | 100 | 100 | 4 |
| Water 1h | 100 | 378 | 78 | 100 | 96 | 6 |
| Water 24h | 100 | 363 | 63 | 100 | 102 | 6 |

**Table 3A.2. Proton NMR results.**

| Proton NMR | | | | | | | | | | | |
|---|---|---|---|---|---|---|---|---|---|---|---|
| Sample | Time Cleaned | Acetate | | HOD | | H alpha | | H beta | | H gamma | |
| | | Position | Integral | Position | Integral | Position | Integral | Position | Integral | Position | Integral |
| SBA-cal | - | 1.07 | 1.00 | 4.91 | 2.64 | | | | | | |
| SBA-APTS | - | 1.1 | 1.00 | 4.94 | 2.43 | -0.53 | 0.44 | 0.6 | 0.44 | 1.69 | 0.37 |
| Nitric | 1 | 1.09 | 1.00 | 4.938 | 2.67 | | | | | | |
| | 24 | 1.08 | 1.00 | 4.94 | 2.92 | | | | | | |
| Piranha | 1 | 1.069 | 1.00 | 4.921 | 2.65 | | | | | | |
| | 24 | 1.063 | 1.00 | 4.921 | 2.91 | | | | | | |
| UVOzone | 1 | 1.08 | 1.00 | 4.94 | 2.62 | | | | | | |
| | 24 | 1.06 | 1.00 | 4.92 | 2.57 | | | | | | |
| Water | 1 | 1.08 | 1.00 | 4.94 | 2.87 | | | | | | |
| | 24 | 1.08 | 1.00 | 4.94 | 3.14 | | | | | | |
| Functionalised with APTS | | | | | | | | | | | |
| Nitric | 1 | 1.09 | 1.00 | 4.95 | 3.03 | -0.56 | 0.53 | 0.59 | 0.54 | 1.67 | 0.46 |
| | 24 | 1.076 | 1.00 | 4.92 | 3.49 | -0.567 | 0.5 | 0.578 | 0.5 | 1.661 | 0.42 |
| Piranha | 1 | 1.088 | 1.00 | 4.923 | 2.63 | -0.557 | 0.38 | 0.608 | 0.39 | 1.672 | 0.33 |
| | 24 | 1.07 | 1.00 | 4.92 | 2.91 | -0.57 | 0.5 | 0.57 | 0.5 | 1.66 | 0.41 |
| UVOzone | 1 | 1.1 | 1.00 | 4.94 | 2.26 | -0.54 | 0.41 | 0.63 | 0.42 | 1.69 | 0.37 |
| | 24 | 1.1 | 1.00 | 4.94 | 2.48 | -0.55 | 0.48 | 0.6 | 0.48 | 1.68 | 0.42 |
| Water | 1 | 1.075 | 1.00 | 4.916 | 2.21 | -0.569 | 0.38 | 0.575 | 0.38 | 1.659 | 0.33 |
| | 24 | 1.056 | 1.00 | 4.917 | 2.8 | -0.579 | 0.52 | 0.556 | 0.53 | 1.64 | 0.47 |

**Table 3A.3. Carbon NMR results.**

| $^{13}$C NMR | | | | | | | | | | | |
|---|---|---|---|---|---|---|---|---|---|---|---|
| Sample | Time Cleaned | Methyl | | Acetate | | alpha | | beta | | gamma | |
| | | Position | Integral | Position | Integral | Position | Integral | Position | Integral | Position | Integral |
| SBA-cal | - | 23.75 | 1.00 | 180.92 | 0.55 | | | | | | |
| SBA-APTS | - | 23.85 | 1.00 | 180.9 | 0.72 | 12.65 | 0.73 | 27.09 | 0.47 | 43.83 | 0.7 |
| Nitric | 1 | 23.79 | 1.00 | 180.94 | 0.44 | | | | | | |
| | 24 | 23.81 | 1.00 | 180.94 | 0.49 | | | | | | |
| Piranha | 1 | 23.8 | 1.00 | 180.92 | 0.46 | | | | | | |
| | 24 | 23.8 | 1.00 | 180.91 | 0.49 | | | | | | |
| UVOzone | 1 | 23.78 | 1.00 | 180.94 | 0.49 | | | | | | |
| | 24 | 23.8 | 1.00 | 180.91 | 0.47 | | | | | | |
| Water | 1 | 23.81 | 1.00 | 180.94 | 0.63 | | | | | | |
| | 24 | 23.83 | 1.00 | 180.93 | 0.6 | | | | | | |
| Functionalised with APTS | | | | | | | | | | | |
| Nitric | 1 | 23.86 | 1.00 | 180.87 | 0.49 | 12.65 | 0.74 | 27.09 | 0.65 | 43.82 | 0.74 |
| | 24 | 23.82 | 1.00 | 180.84 | 0.48 | 12.62 | 0.7 | 27.06 | 0.59 | 43.8 | 0.58 |
| Piranha | 1 | 23.85 | 1.00 | 180.88 | 0.61 | 12.65 | 0.59 | 27.09 | 0.65 | 43.82 | 0.57 |
| | 24 | 23.82 | 1.00 | 180.86 | 0.48 | 12.62 | 0.85 | 27.06 | 0.68 | 43.8 | 0.7 |
| UVOzone | 1 | 23.82 | 1.00 | 180.9 | 0.44 | 12.63 | 0.68 | 27.07 | 0.55 | 43.82 | 0.59 |
| | 24 | 23.83 | 1.00 | 180.89 | 0.6 | 12.63 | 0.62 | 27.07 | 0.73 | 43.81 | 0.72 |
| Water | 1 | 23.82 | 1.00 | 180.89 | 0.56 | 12.62 | 0.68 | 27.07 | 0.57 | 43.81 | 0.59 |
| | 24 | 23.81 | 1.00 | 180.86 | 0.52 | 12.61 | 0.76 | 27.05 | 0.71 | 43.79 | 0.84 |

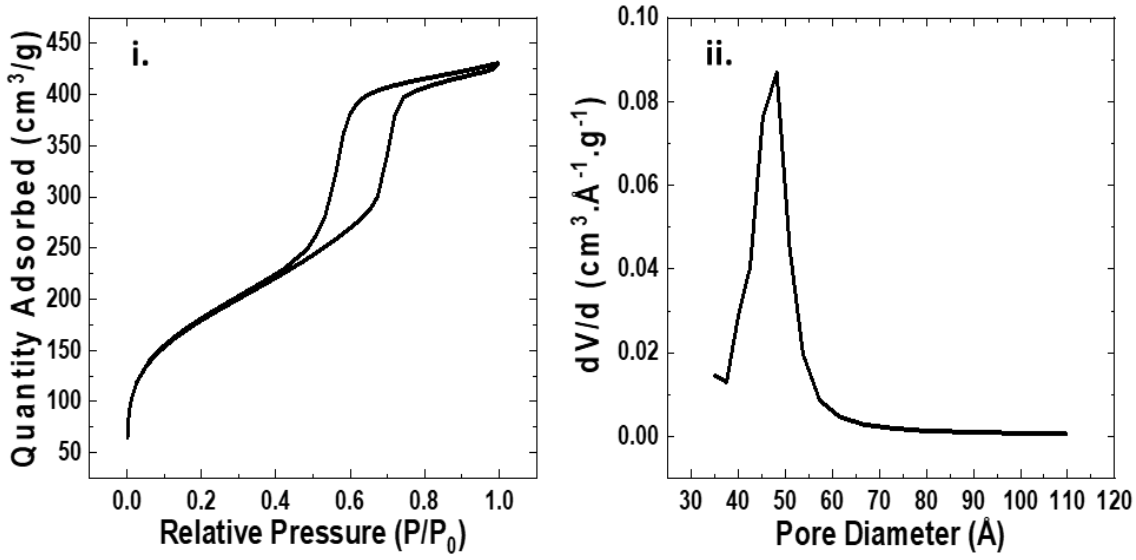


**Figure 3A.1:** **Analysis of physical properties of mesoporous SBA-15 material: (i) $N_2$ sorption isotherm of calcined SBA-15 showing type IV hysteresis loop typical of mesopores; (ii) BJH pore size distribution curve of calcined SBA-15 (desorption).**

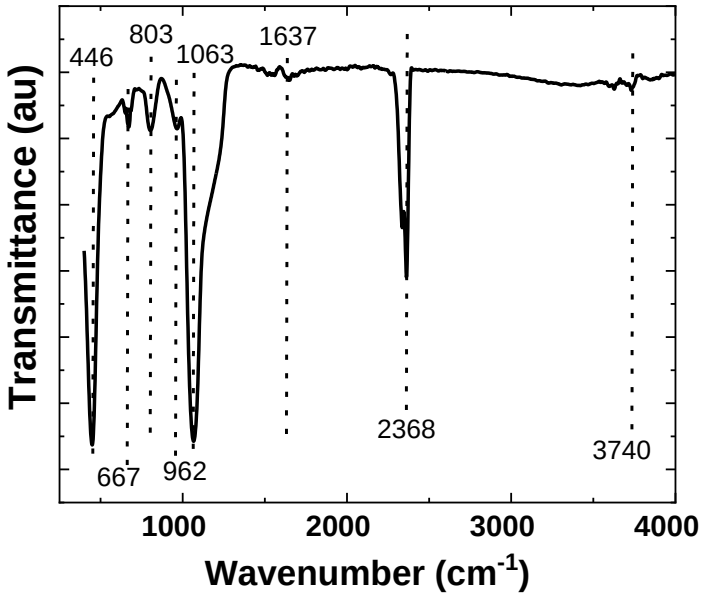


**Figure 3A.2: FTIR of calcined SBA-15.**

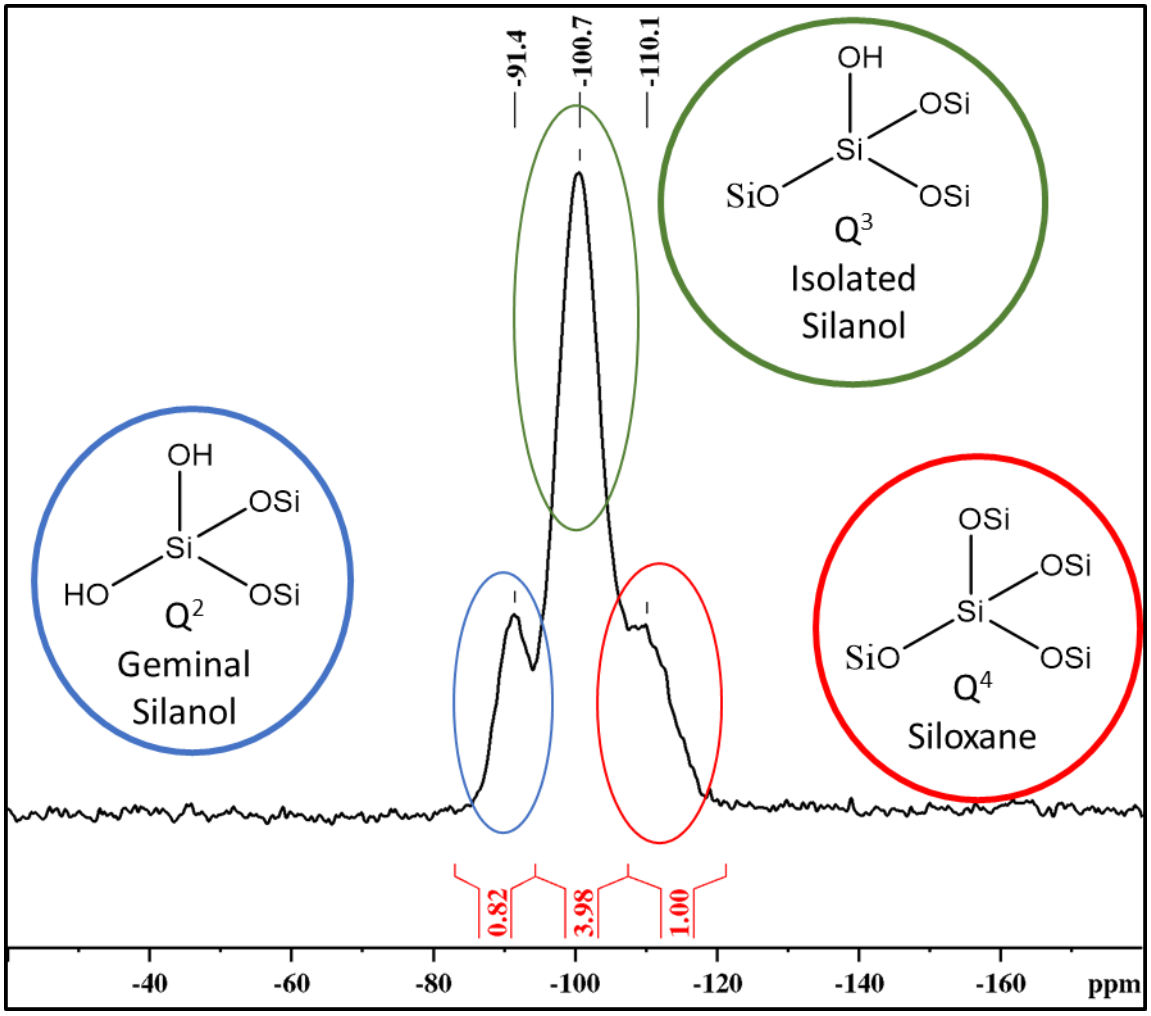


**Figure 3A.3:** **MASNMR $^{29}$Si spectra of calcined SBA-15 along with labelled peaks seen for different silicon environments present.**

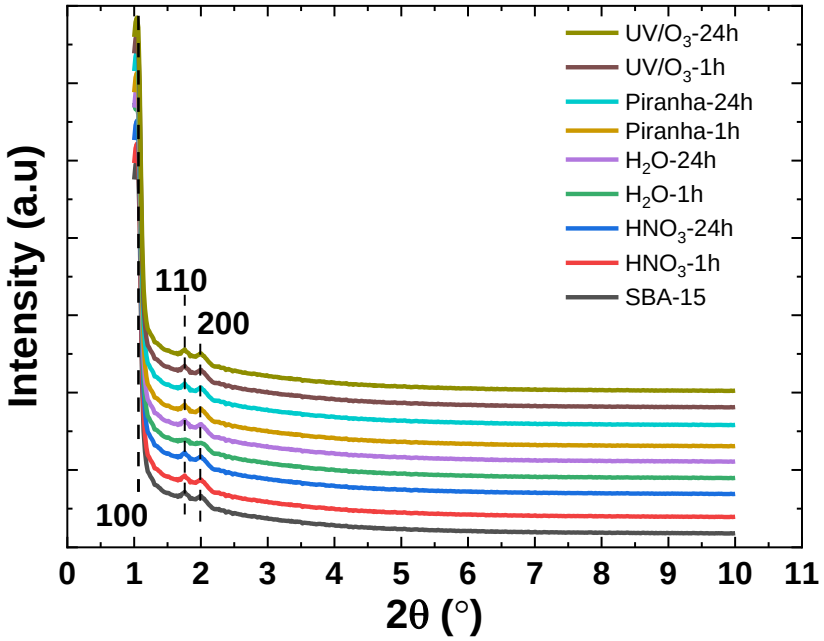


**Figure 3A.4:** **XRD of all samples cleaned along with bare SBA-15. Spectra show no change to crystal structure after any cleaning methods.**

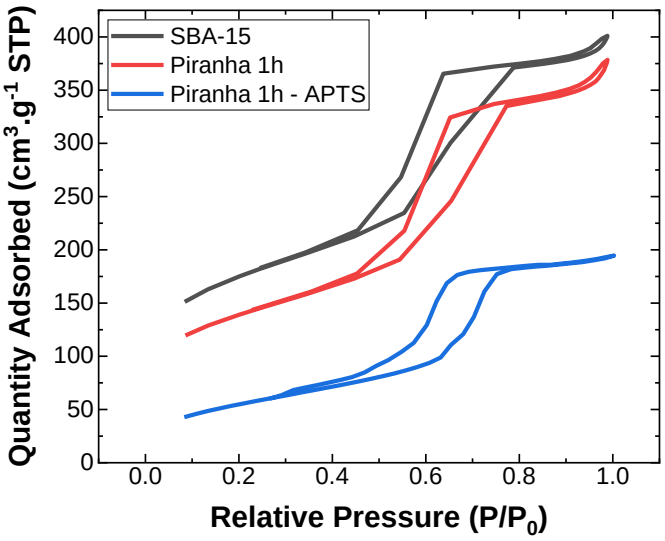


**Figure 3A.5:** **$N_2$ sorption analysis of quantity adsorbed of liquid nitrogen through different stages including bare SBA-15 (black), piranha solution cleaned SBA-15 (red) and SBA-15 which was cleaned with piranha solution and then functionalised with APTS (blue).**

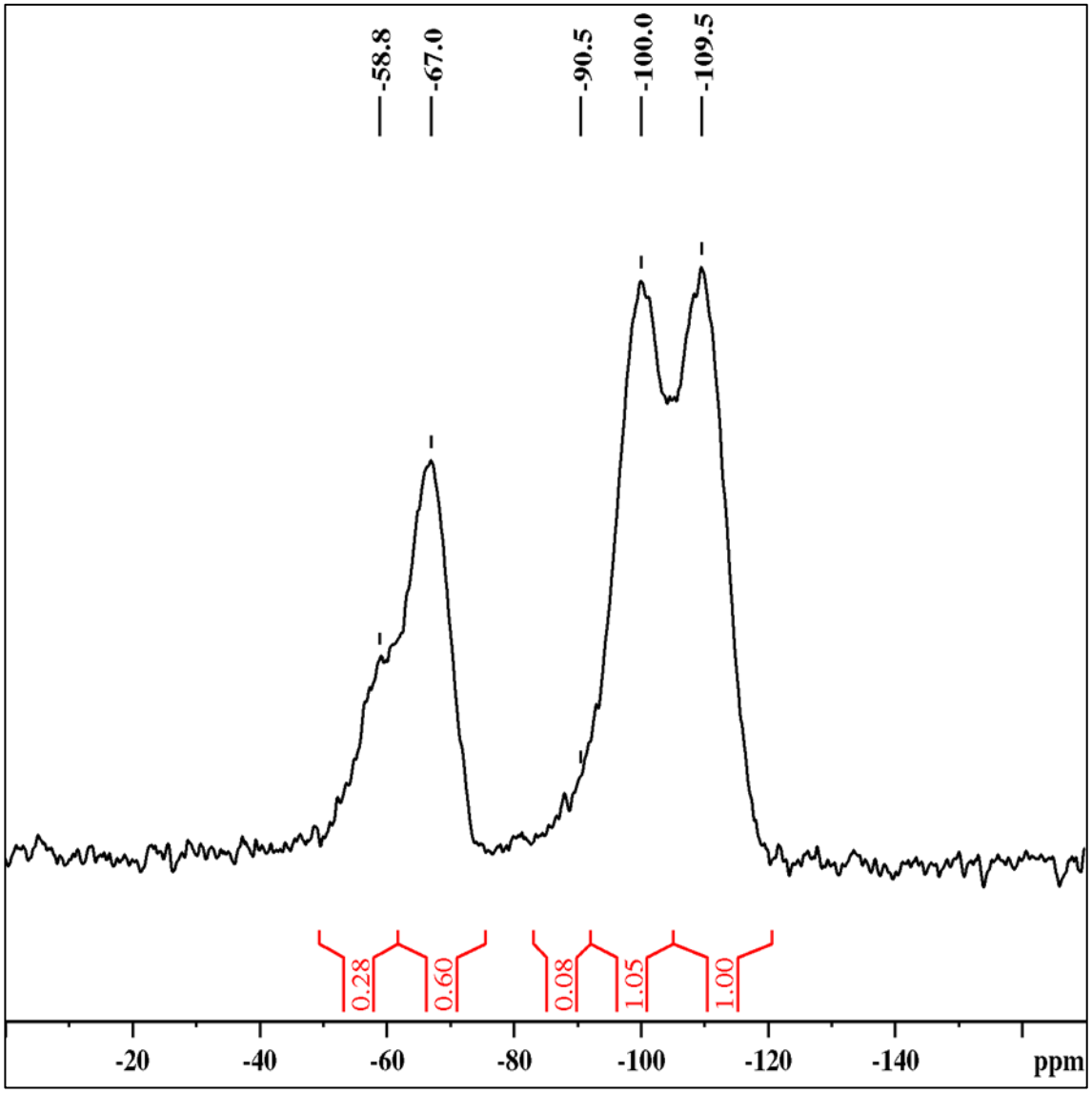


**Figure 3A.6.** **$^{29}$Si MASNMR spectra for SBA-15 sample which was cleaned with piranha solution for 1h and then functionalised with APTS. The spectra show Q4 peak (-109.5 ppm), Q3 peak (-100.0 ppm), Q2 peak (-90.5 ppm), T3 peak (-67.0 ppm) and T2 peak (-58.8 ppm).**

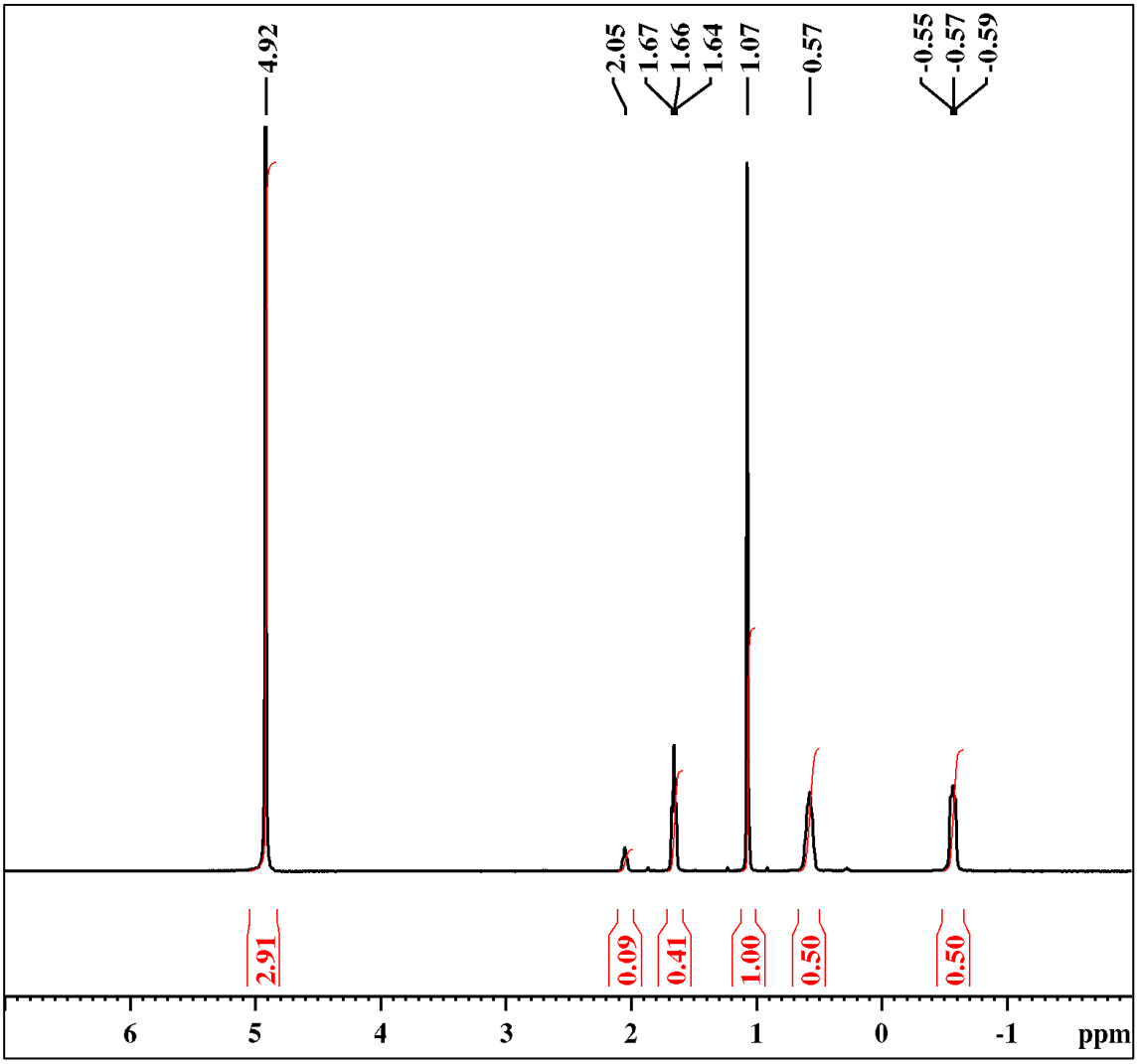


**Figure 3A.7.** **1H NMR spectra of 24-hour piranha solution cleaned SBA-15 which was then functionalised with APTS. The spectra shows the peaks which correspond to the grafted APTS peaks with are alpha proton (-0.57 ppm), beta proton (0.57 ppm), gamma proton (1.66 ppm) along with the standard acetate peak (1.07 ppm) and the HOD contribution (4.92 ppm).**

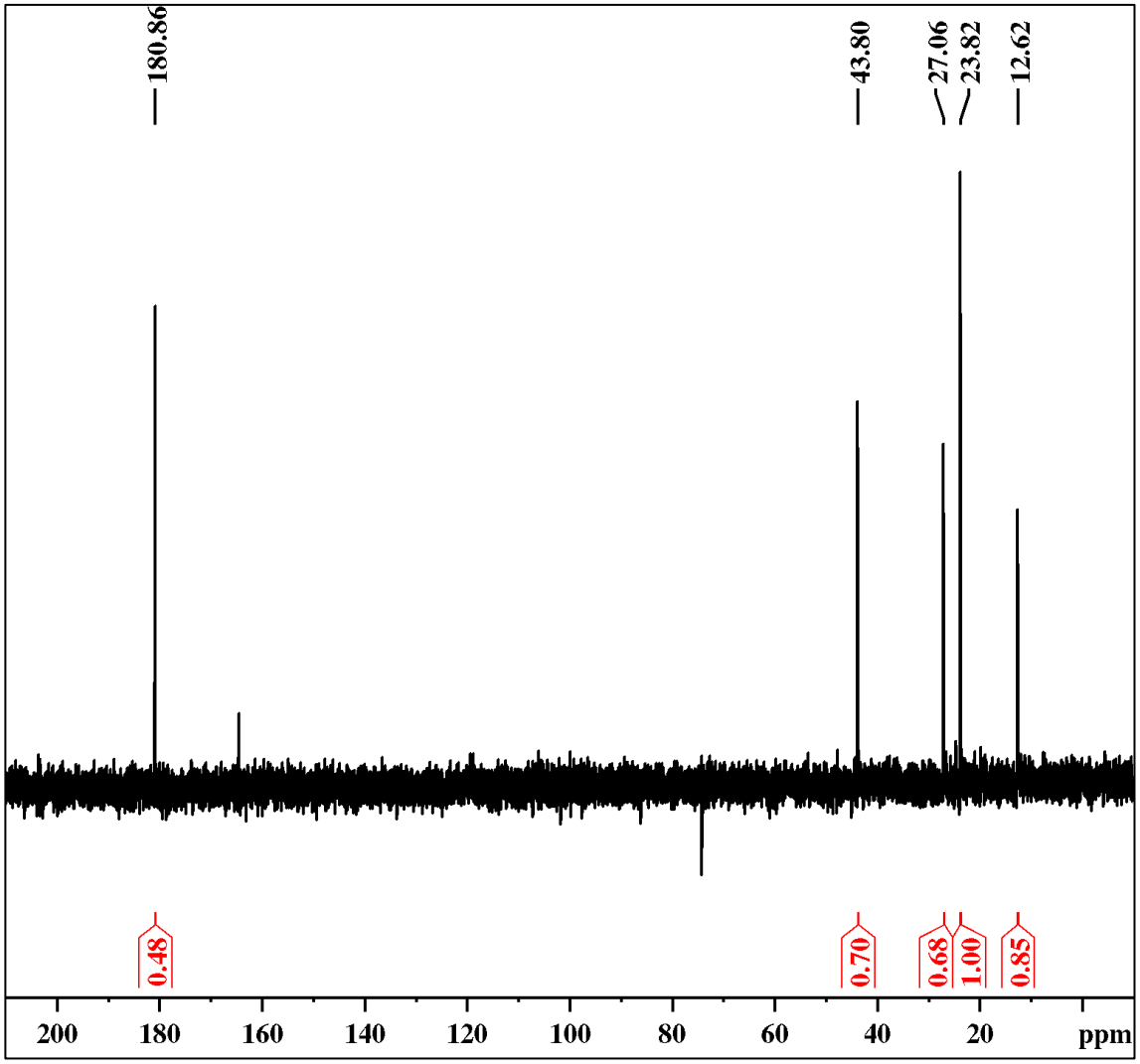


**Figure 3A.8.** **$^{13}$Carbon NMR spectra of 24-hour piranha solution cleaned SBA-15 which was then functionalised with APTS. The spectra shows the peaks which correspond to the grafted APTS peaks with are alpha carbon (12.62 ppm), beta carbon (27.06 ppm), gamma carbon (43.80 ppm) along with the methyl carbon peak (23.82 ppm) and the acetate carbon (180.86 ppm).**

# *Chapter 4*

# *Functionalisation and optimisation of ordered mesoporous silicas with hydroxy-terminated Poly-2-vinyl pyridine with metal salt infiltration*

## 4.1 Abstract

Polymers can be functionalised to silicas to enhance their properties and increase the potential to which they could play a vital role in future applications in many different products. Interest in mesoporous silicas are always increasing and in this study two different types are synthesized. MCM-41 and SBA-15 are synthesized, and their physical properties are determined using $N_2$ sorption and x-ray diffraction along with FTIR. The polymer poly-2-vinyl pyridine (hydroxy terminated) is grafted to mesoporous silicas to attach a long alkyl chain with an interest in the active pyridine functional group. The nitrogen of the pyridine group is in the ortho position. The optimal concentration for the grafting process was determined for both mesoporous silicas using elemental analysis. 2 k polymer weight was optimal for MCM-41 while 4-6 k polymer weight was for SBA-15. The grafted support then underwent metal salt inclusion. Cerium metal salt was examined. The surface was analysed using x-ray photoelectron spectroscopy (XPS) to determine the metal concentration. These metal infiltrated samples were imaged using transmission electron microscopy (TEM) and scanning electron microscopy (SEM).

## 4.2 Introduction

Porous silicas make up a large proportion inside the sphere of porous materials and are widely studied due to their applications in multiple fields such as catalysis[1–4], drug delivery[5–8], bioimaging[9], sensing[10]/biosensing[11–13], adsorption[14–21] and separations[22–24]. Its large benefits which include their high mechanical strength, tuneable pore size and varying high surface areas[25]. Other widely studied porous materials such as MOFs[26,27] and zeolites compete with mesoporous molecular sieves for other applications in gas sensing and storage and as new adsorbent materials[28]. Mesoporous materials (MCM-41, MCM-48, SBA-15 etc.) have been considered as ideal catalytic and adsorption supports due to their high surface area and thermal stability and uniform interconnected pores which offer an interaction between catalysts

and reactants. Along with these well-defined pores and enhanced accessibility, their ability to anchor diverse chemical functionalities on their surface provides added benefit to other porous materials.

MCM-41 a member of the M41S family of molecular sieves was first synthesized by Mobil Oil as an experiment to synthesize organic-inorganic adsorbents or supports with the ability to fine tune properties[29]. MCM-41 has one-dimensional channel system[30] in the range of 2-10 nm depending on the template used and has a two-dimensional hexagonal arrangement of the mesopores[31]. It is the most studied of the MCM family due to others being less thermally stable or different physical properties like that of MCM-48 which has a cubic arrangement of its mesopore structure[31].

Stucky et al synthesized a similar material which also consisted of a two-dimensional (p6mm) hexagonal array of pores called Santa Barbara Amorphous (SBA) [32]which has attracted the interest of many researchers due to their well-defined pore structure, large pore size (4.6–30 nm), inert framework, thick pore wall and high thermal and hydrothermal stability[33]. All these advantages make them suitable candidates for many applications in catalysis, adsorption, immobilization, drug delivery and separation techniques. SBA-15 has attracted more attention among different mesoporous silica structures due to their desirable properties such as thick pore wall and hexagonal mesopores (4–12 nm), high surface area, ease of synthesis and functionalization and high thermal and mechanical stability.

As with all silicas, different functional moieties can be introduced to the support framework by incorporating different functional ligands either directly by co-condensation[34–36] during synthesis or by a post grafting step[20,30]. Grafting of the mesoporous silicas surface with various functional groups (i.e. amines, thiol, nitriles, epoxides etc.) has been studied by various researchers

in the past all to add applications to the area of porous silicas[37–43]. Their ability to be readily modified with different functional groups is due to the presence of surface silanol groups[44–46].

The popularity of porous materials aside from their adventitious physical properties, is due to the relative ease of functionalisation with a vast array of alkoxysilanes with different terminal functional groups and chemistries. Mesoporous silicas must be functionalised and in turn offers stability and as a stable support for the now active layer on the material. Grafting occurs at surface silanol (Si-OH) sites and with careful optimization of parameters, functional layers can be attached which offer excellent coverage of the functional moiety. Most of the functionalisation of porous materials comes from the attachment of organosilane compounds which forms a very stable Si-O-Si bond. The grafting mechanism typically will follow the hydrolysis and condensation of the alkoxysilane but is sometimes dependent on the terminal functional group or groups throughout attached layer. Therefore, careful consideration must be placed on the surface chemistry to allow the deposition of a dense polymer layer. The polymer chosen in this study was hydroxy-terminated poly-2-vinyl pyridine (P2vP-OH) which would allow dehydration and in turn produce the necessary grafting of the polymer to the mesoporous support. This would mimic the normal grafting route.

Polymer and brush films have been studied with mesoporous silicas[47]. Marcoux et al produced mesoporous polymer composites with poly(chloromethyl styrene) PCMS and poly(glycidyl methacrylate) PGMA[48]. Chen et al prepared mesoporous SBA-15 materials which were derivatised with PGMA and poly(glycidyl methacrylate)-b- poly(methyl methacrylate) PGMA-PMMA[49]. Liu et al grafted poly-4-vinyl pyridine (P4vP) to mesoporous silica as a pH-sensitive controlled release device for therapeutics[50].

Two key requirements for effective catalysis are high activity and conversion rates. For better catalytic activity, supports require higher surface area and good metal dispersion. A lot of research

into metal dispersion occurs in the semiconductor manufacturing environment where processes such as sequential infiltration synthesis (SIS), metal salt infiltration (MSI) and aqueous metal reduction are common[51,52]. These processes typically occur on silicon wafer substrates and in the case of block co-polymers (BCPs) a layer of the biopolymer is grafted to the wafer's surface. The BCP then acts as an infiltration site for the interested metal. In the case of semiconductors this produces finely ordered features in the nanometre range. In the case of BCPs, the metal has a higher affinity toward one of the polymers. Metal infiltration then occurs selectively on one polymer and not on the other. In the case of poly-2-vinyl pyridine (P2vP), the N group at the centre of the pyridine ring, interacts with the metal cation which facilitates the infiltration. This has been shown to provide good metal dispersion (pyridine at regular points in the polymer chain) which adds to the effectiveness of the potential catalyst.

In this study, metal infiltration occurs as there is an affinity from the metal ion to the organic polymer layer which is with the P2vP. Metals can form an interaction with the nitrogen in the pyridine ring. The nitrogen can coordinate with the metal(s) and in turn attach to the support. The polymer layer can then be removed by multiple methods including plasma cleaning, calcination and can convert the metal to a different oxide. This can further incorporate other functional moieties and layers if required by grafting with silanes or other reactive ligands.

Many different metals supported silicas have been shown to increase the catalytic ability of some transformations leading to 100% conversions and greater than 90% selectivity's. Transition metal which include Ru, Pt, Pd, Au, Ag, Cu, Ni have all been incorporated into mesoporous silicas to carry out catalytic conversions of organic species.

In this report we outline the optimization of grafting the hydroxy terminated polymer poly-2-vinylpyridine to two classes of mesoporous silicas, SBA-15, and MCM-41. The silicas were initially synthesised and characterised. After functionalisation with the polymer the silicas were

characterised using elemental analysis to determine the quantity loaded. Electron microscopy was used to observe any changes in structure and x-ray diffraction was used determine the crystallinity of the new material. Finally, metal salts are infiltrated into the polymer layer and the surface composition is analysed using X-ray photoelectron spectroscopy throughout the infiltration stage and in the removal of the polymer. Electron microscopy was also used to image this new material.

## 4.3 Materials & Methods

### *4.3.1 Materials*

Pluronic 123 (Poly(ethylene glycol)-block-poly(propylene glycol)-block-poly(ethylene glycol), tetraethyl orthosilicate (>99%), hydrochloric acid (ACS reagent 37%), 2-propanol (CHROMASOLV, for high performance liquid chromatography [HPLC], 99.9%), hexadecyltrimethylammonium bromide [CTAB] (>98%), ammonium hydroxide (ACS Reagent 28.0-30.0 wt.%), ethanol (anhydrous >99.5%) were all purchased from Sigma Aldrich, Ireland. Tetrahydrofuran (99.8 % HPLC grade) was purchased from Fisher Scientific, UK. Poly-2-vinylpyridine-hydroy-terminated of varying sizes (2k, 4k, 6k, 10k, 16k) were purchased from Polymer Source Inc. Montreal, Canada. Ammonium cerium (IV) nitrate (99.99% trace metals basis) was purchased from Sigma Aldrich, Ireland.

### *4.3.2 Methods*

#### 4.3.2.1 Synthesis of mesoporous silicas

The preparation of silica SBA-15 was achieved by following the procedure reported by Zhao et al. 8.0 g of Pluronic 123 was stirred in 60 mL of deionised water at 40 °C until fully dissolved. 116.5 mL of 2 $molL^{-1}$ HCl was added followed by the dropwise addition of 17.6 mL TEOS (tetraethyl orthosilicate). The reaction solution was the transferred into a sealed bottle to be autoclaved at 90 °C for 48 h without stirring. The white product was filtered off and washed with

deionised water. The solid was then dried and calcined at 550 °C for 6 h. Any mention of SBA-15 from this point on will have been as synthesised and calcined. Within this chapter, SBA was synthesised once and therefore no replicates were made.

The preparation of MCM-41 was carried out using method described by Kumar et al. 4.8 g of hexadecyltrimethylammonium bromide (CTAB) was dissolved in 240 g of deionised water by stirring. 16 mL of ammonium hydroxide solution was added and stirred for 10 min when 20 mL TEOS was then added. The solution mixture was stirred overnight for 18 h and then filtered. It was washed with equal aliquots of ethanol and water three times. The resulting powder was then calcined for 8 hours at 550 °C. Enough MCM-41 was synthesised in this batch and as such no replicates were made for this chapter.

#### 4.3.2.2 Functionalisation of mesoporous supports with P2vP

The grafting of P2vP-OH to mesoporous silicas was carried out to determine the optimal polymer weight for functionalisation. 3 % w/w solutions of poly-2-vinyl pyridine in THF were made up to a volume of 8 mL. 0.25 g of mesoporous silica (SBA-15/MCM-41) was measured and added to the flask. The reaction was stirred at 62 °C for 90 min. The resulting product was filtered and washed with tetrahydrofuran. As a control, the two mesoporous silicas were also stirred in THF at 62 °C for 90 min and then filtered and washed with THF.

#### 4.3.2.3 Metal infiltration of SBA-P2vP with Ce

SBA-15 functionalised with P2vP was infiltrated with cerium metal. The ammonium cerium (IV) nitrate salt was placed into absolute ethanol and dissolved overnight with constant stirring. Different concentrations were examined. A mass of 0.25 g of SBA-15 was measured and added to the dissolved solution of the salt and stirred for 24 h at room temperature. The resulting product

was filtered, washed with ethanol, and dried in an oven set at 50 °C overnight. Control samples including SBA-15 were also examined.

### *4.3.3 Characterisation techniques*

#### 4.3.3.1 X-ray photoemission spectroscopy (XPS)

X-ray photoelectron spectroscopy was performed under ultra-high vacuum conditions ($<5x10^{-8}$ mbar) on a VG Scientific ESCAlab Mk II system equipped with a hemispherical analyser using Al Kα x-rays (1486.6 eV). The emitted photoelectrons were collected at a take-off angle of $90^0$ from the disks' surface. The analyser pass energy for the survey scans was 200 eV. The binding energy scale was referenced to the adventitious carbon 1s core level scans at 284.8 eV. Core level scans of Si 2s, C 1s, N 1s and O 1s were examined along with Ce 3d.

#### 4.3.3.2 Electron microscopy

Scanning electron microscopy (SEM) was carried out using a Karl Zeiss Ultra Plus field emission SEM with Gemini column. The technique was used to provide detailed visual information on the external surface morphology. An in-lens detector was used. The samples were placed on carbon tape and then adhered to a stainless-steel stub before being placed in the instrument's chamber. It was operated at 5 KeV and various magnifications were used as required. Transmission electron microscopy (TEM) was used to provide detailed images of the internal structure of the synthesised mesoporous silica. The samples were sonicated in HPLC grade water and dropped on support films of lacey carbon with 200 mesh copper grids. The TEM used was a JOEL 2100 operating at 200 kV. The images were acquired in bright field mode.

#### 4.3.3.3 Fourier transform infra-red (FT-IR)

Fourier transform infra-red spectroscopy was performed using a Bruker Tensor II (mid-range extended with diamond UATR) and was collected using an attenuated total reflection infrared accessory. Spectra of the SBA-15 at various stages of the process were recorded in the range 400 $cm^{-1}$ to 4000 $cm^{-1}$.

#### 4.3.3.4 $N_2$ sorption analysis

The surface area, pore diameter, pore volume and pore size distribution measurements of the samples were performed based on the sorption technique using the Micromeritics Tristar II surface area analyser (Micrometrics, Norcross, GA, USA). The specific surface area was calculated using the multi-point Brunauer, Emmett and Teller (BET) method in the relative pressure range $P/P_0$ = 0.05-0.3. The specific pore volume, pore diameter and pore size distribution curves were computed based on the Barrett-Joyner-Halenda (BJH) method. Nitrogen gas was used. The sorption analysis carried out was measured at 77 K. Each sample was degassed under nitrogen for five hours at 200 ˚C prior to analysis.

#### 4.3.3.5 Elemental analysis

Elemental analysis took place on mesoporous silicas after grafting and after removal of the polymer layer. SBA-15 and MCM-41 were examined to determine the percentage carbon and nitrogen in the sample after grafting to understand the optimum level of attachment. The analysis was performed on Elementar vario EL cube elemental analyser. All samples analysed were ran in triplicate. Furthermore, samples were measured after samples were calcined after metal infiltration to prove all the P2vP layer had been removed.

#### 4.3.3.6 X-ray diffraction (XRD)

X-ray diffraction (XRD) patterns have been recorded with a Bruker D8 Advance diffractometer equipped with an un-monochromated Cu-$K_\alpha$ source with a 1D detector which includes an energy discriminator which filters out Cu-$K_\beta$. Samples were ran in the low angle range from 0.5˚ to 5˚ ($0.5^\circ \leq \theta \geq 5.0^\circ$).

## 4.4 Results and discussion

### *4.4.1 Characterisation of synthesized silicas.*

Electron microscopy was carried out on both calcined SBA-15 (SBA15-cal) and calcined MCM-41 (MCM41-cal). The SEM micrographs of different magnifications are shown in figure 4.1(a-f). The SBA-15 (figure 4.1[a-c]) and MCM-41 (figure 4.1[d-f]) both look very similar from the figures. Both have no well-defined morphology or size, but the individual particles all appear to be smaller than 150 μm in size. The SBA-15 seems to be an accumulation of much larger particles compared with the MCM-41 particles. The MCM-41 particles look smaller in size with the largest based on the SEM images estimating to be no bigger in diameter than 80 μm but many seem much smaller than this. The SBA-15 looks more rigid with a more crystalline edge compared with the majority of MCM-41 particles, looking much fluffier and as though more aggregation of smaller particles combined.

TEM results are shown in the same figure 4.1 indicating SBA-15 particles (g) and MCM-41 (h-i). The TEM image for SBA-15 (g) show the highly ordered pore channels which run parallel to each other in the right foreground along with the left background of the image. The TEM image also show the ordered hexagonal pore structure which runs from the end-on side of the particles. This is shown inset in the top right corner of the image. The same structure is seen for MCM-41as described for SBA-15 just seen on higher magnification. Figure 4. (h) shows the hexagonal pore

structure of MCM-41 and (i) shows the ordered pore channels running parallel to each other although curved.

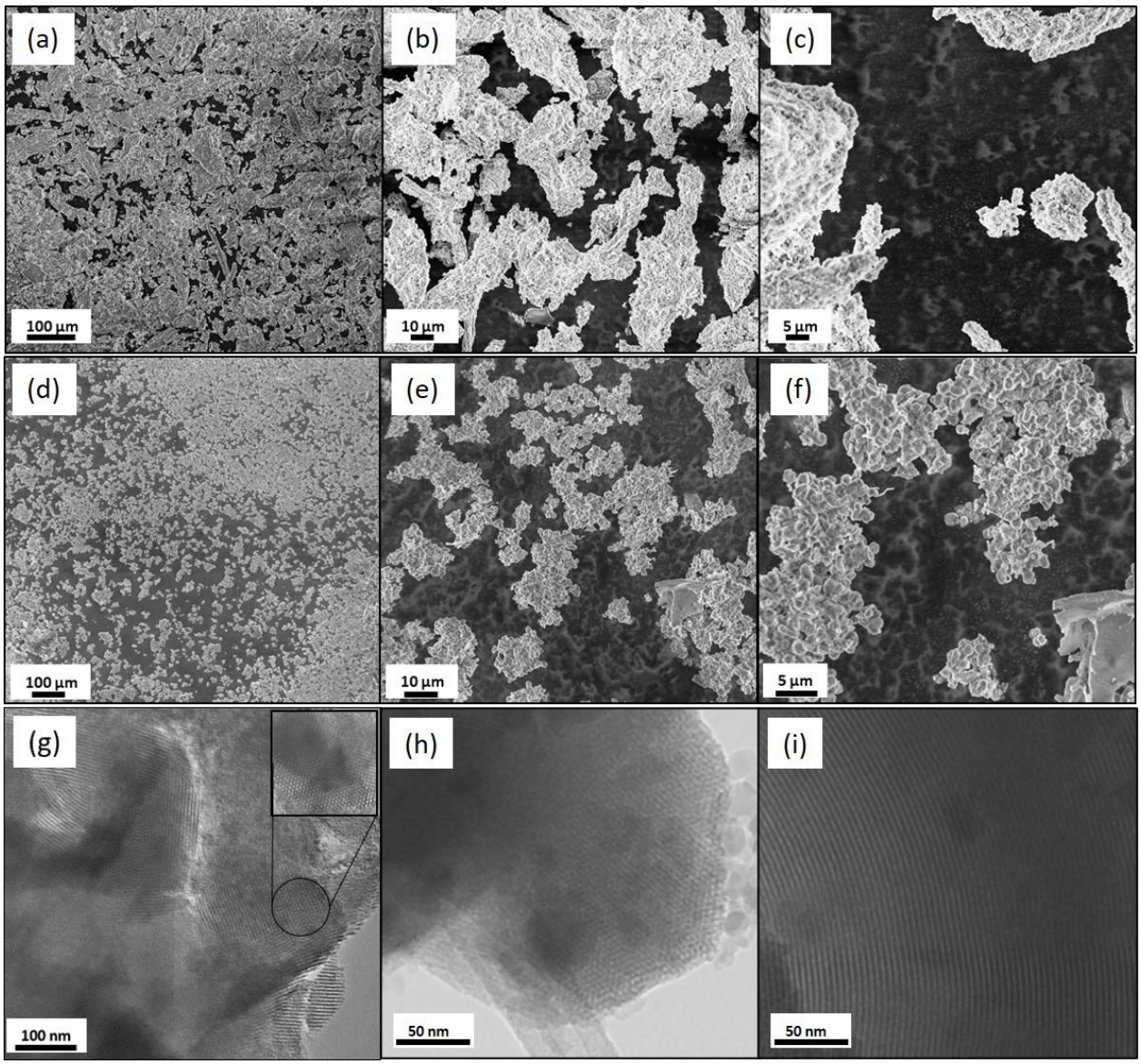


**Figure 4.1: Electron microscopy images. SEM images of SBA-15 at different magnifications (a-c), SEM images of MCM-41 at different magnifications (d-f), TEM image of SBA-15 (g) and TEM images of MCM-41 (h-i).**

The $N_2$ sorption isotherm was measured for both SBA-15 and MCM-41 and is displayed in figure 4.2. For both curves, a type IV isotherm with a typical hysteresis which indicates mesopore structure. The MCM-41 curve is very much a H1 type hysteresis loop which is described by the

vertical and parallel lines[53]. This is compared with the SBA-15 curve which is someway between a H1 and H2 loop due to the more horizonal line shape which is also not fully parallel. This indicates that the mesopores are not completely uniform and that there is a change as $N_2$ is adsorbed (lower red curve) and desorbs (higher red curve) from the surface of the SBA-15[54].

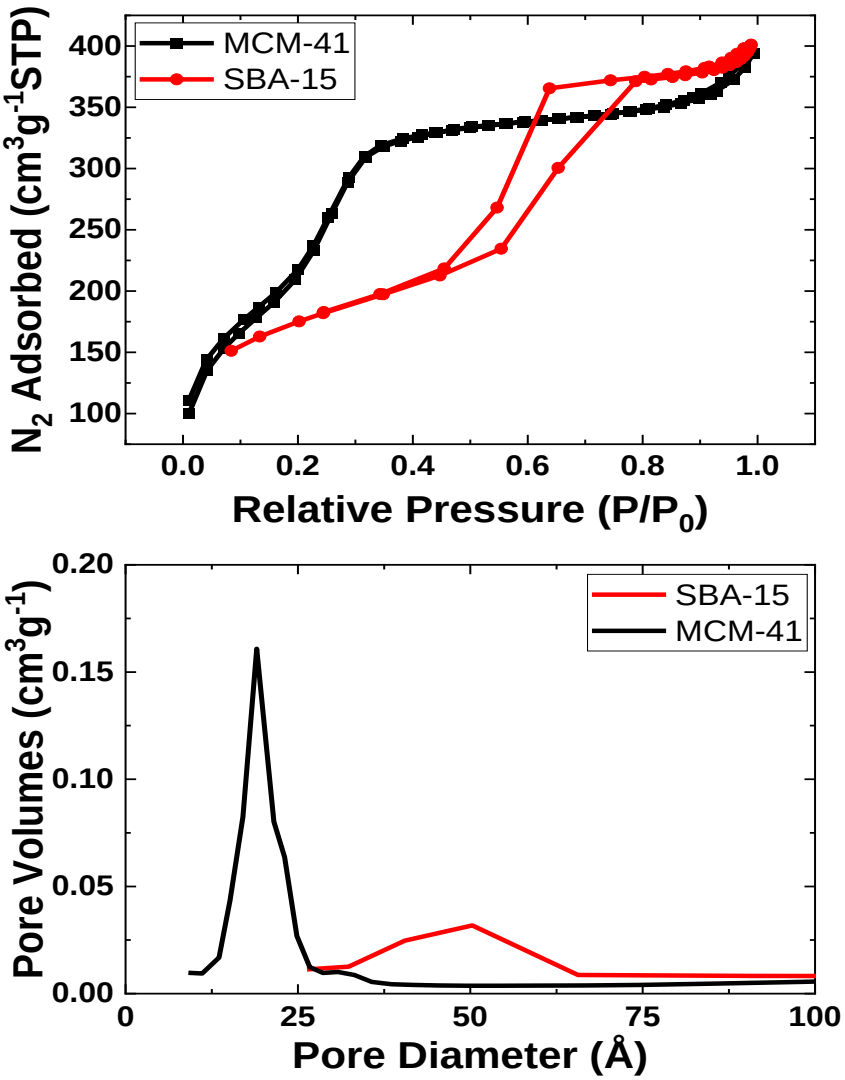


**Figure 4.2:** **Nitrogen adsorption-desorption isotherms (TOP) of synthesised mesoporous silicas SBA-15 (red) & MCM-41 (black) and the pore size distribution (BOTTOM) of both mesoporous silicas.**

The physical properties for both synthesised SBA-15 and MCM-41 are displayed in table 4.1. It displays surface areas of MCM-41 and SBA-15 to be 1005 and 611 $m^2g^{-1}$, respectively. The pore volume was higher for SBA-15 at 0.56 $cm^3g^{-1}$ than MCM-41 at 0.46 $cm^3g^{-1}$. This is typical as SBA-15 has larger and more interconnections between the cylindrical pore structure compared with MCM-41 which normally consists of unidirectional pores[53]. This then leads onto pore diameter, which for SBA-15 is much larger than MCM-41. SBA-15 pore diameter was determined at 48 Å and MCM-41 was 26 Å. The pore size distribution of both MCM-41 and SBA-15 are also displayed in in the bottom half of figure 4.2. Here it can be seen that the pore diameter of both are plotted against the pore volume. The pore diameter of MCM-41 is very narrow and small and shows that the pore volume is below 25 Å which agrees with the overall average pore diameter value shown and already discussed at 26 Å. The pore size distribution of the SBA-15 is misleading from the plot as the pore size is quite narrow but when compared with the MCM-41, it is quite broad. This would agree with the general synthesis of SBA-15 when compared to MCM-41 which has a narrow pore diameter range and has typically much smaller pores[55].

**Table 4.1: Physical properties of silicas SBA-15 & MCM-41 determined using $N_2$ sorption.**

| **Sample** | **Surface Area** $m^2g^{-1}$ | **Pore Volume** $cm^3g^{-1}$ | **Pore Diameter** *Å* |
|---|---|---|---|
| MCM-41 | 1005 | 0.46 | 26 |
| SBA-15 | 611 | 0.56 | 48 |

Powder X-ray diffraction results of both SBA-15 and MCM-41 are displayed in figure 4.3. The low angled spectra shown displays three points which relate to the (1 0 0), (1 1 0) and (2 0 0) lattice points which indicate the p6mm structure associated with the hexagonal framework of both mesoporous silicas[56–58]. It is obvious and clear from looking at the spectra that the MCM-41peaks are much more pronounced compared with the clear (1 0 0) point for SBA-15 but the two

shoulder points for the (1 1 0) and (2 0 0). This would indicate that there is a more crystalline lattice structure for the MCM-41 compared with the SBA-15.

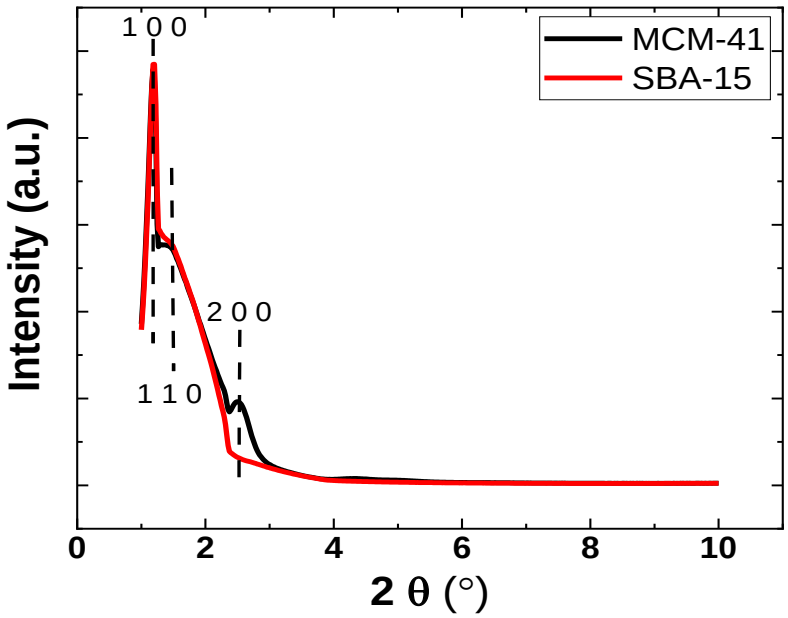


**Figure 4.3: XRD pattern for mesoporous silicas MCM-41 and SBA-15.**

### *4.4.2 Functionalisation of silicas with P2vP*

Elemental analysis results for the grafting of P2vP-OH are seen in figure 4.4. Percentage carbon and nitrogen are displayed showing the impact of the functionalisation step. The polymer weight noted is the minimum size of the polymer over a wide variance. Functionalisation of both SBA-15 and MCM-41 with poly-2-vinyl pyridine occurred. Elemental analysis of both mesoporous silicas which underwent functionalisation without the polymer present showed a percentage carbon and nitrogen of 0.05 % and 0.02 %, respectively.

An increase in percentage carbon and nitrogen associated with grafting of P2vP is seen for all derivatised samples. Firstly, examining SBA-15 (figure 4.4a), the percentage carbon result show

that there was an increase in percentage carbon to 11.77 % from the 2k polymer weight to 14.99 % for the 4k polymer weight. The percentage carbon slightly decreases within error to 14.93 % and plateaus for the 6k polymer weight. A decrease in percentage carbon is then seen as the polymer weight increases to 10 and 16k polymer weight at 13.36 % and 8.99 % of carbon, respectively. This follows a trend shown by Lundy et al in which they grafted poly-2vinyl pyridine to silicon substrates[59]. Using XPS in their case it was seen to follow the same trend to 6k polymer weight and then dropped significantly at higher molecular weights. The potential reason for this reduction in grafting is due to π-π stacking interactions between overlapping nitrogen groups in the pyridine rings. As the polymer weight increases there becomes more interactions with more cluttered pyridine rings as demonstrated by Sieranski et al[60]. This interaction causes more agglomeration and in turn reduces the coverage of the polymer. This is seen from the percentage carbon result which shows and links the quantity of the polymer functionalised onto the mesoporous silica surface. This was also demonstrated by Lundy et al[61] using AFM on a flat silicon wafer surface which underwent grafting by poly-2-vinyl pyridine and other block-co-polymers. AFM in conjunction with contact angle measurements showed coverage using the Cassie-Baxter model. This showed the uniform grafted layer on the surface of the wafer substrate. The percentage nitrogen results for SBA-15 also follows the same trend as the carbon component. There is the initial increase from 2k to 4k with a plateau at 6k and then the decrease down at 10k and 16k.Another potential reason for the large reduction in grafting coverage could be due to the larger polymer weights not being able to enter the hexagonal pore structure and attach to the silica support. XPS could also have been used to determine the degree of P2vP attachment. It was used as a qualitative measure to show polymer derivatisation by the presence of nitrogen at the surface.

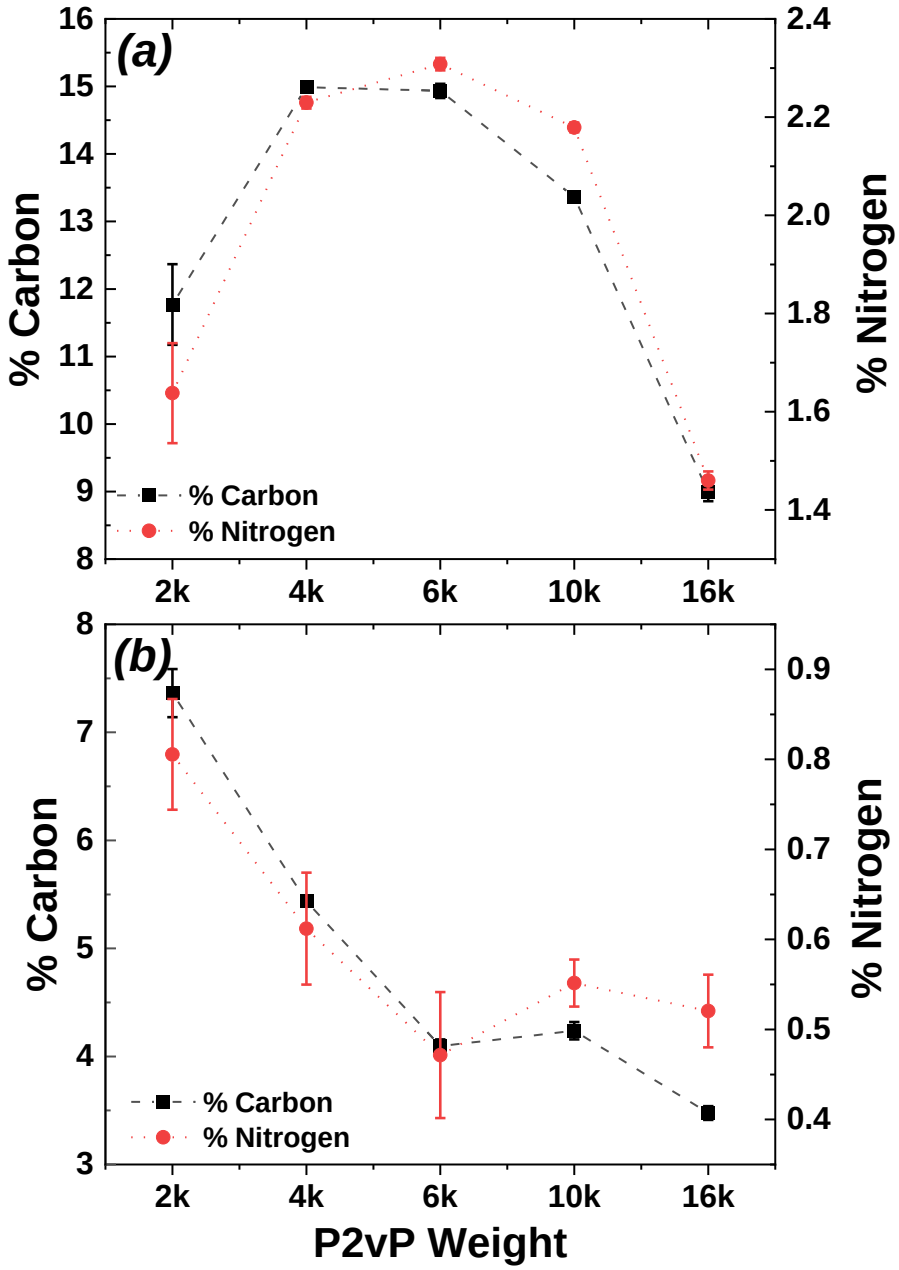


**Figure 4.4:** **Elemental analysis plots of polymer weight grafted to mesoporous silicas SBA-15 (a) and MCM-41 (b). Plots show percentage carbon and nitrogen against the difference in polymer P2vP weight grafted to both mesoporous silicas. Data points represent three repeats.**

Interestingly, the trend seen for both percentage carbon and nitrogen for SBA-15 is completely different for MCM-41. The MCM-41 result is seen in figure 4.4(b). The percentage carbon and nitrogen determined for MCM-41 showed the highest values for the 2k P2vP. The results were

7.36 % for carbon and 0.81 % for nitrogen. There was a dramatic decrease in percentage carbon and nitrogen as the weight of the polymer increased to where it produced a trough at 6k and above. This would indicate that the larger polymer weights are unable to enter into the pores of the mesoporous silica supports. With MCM-41 having smaller pores (26 Å) than SBA-15 (48 Å) the results would agree and explain the low percentage carbon and nitrogen numbers.

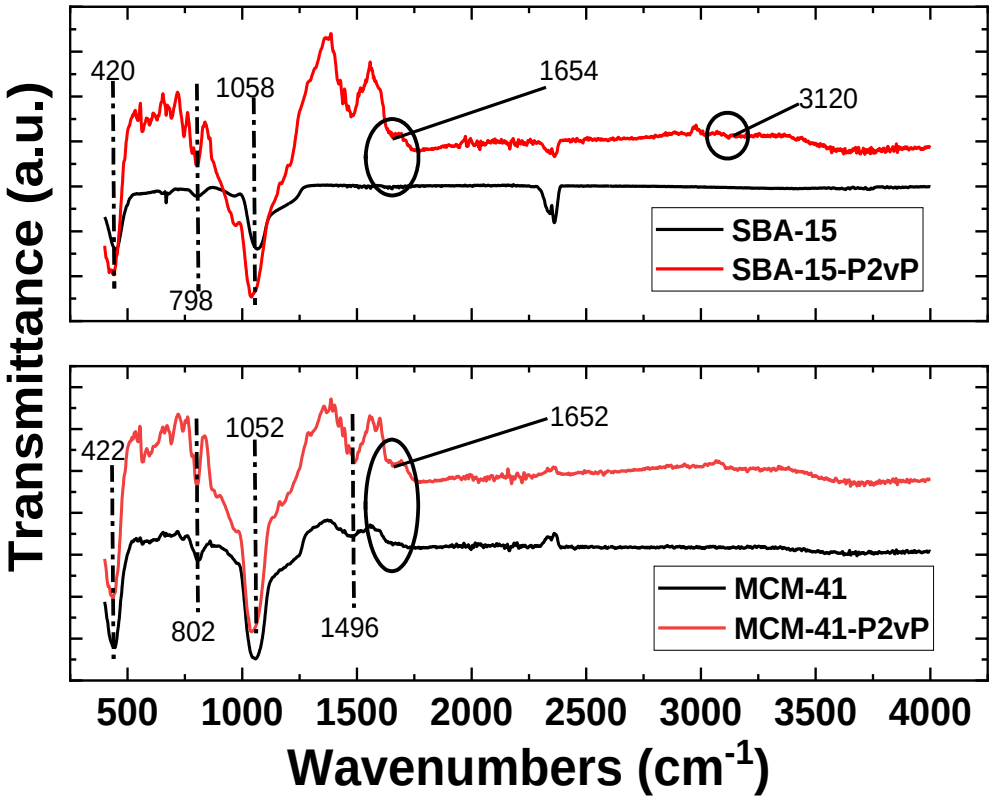


**Figure 4.5: FT-IR spectra of SBA-15 and MCM-41 along with their corresponding spectra after P2vP attachment.**

Fourier-transform infrared spectroscopy (FT-IR) was used to show the grafting of P2vP had occurred on both mesoporous silica supports. Figure 4.5 shows two spectra, SBA-15 (top) and MCM-41 (bottom). In both plots the bare silica material is shown by the black line and the P2vP grafted materials is displayed with the red lines. Typical spectra for mesoporous silicas are

observed for both SBA-15 and MCM-41. The $SiO_2$ framework symmetric and anti-symmetrical vibrations were seen at 798 and 1058 $cm^{-1}$ for SBA-15 and at 800 and 1052 $cm^{-1}$ for MCM-41.

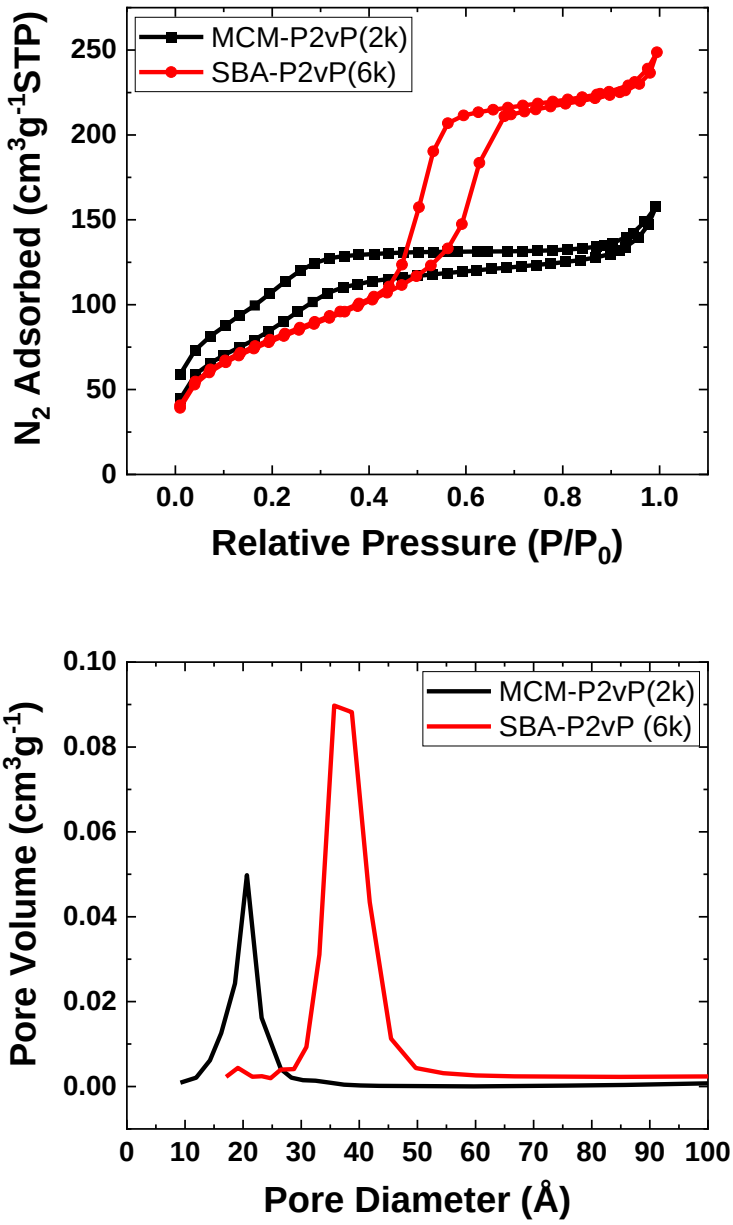


**Figure 4.6:** **Nitrogen adsorption-desorption isotherms (TOP) of P2vP functionalised mesoporous silicas SBA-15 (red) & MCM-41 (black) and the pore size distribution (BOTTOM) of both mesoporous silicas.**

The torsion vibrations of the Si-O-Si framework is also seen at 420 and 422 $cm^{-1}$ for SBA-15 and MCM-41, respectively[62]. The stretching modes related to the nitrogen of the pyridine ring is present at 1654 and 1652 $cm^{-1}$ for SBA-15 and MCM-41[63].

The physical properties were calculated and measured using $N_2$ sorption analysis. The results are seen in table 4.2. With the original surface areas of MCM-41 and SBA-15 at 1005 and 611 $m^2g^{-1}$, respectively, there was a significant drop in surface area after P2vP attachment.

**Table 4.2: Physical properties of P2vP functionalised mesoporous silicas, MCM-41, and SBA-15.**

| **Sample** | **Molecular weight** *k* | **Surface Area** *m2/g* | **Pore Volume** *cm3/g* | **Pore Diameter** *Å* |
|---|---|---|---|---|
| MCM-41 | 2 | 714 | 0.35 | 26 |
| | 4 | 638 | 0.31 | 26 |
| | 6 | 674 | 0.33 | 26 |
| | 10 | 849 | 0.43 | 25 |
| | 16 | 922 | 0.44 | 25 |
| SBA-15 | 2 | 344 | 0.43 | 46 |
| | 4 | 290 | 0.38 | 45 |
| | 6 | 283 | 0.35 | 40 |
| | 10 | 265 | 0.33 | 42 |
| | 16 | 280 | 0.35 | 42 |

Taking MCM-41, two things are happening. The lower molecular weight polymers are grafting to the support on the surface and inside the pores. This is reducing the pore volume significantly. The opposite is occurring with the higher molecular weights of the polymer. Grafting is taking place, but it seems only on the outer surface and not inside the pore structure. This is causing the surface area to decrease more at the lower polymer weights where it begins to increase after the 4-k polymer. A similar trend is seen with SBA-15 silica support but is less pronounced and begins to increase at higher weights (10 k). The pore diameter for both materials seems to stay very

constant and does not change drastically in relative to any of the different polymer weights. A comparison of the two isotherms and the pore diameter of both P2vP functionalised materials is seen in figure 4.6. The regular pore structure of both materials is maintained in the isotherms along with showing the higher slope of the adsorption plot for MCM-41 indicating the higher surface area. The two pore diameter plots show the narrow pore size distribution of both materials along with SBA-15 having the bigger pore size as already outlined.

### *4.4.3 Metal infiltration of silicas*

Cerium metal adsorption was examined in mesoporous silica which had been derivatised with P2vP. As the grafting to MCM-41 was significantly lower when compared with SBA-15, it was decided to infiltrate using only grafted SBA-15 (SBA-P2vP) as its interaction potential was much higher. As a control to these trials, silicas which were not grafted with polymer were also examined.

#### 4.4.3.1 Electron microscopy

Electron microscopy was carried out on mesoporous silica SBA-15 which was grafted with P2vP and incorporated with cerium. SEM showed no difference to unchanged SBA-15 in terms of morphology and size. TEM also showed no difference after incorporation but again shows the hexagonal pore structure and parallel pore channels of SBA-15 with CeO2 as seen in figure 4.7 (a) and (b) respectively.

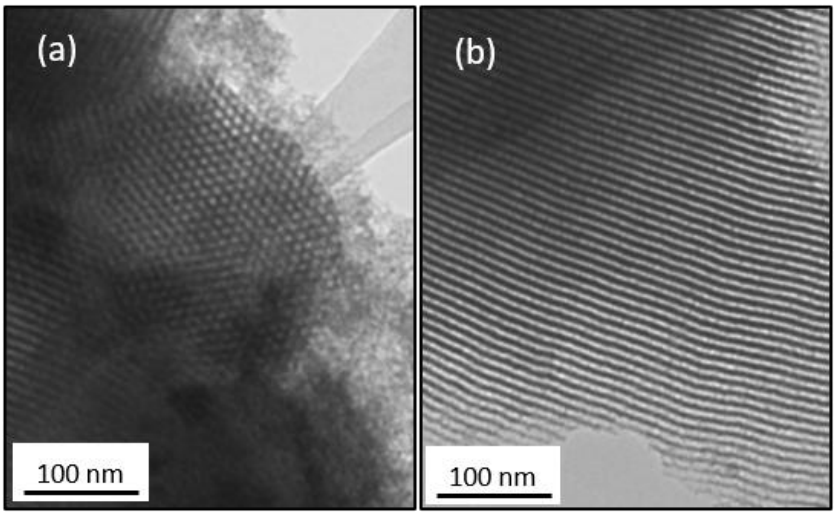


**Figure 4.7: TEM images of SBA-15 with $CeO_2$ infiltrated into P2vP polymer layer; (a) shows the hexagonal pore arrangement with (b) showing the parallel pores produced during silica formation.**

### 4.4.3.2 XPS

XPS was used to determine the elemental surface composition and chemical states of the mesoporous silica. Firstly, XPS showed qualitatively the presence of cerium at the surface of samples. Cerium was detected on all samples which had been grafted with P2vP. Quantification of cerium adsorbed into the P2vP functionalised mesoporous silica is displayed in table 4.3. The results in the table show that adsorption of cerium from solution occurred.

**Table 4.3: Elemental surface composition using relative percentage determined from XPS data.**

| Sample | Composition (Relative %) | | | | |
|---|---|---|---|---|---|
| | *O1s* | *C1s* | *Si2p* | *Ce3d* | *N1s* |
| SBA-cal | 63.9 | - | 36.1 | - | - |
| SBA-Ce (1.0%) | 36.0 | 45.4 | 18.6 | - | - |
| SBA-Ce (5.0%) | 62.6 | 2.80 | 34.6 | - | - |
| SBA-P2vP | 45.2 | 26.4 | 25.70 | - | 2.7 |
| SBA-P2vP-Ce (0.1%) | 62.5 | 3.2 | 34.0 | 0.2 | - |
| SBA-P2vP-Ce (1.0%) | 62.9 | 1.7 | 35.1 | 0.3 | - |
| SBA-P2vP-Ce (5.0%) | 63.5 | 2.5 | 33.2 | 0.8 | - |
| SBA-P2vP-$CeO_2$ (0.1%) | 60.5 | 0.9 | 38.4 | 0.3 | - |
| SBA-P2vP-$CeO_2$ (1.0%) | 62.2 | - | 37.5 | 0.3 | - |
| SBA-P2vP-$CeO_2$ (5.0%) | 64.4 | 1.7 | 33.3 | 0.5 | - |

The results in table 4.3 show the relative percentage of elements making up the surface of the mesoporous silica pressed disk. As the mesoporous SBA-15 material is functionalised with P2vP and then infiltrated with cerium, it is natural to expect the presence of silicon, oxygen, carbon, nitrogen and finally cerium.

The different silica materials were exposed in solution to difference concentration of cerium in ethanol. Not surprisingly, an increase in concentration of metal is seen from the silica material that is in contact with higher concentration solutions. This increase includes a relative percentage of the surface to contain from 0.2 to 0.8 % of cerium. As a control, unfunctionalized silica material was also exposed the cerium solutions. After each exposure, the materials were filtered and washed. As can be seen from the table, no cerium was determined in the SBA-15 material (SBA-cal) along with SBA-Ce (1.0 %) and SBA-Ce (5.0 %).

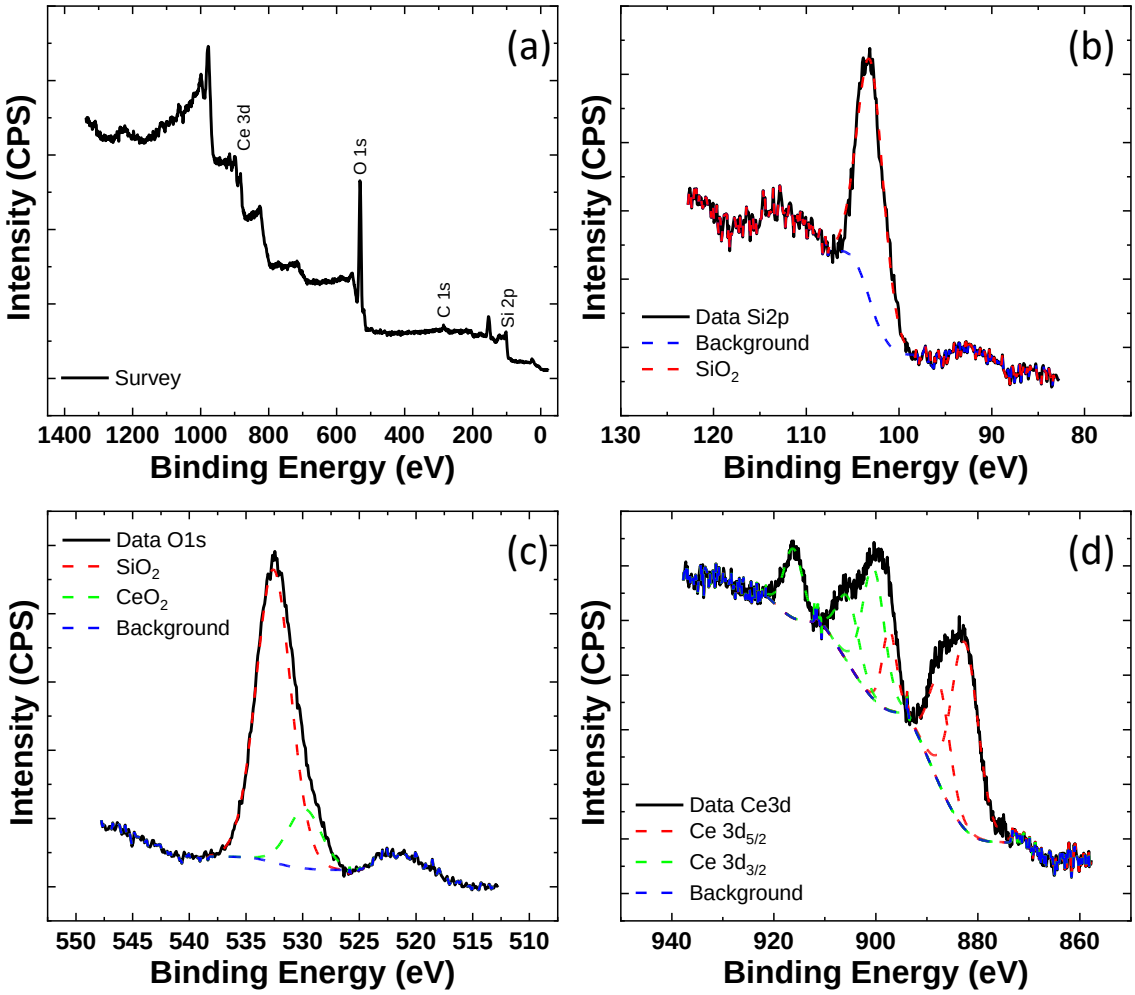


**Figure 4.8:** **XPS spectra for SBA-P2vP-Ce (5.0%) showing survey scan (a), core level scans for silicon (b), oxygen (c) and cerium (d).**

This clearly shows that the interaction for adsorption occurs due to the presence of the P2vP polymer, specifically the pyridine group. It must be stated that as the concentrations of cerium detected in all of the samples is quite low (<1.5%), they are within the limit of detection for accurate figures but can be interpreted as definitely present with error in the precise percentage. Based on the XPS results displayed, the oxidation state of the cerium salt was determined as +4 due to the position of first peak at 880 eV[64].

After incorporating the cerium into the polymer layer, the resulting material was calcined for the removal of the polymer. The percentage cerium decreased after calcination in respect of its related concentration sample. Also, interestingly nitrogen was only determined in the SBA-P2vP sample which also had a very high percentage carbon when compared to the rest of the samples. This was the polymer grafted sample used for infiltration with the cerium salt.

Figure 4.8 shows the survey and core level scans of the material which the highest determination of cerium was achieved. The survey scan shows the presence of silicon, oxygen, carbon, and cerium. High resolution core level scans are also shown of silicon, oxygen, and cerium. The core scan of silicon only shows one elemental species relating to the silica and its presence as $SiO_2$. The oxygen core level scans show the presence of two differing oxygen species. This includes the predominant oxygen relating to silica (532 eV) along with the lower binding energy oxygen seen at 530 eV. This species is due to the presence of the cerium oxide found at the surface. Lastly, the core level scan of the cerium allows the determination of the oxidation state of the cerium present. The shape and build-up of the peak's components, allow for the conclusion that the cerium is in the +4 oxidation state[64]. The position of the first component of the peak seen at 880 eV also proves that the cerium is $CeO_2$ as opposed to $Ce_2O_3$.

#### 4.4.3.3 FT-IR

The adsorption of cerium from solution to silica grafted with P2vP was shown using FT-IR. Figure 4.9 displays the different spectra of silica samples which were infiltrated with cerium from solutions of differing concentrations. Firstly, the spectra show the same peaks which have been discussed previously and displayed in figure 4.5. After infiltration with $CeO_2$, a peak which can only relate to the adsorption of Ce, is seen at 1306 $cm^{-1}$. This is related to wavenumbers seen by Mesaros et al[65]. This strong band seen at approximately 1300 $cm^{-1}$ was also described by Yang et al to be due to $CeO_2$[66]. It is seen that this peak is absent for the SBA-P2vP standard sample. It is also absent from the control samples displayed in figure 4A.3. There is a slight presence of the peak beginning to form for the low concentration solutions associated with Ce (0.1%) samples. As the concentration of the salt solution increases so too is there a correlation between the intensity of this $CeO_2$ peak. Finally, there is an obvious peak for the presence of $CeO_2$ in the highest cerium concentration studied at 5.0 % w/w solutions. Figure 4A.2 represents a highlighted version of figure 4.9, showing detailed viewing of the related peak. It must be also noted that some materials were calcined after infiltration and that these related samples showed a higher intensity for this specific peak at approximately 1306 $cm^{-1}$.

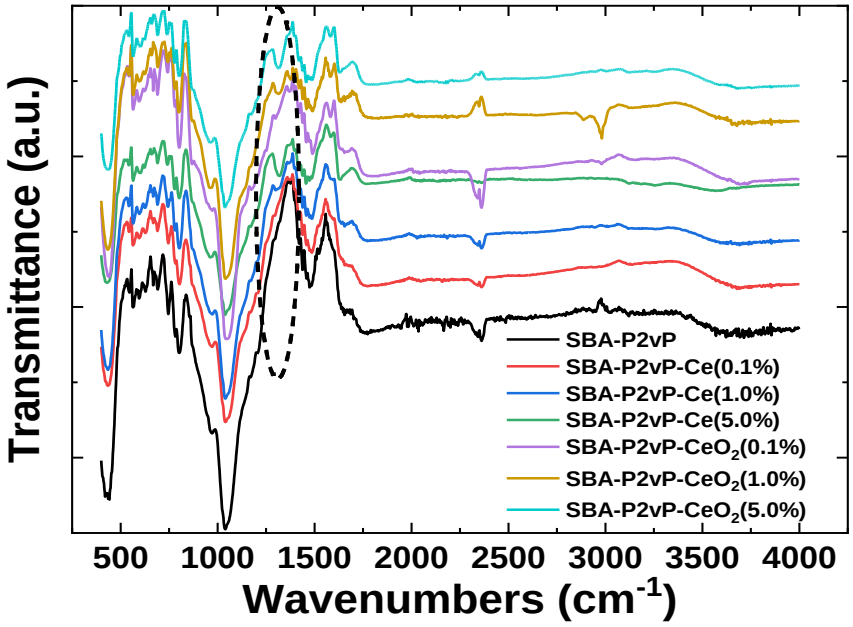


**Figure 4.9:** **FT-IR spectra of multiple SBA materials functionalised with P2vP including the infiltration of cerium metal from solutions of varying metal concentrations. Some materials (titled $CeO_2$) had been calcined.**

### 4.4.3.4 Elemental analysis

Elemental analysis was used to determine if the removal of the polymer occurred after uv/ozone and calcination. If any substantial percentage carbon was determined it was agreed that removal of the polymer failed. It was noticed that $UV/O_3$ did not remove fully the grafted polymer layer. Carbon percentages between 5-8 % were seen from this method of material cleaning. It is thought that the method is only removing the P2vP from silica which forms the top layer of silica placed inside the chamber. The silica buried at the bottom of the pile will undergo less 'cleaning' compared with the material which forms the outer layers. This is potentially the reason as to why some of the polymer is removed and not all. When calcined, the percentage carbon becomes negligible with a value approximately zero. This shows that the polymer is removed leaving behind the silica material which incorporates the metal which was infiltrated into the polymer.

XPS also shows that after calcination the oxidation state of the metal does not change. The cerium oxide stays in +4 oxidation state seen by the position of the cerium core scan at 882 eV[64].

## 4.5 Conclusion

Two types of common mesoporous silicas, SBA-15 and MCM-41 have been synthesised and characterised. Both mesoporous materials were grafted with hydroxy-terminated poly-2-vinyl pyridine. The two mesoporous silicas were synthesised and characterised and the resulting materials were produced as expected. The optimal functionalisation conditions for both mesoporous silicas with P2vP was determined. Higher loading of P2vP to SBA-15 was achieved. The optimal polymer weight determined was between 4-6 k. For mesoporous MCM-41 silica this optimal weight was much lower. It was determined that 2 k was best. The reason for these wide difference in polymer sizes is due to the higher pore sizes available with SBA-15 compared to MCM-41. This is typical of the two materials and is shown due to the physical properties especially pore size or diameter. The values obtained for SBA-15 were a surface area of 611 $m^2g^{-1}$ and pore diameter of 48 Å. This was compared to MCM-41 whose pore diameter was 26 Å with a surface area of 1005 $m^2g^{-1}$. The adsorption of cerium from solutions with varying concentrations was also examined. SBA-15 which had been grafted with P2vP, adsorbed cerium from solution compared with un-functionalised SBA-15 in which no cerium was measured using both XPS and FT-IR. An approximate relative concentration of 0.5-0.8 % of cerium was determined at the surface of the functionalised mesoporous silica pressed disk. Finally, samples were calcined to potentially remove any polymer while also to see if any there was a change in the oxidation state of the cerium. The polymer was removed by calcination by measuring percentage carbon using elemental analysis. The cerium remained in the $CeO_2$ state (+4) as determined by XPS.

## 4.6 References

[1] A.J. Crisci, M.H. Tucker, M. Lee, S.G. Jang, J.A. Dumesic, S.L. Scott, Acid-Functionalized SBA-15-Type Silica Catalysts for Carbohydrate Dehydration, ACS Catal. 1 (2011) 719–728. https://doi.org/10.1021/cs2001237.

[2] K.K. Sharma, A. Anan, R.P. Buckley, W. Ouellette, T. Asefa, Toward efficient nanoporous catalysts: Controlling site-isolation and concentration of grafted catalytic sites on nanoporous materials with solvents and colorimetric elucidation of their site-isolation, J. Am. Chem. Soc. 130 (2008) 218–228. https://doi.org/10.1021/ja074128t.

[3] I. Agirrezabal-Telleria, J. Requies, M.B. Güemez, P.L. Arias, Pore size tuning of functionalized SBA-15 catalysts for the selective production of furfural from xylose, Appl. Catal. B Environ. 115–116 (2012) 169–178. https://doi.org/10.1016/j.apcatb.2011.12.025.

[4] J. Zhang, J. Zhuang, L. Lin, S. Liu, Z. Zhang, Conversion of D-xylose into furfural with mesoporous molecular sieve MCM-41 as catalyst and butanol as the extraction phase, Biomass and Bioenergy. 39 (2012) 73–77. https://doi.org/10.1016/j.biombioe.2010.07.028.

[5] Y. Zhang, J. Zhang, T. Jiang, S. Wang, Inclusion of the poorly water-soluble drug simvastatin in mesocellular foam nanoparticles: Drug loading and release properties, Int. J. Pharm. 410 (2011) 118–124. https://doi.org/10.1016/j.ijpharm.2010.07.040.

[6] I.I. Slowing, J.L. Vivero-Escoto, C.W. Wu, V.S.Y. Lin, Mesoporous silica nanoparticles as controlled release drug delivery and gene transfection carriers, Adv. Drug Deliv. Rev. 60 (2008) 1278–1288. https://doi.org/10.1016/j.addr.2008.03.012.

[7] S.K. Natarajan, S. Selvaraj, Mesoporous silica nanoparticles: Importance of surface

modifications and its role in drug delivery, RSC Adv. 4 (2014) 14328–14334. https://doi.org/10.1039/c4ra00781f.

[8] F. Sevimli, A. Yilmaz, Surface functionalization of SBA-15 particles for amoxicillin delivery, Microporous Mesoporous Mater. 158 (2012) 281–291. https://doi.org/10.1016/j.micromeso.2012.02.037.

[9] K.C.-W. Wu, Y. Yamauchi, C.-Y. Hong, Y.-H. Yang, Y.-H. Liang, T. Funatsu, T. Makoto, Biocompatible, surface functionalized mesoporous titania nanoparticles for intracellular imaging and anticancer drug delivery, Chem. Commun. (2011) 5232–5234.

[10] T. Gong, Y. Li, H. Zhang, J. Zhou, G. Xie, B. Lei, J. Zhuang, Y. Liu, H. Zhang, Synthesis of SBA-15 with different morphologies for oxygen sensing, Microporous Mesoporous Mater. (2020) 110001. https://doi.org/10.1016/j.micromeso.2020.110001.

[11] M. Hasanzadeh, N. Shadjou, M. Eskandani, M. de la Guardia, Mesoporous silica-based materials for use in electrochemical enzyme nanobiosensors, TrAC - Trends Anal. Chem. 40 (2012) 106–118. https://doi.org/10.1016/j.trac.2012.06.007.

[12] S. Dehdashtian, M.B. Gholivand, M. Shamsipur, Z. Karimi, A nano sized functionalized mesoporous silica modified carbon paste electrode as a novel, simple, robust and selective anti-diabetic metformin sensor, Sensors Actuators B Chem. 221 (2015) 807–815. https://doi.org/10.1016/j.snb.2015.07.010.

[13] S.K. Vashist, E. Lam, S. Hrapovic, K.B. Male, J.H.T. Luong, Immobilization of antibodies and enzymes on 3-aminopropyltriethoxysilane-functionalized bioanalytical platforms for biosensors and diagnostics, Chem. Rev. 114 (2014) 11083–11130. https://doi.org/10.1021/cr5000943.

[14] A. Katiyar, S. Yadav, P.G. Smirniotis, N.G. Pinto, Synthesis of ordered large pore SBA-15 spherical particles for adsorption of biomolecules, J. Chromatogr. A. 1122 (2006) 13–20. https://doi.org/10.1016/j.chroma.2006.04.055.

[15] A.M. Burke, J.P. Hanrahan, D.A. Healy, J.R. Sodeau, J.D. Holmes, M.A. Morris, Large pore bi-functionalised mesoporous silica for metal ion pollution treatment, J. Hazard. Mater. 164 (2009) 229–234. https://doi.org/10.1016/j.jhazmat.2008.07.146.

[16] A.L.T. Pham, D.L. Sedlak, F.M. Doyle, Dissolution of mesoporous silica supports in aqueous solutions: Implications for mesoporous silica-based water treatment processes, Appl. Catal. B Environ. 126 (2012) 258–264. https://doi.org/10.1016/j.apcatb.2012.07.018.

[17] A. Rimola, D. Costa, M. Sodupe, J.F. Lambert, P. Ugliengo, Silica surface features and their role in the adsorption of biomolecules: Computational modeling and experiments, Chem. Rev. 113 (2013) 4216–4313. https://doi.org/10.1021/cr3003054.

[18] R. Kishor, A.K. Ghoshal, Amine-Modified Mesoporous Silica for CO2 Adsorption: The Role of Structural Parameters, Ind. Eng. Chem. Res. 56 (2017) 6078–6087. https://doi.org/10.1021/acs.iecr.7b00890.

[19] S.M.L. Dos Santos, K.A.B. Nogueira, M. De Souza Gama, J.D.F. Lima, I.J. Da Silva Júnior, D.C.S. De Azevedo, Synthesis and characterization of ordered mesoporous silica (SBA-15 and SBA-16) for adsorption of biomolecules, Microporous Mesoporous Mater. 180 (2013) 284–292. https://doi.org/10.1016/j.micromeso.2013.06.043.

[20] E. Da'na, Adsorption of heavy metals on functionalized-mesoporous silica: A review, Microporous Mesoporous Mater. 247 (2017) 145–157.

https://doi.org/10.1016/j.micromeso.2017.03.050.

[21] H. Chaudhuri, S. Dash, A. Sarkar, SBA-15 functionalised with high loading of amino or carboxylate groups as selective adsorbent for enhanced removal of toxic dyes from aqueous solution, New J. Chem. 40 (2016) 3622–3634. https://doi.org/10.1039/c5nj02816g.

[22] P.K. Jal, S. Patel, B.K. Mishra, Chemical modification of silica surface by immobilization of functional groups for extractive concentration of metal ions, Talanta. 62 (2004) 1005–1028. https://doi.org/10.1016/j.talanta.2003.10.028.

[23] A. Stein, Advances in microporous and mesoporous solids - Highlights of recent progress, Adv. Mater. 15 (2003) 763–775. https://doi.org/10.1002/adma.200300007.

[24] H. Yoshitake, T. Yokoi, T. Tatsumi, Adsorption of chromate and arsenate by amino-functionalized MCM-41 and SBA-1, Chem. Mater. 14 (2002) 4603–4610. https://doi.org/10.1021/cm0202355.

[25] S. Mintova, J. Čejka, Micro/Mesoporous Composites, in: J. Čejka, H. van Bekkum, A. Corma, F.B.T.-S. in S.S. and C. Schüth (Eds.), Introd. to Zeolite Sci. Pract., Elsevier, 2007: pp. 301–VI. https://doi.org/https://doi.org/10.1016/S0167-2991(07)80797-X.

[26] H.-C. Zhou, S. Kitagawa, Metal–Organic Frameworks (MOFs), Chem. Soc. Rev. 43 (2014) 5415–5418. https://doi.org/10.1039/C4CS90059F.

[27] N.A. Khan, Z. Hasan, S.H. Jhung, Adsorptive removal of hazardous materials using metal-organic frameworks (MOFs): A review, J. Hazard. Mater. 244–245 (2013) 444–456. https://doi.org/10.1016/j.jhazmat.2012.11.011.

[28] Y. Yin, Z.-F. Yang, Z.-H. Wen, A.-H. Yuan, X.-Q. Liu, Z.-Z. Zhang, H. Zhou,

Modification of as Synthesized SBA-15 with Pt nanoparticles: Nanoconfinement Effects Give a Boost for Hydrogen Storage at Room Temperature, Sci. Rep. 7 (2017) 4509. https://doi.org/10.1038/s41598-017-04346-9.

[29] J.S. Beck, J.C. Vartuli, W.J. Roth, M.E. Leonowicz, C.T. Kresge, K.D. Schmitt, C.T.-W. Chu, D.H. Olson, E.W. Sheppard, S.B. McCullen, J.B. Higgins, J.L. Schlenkert, A New Family of Mesoporous Molecular Sieves Prepared with Liquid Crystal Templates, J. Am. Chem. Soc. (1992) 10834–10843.

[30] H. Ritter, D. Brühwiler, Accessibility of amino groups in postsynthetically modified mesoporous silica, J. Phys. Chem. C. 113 (2009) 10667–10674. https://doi.org/10.1021/jp901983j.

[31] D. Kumar, K. Schumacher, C. Du Fresne von Hohenesche, M. Grün, K.K. Unger, MCM-41, MCM-48 and related mesoporous adsorbents: their synthesis and characterisation, Colloids Surfaces A Physicochem. Eng. Asp. 187–188 (2001) 109–116. https://doi.org/10.1016/S0927-7757(01)00638-0.

[32] D. Zhao, J. Feng, Q. Huo, N. Melosh, H. Glenn, B.F. Chmelka, G.D. Stucky, G.H. Fredrickson, F. Chmelka, Triblock Copolymer Syntheses of Mesoporous 50 to 300 Angstrom Silica with Periodic Pores, Science (80-. ). 279 (1998) 548–552.

[33] D. Zhao, Q. Huo, J. Feng, B.F. Chmelka, G.D. Stucky, Tri-, Tetra-, and Octablock Copolymer and Nonionic Surfactant Syntheses of Highly Ordered, Hydrothermally Stable, Mesoporous Silica Structures, J. Am. Chem. Soc. 120 (1998) 6024–6036.

[34] Y. Li, W. Xiong, C. Wang, B. Song, G. Zhang, Synthesis of hexagonal mesoporous silicates functionalized with amino groups in the pore channels by a co-condensation

approach, RSC Adv. 6 (2016) 53991–54000. https://doi.org/10.1039/c5ra24597d.

[35] F. Xie, Z. Xie, P. Liu, Y. Yuan, J. Li, S. Chen, F. Guo, J. Chen, Z. Gu, A highly organic functionalized three-connected periodic mesoporous silica by Co-condensation with hydridosilica, Microporous Mesoporous Mater. 266 (2018) 177–182. https://doi.org/10.1016/j.micromeso.2018.03.001.

[36] E. Da'na, A. Sayari, Adsorption of copper on amine-functionalized SBA-15 prepared by co-condensation: Equilibrium properties, Chem. Eng. J. 166 (2011) 445–453. https://doi.org/10.1016/j.cej.2010.11.016.

[37] A. Szegedi, M. Popova, I. Goshev, J. Mihály, Effect of amine functionalization of spherical MCM-41 and SBA-15 on controlled drug release, J. Solid State Chem. 184 (2011) 1201–1207. https://doi.org/10.1016/j.jssc.2011.03.005.

[38] H. Salmio, D. Brühwiler, Distribution of amino groups on a mesoporous silica surface after submonolayer deposition of aminopropylsilanes from an anhydrous liquid phase, J. Phys. Chem. C. 111 (2007) 923–929. https://doi.org/10.1021/jp0651440.

[39] F. Ilhan, E.F. Fabrizio, L. McCorkle, D.A. Scheiman, A. Dass, A. Palczer, M.B. Meador, J.C. Johnston, N. Leventis, Hydrophobic monolithic aerogels by nanocasting polystyrene on amine-modified silica, J. Mater. Chem. 16 (2006) 3046. https://doi.org/10.1039/b604323b.

[40] V.D. Hoang, T.P. Dang, Q.K. Dinh, H.P. Nguyen, A.T. Vu, The synthesis of novel hybrid thiol-functionalized nano-structured SBA-15, Adv. Nat. Sci. Nanosci. Nanotechnol. 1 (2010). https://doi.org/10.1088/2043-6262/1/3/035011.

[41] S.J.L. Billinge, E.J. McKimmy, M. Shatnawi, H.J. Kim, V. Petkov, D. Wermeille, T.J.

Pinnavaia, Mercury binding sites in thiol-functionalized mesostructured silica, J. Am. Chem. Soc. 127 (2005) 8492–8498. https://doi.org/10.1021/ja0506859.

[42] P. Innocenzi, G. Brusatin, M. Guglielmi, R. Bertani, New synthetic route to (3-glycidoxypropyl)trimethoxysilane-based hybrid organic-inorganic materials, Chem. Mater. 11 (1999) 1672–1679. https://doi.org/10.1021/cm980734z.

[43] R. Rajan, E. Rainosalo, S.P. Thomas, S.K. Ramamoorthy, J. Zavašnik, J. Vuorinen, M. Skrifvars, Modification of epoxy resin by silane-coupling agent to improve tensile properties of viscose fabric composites, Polym. Bull. 75 (2018) 167–195. https://doi.org/10.1007/s00289-017-2022-2.

[44] J. Nawrocki, The silanol group and its role in liquid chromatography, J. Chromatogr. A. 779 (1997) 29–71. https://doi.org/10.1016/S0021-9673(97)00479-2.

[45] B. Buszewski, L. Nondek, A. Jurášek, D. Berek, Preparation of silanized silica with high ligand density. The effect of silane structure, Chromatographia. 23 (1987) 442–446. https://doi.org/10.1007/BF02311822.

[46] E. Vilarrasa-García, J.A. Cecilia, S.M.L. Santos, C.L. Cavalcante, J. Jiménez-Jiménez, D.C.S. Azevedo, E. Rodríguez-Castellón, CO2 adsorption on APTES functionalized mesocellular foams obtained from mesoporous silicas, Microporous Mesoporous Mater. 187 (2014) 125–134. https://doi.org/10.1016/j.micromeso.2013.12.023.

[47] D.W. Lee, B.R. Yoo, Advanced silica/polymer composites: Materials and applications, J. Ind. Eng. Chem. 38 (2016) 1–12. https://doi.org/10.1016/j.jiec.2016.04.016.

[48] L. Marcoux, J. Florek, R. Guillet-Nicolas, F. Kleitz, Mesoporous polymer-silica nanocomposites with stimuli responsive functional groups, Microporous Mesoporous

Mater. 291 (2020) 109690. https://doi.org/10.1016/j.micromeso.2019.109690.

[49] M. Chen, L. Qin, Y. Liu, F. Zhang, Controllable preparation of polymer brushes from mesoporous silica SBA-15 via surface-initiated ARGET ATRP, Microporous Mesoporous Mater. 263 (2018) 158–164. https://doi.org/10.1016/j.micromeso.2017.12.019.

[50] R. Liu, P. Liao, J. Liu, P. Feng, Responsive polymer-coated mesoporous silica as a pH-sensitive nanocarrier for controlled release, Langmuir. 27 (2011) 3095–3099. https://doi.org/10.1021/la104973j.

[51] C. Cummins, M.A. Morris, Using block copolymers as infiltration sites for development of future nanoelectronic devices: Achievements, barriers, and opportunities, Microelectron. Eng. 195 (2018) 74–85. https://doi.org/10.1016/j.mee.2018.04.005.

[52] C. Cummins, M.T. Shaw, M.A. Morris, Area Selective Polymer Brush Deposition, Macromol. Rapid Commun. 38 (2017) 1–6. https://doi.org/10.1002/marc.201700252.

[53] M. Thommes, R. Köhn, M. Fröba, Sorption and pore condensation behavior of pure fluids in mesoporous MCM-48 silica, MCM-41 silica, SBA-15 silica and controlled-pore glass at temperatures above and below the bulk triple point, Appl. Surf. Sci. 196 (2002) 239–249. https://doi.org/10.1016/S0169-4332(02)00062-4.

[54] A.T. Krzyzak, I. Habina, Low field1H NMR characterization of mesoporous silica MCM-41 and SBA-15 filled with different amount of water, Microporous Mesoporous Mater. 231 (2016) 230–239. https://doi.org/10.1016/j.micromeso.2016.05.032.

[55] Z.A. Alothman, A review: Fundamental aspects of silicate mesoporous materials, Materials (Basel). 5 (2012) 2874–2902. https://doi.org/10.3390/ma5122874.

[56] M. Kruk, M. Jaroniec, J.M. Kim, R. Ryoo, Characterization of highly ordered MCM-41 silicas using X-ray diffraction and nitrogen adsorption, Langmuir. 15 (1999) 5279–5284. https://doi.org/10.1021/la990179v.

[57] X. Wang, Q. Guo, T. Kong, Tetraethylenepentamine-modified MCM-41/silica gel with hierarchical mesoporous structure for CO2 capture, Chem. Eng. J. 273 (2015) 472–480. https://doi.org/10.1016/j.cej.2015.03.098.

[58] V. Hernández-Morales, R. Nava, Y.J. Acosta-Silva, S.A. MacÍas-Sánchez, J.J. Pérez-Bueno, B. Pawelec, Adsorption of lead (II) on SBA-15 mesoporous molecular sieve functionalized with -NH2 groups, Microporous Mesoporous Mater. 160 (2012) 133–142. https://doi.org/10.1016/j.micromeso.2012.05.004.

[59] R. Lundy, P. Yadav, N. Prochukhan, E.C. Giraud, T.F. O'Mahony, A. Selkirk, E. Mullen, J. Conway, M. Turner, S. Daniels, P.G. Mani-Gonzalez, M. Snelgrove, J. Bogan, C. McFeely, R. O'Connor, E. McGlynn, G. Hughes, C. Cummins, M.A. Morris, Precise Definition of a "monolayer Point" in Polymer Brush Films for Fabricating Highly Coherent TiO2Thin Films by Vapor-Phase Infiltration, Langmuir. 36 (2020) 12394–12402. https://doi.org/10.1021/acs.langmuir.0c02512.

[60] T. Sierański, Discovering the stacking landscape of a pyridine-pyridine system, J. Mol. Model. 23 (2017). https://doi.org/10.1007/s00894-017-3496-4.

[61] R. Lundy, P. Yadav, A. Selkirk, E. Mullen, T. Ghoshal, C. Cummins, M.A. Morris, R. Lundy, P. Yadav, A. Selkirk, E. Mullen, T. Ghoshal, C. Cummins, Optimizing polymer brush coverage to develop highly coherent sub-5nm oxide films by ion inclusion Optimizing polymer brush coverage to develop highly coherent sub- 5nm oxide films by ion inclusion, Chem. Mater. (2019). https://doi.org/10.1021/acs.chemmater.9b02856.

[62] I.A. Rahman, M. Jafarzadeh, C.S. Sipaut, Synthesis of organo-functionalized nanosilica via a co-condensation modification using (gamma)-aminopropyltriethoxysilane (APTES), Ceram. Int. 35 (2009) 1883–1888. https://doi.org/10.1016/j.ceramint.2008.10.028.

[63] M. Snelgrove, C. Zehe, R. Lundy, P. Yadav, J.-P. Rueff, R. O'Connor, J. Bogan, G. Hughes, E. McGlynn, M. Morris, P.G. Mani-Gonzalez, Surface characterization of poly-2-vinylpyridine—A polymer for area selective deposition techniques, J. Vac. Sci. Technol. A. 37 (2019) 050601. https://doi.org/10.1116/1.5115769.

[64] E. Beche, P. Charvin, D. Perarnau, S. Abanades, G. Flamant, Ce3d XPS investigation of cerium oxides and mixed cerium oxide (CexTiyOz), Surf. Interface Anal. (2008) 264–267. https://doi.org/10.1002/sia.2686.

[65] O.L. Pop, Z. Diaconeasa, A. Mesaroş, D.C. Vodnar, L. Cuibus, L. Ciontea, C. Socaciu, FT-IR Studies of Cerium Oxide Nanoparticles and Natural Zeolite Materials, Bull. Univ. Agric. Sci. Vet. Med. Cluj-Napoca. Food Sci. Technol. 72 (2015). https://doi.org/10.15835/buasvmcn-fst:11030.

[66] G. Qi, R.T. Yang, Characterization and FTIR studies of MnO x-CeO 2 catalyst for low-temperature selective catalytic reduction of NO with NH 3, J. Phys. Chem. B. 108 (2004) 15738–15747. https://doi.org/10.1021/jp048431h.

## 4.7 Appendix – Chapter 4

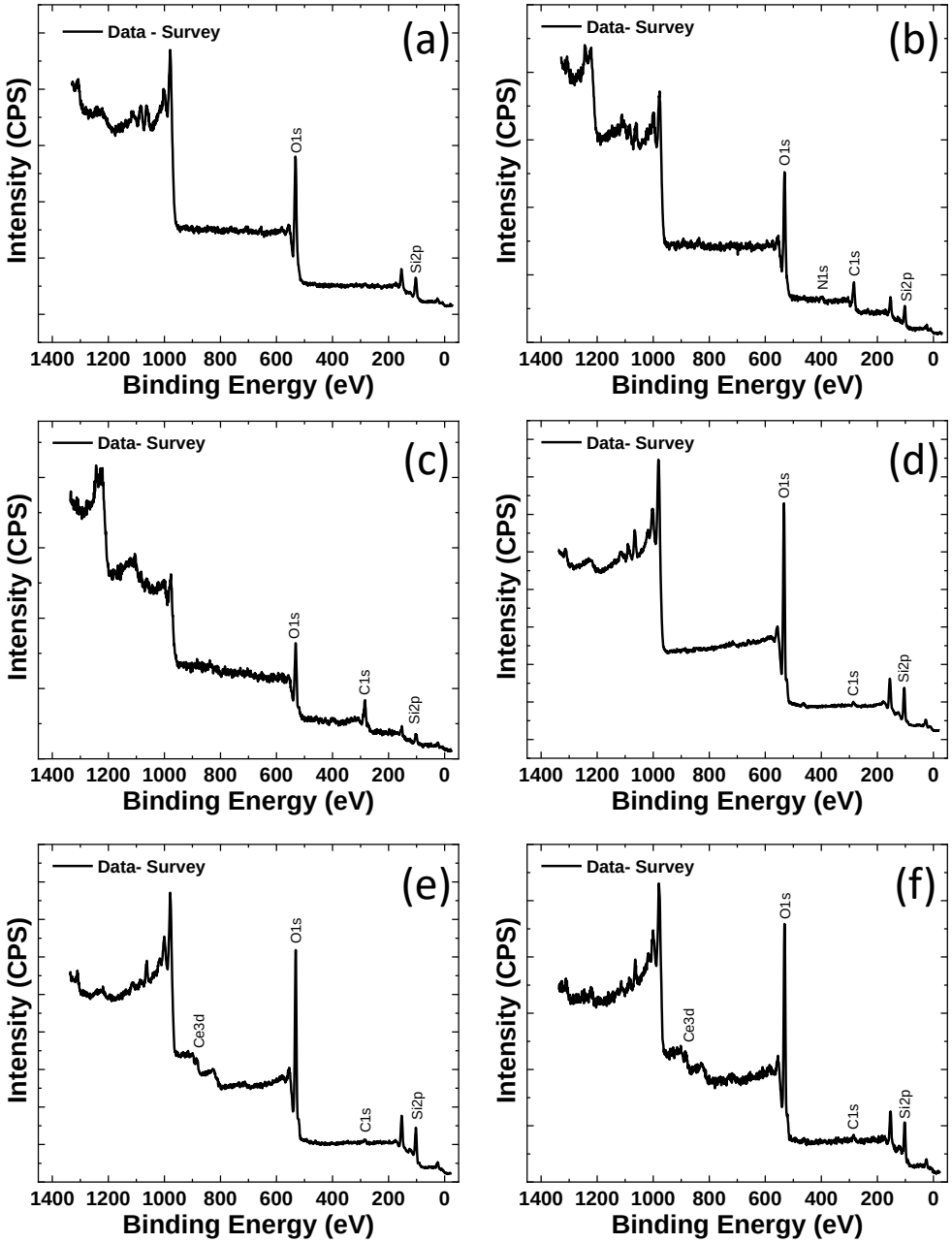


**Figure 4A.1: XPS survey spectra of various mesoporous silica SBA-15 samples including calcined SBA-15 (a), SBA-P2vP (b), SBA-Ce (1.0%) (c),SBA-Ce (5.0%) (d), SBA-P2vP-Ce (0.1%) (e), SBA-P2vP-$CeO_2$ (0.1%) (f).**

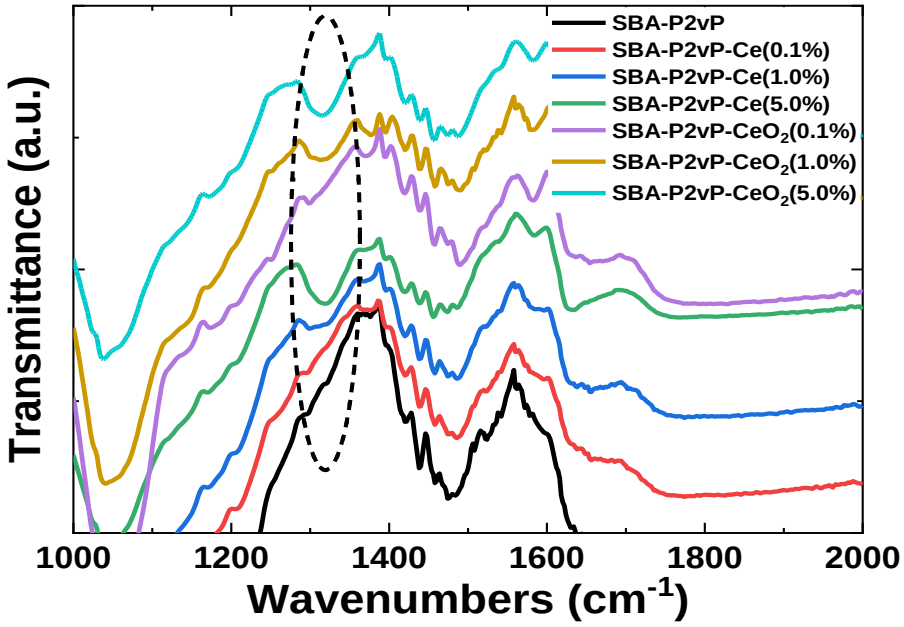


**Figure 4A.2: FT-IR spectra of P2vP functionalised mesoporous silica with specific interest in the peaks seen at 1306 $cm^{-1}$.**

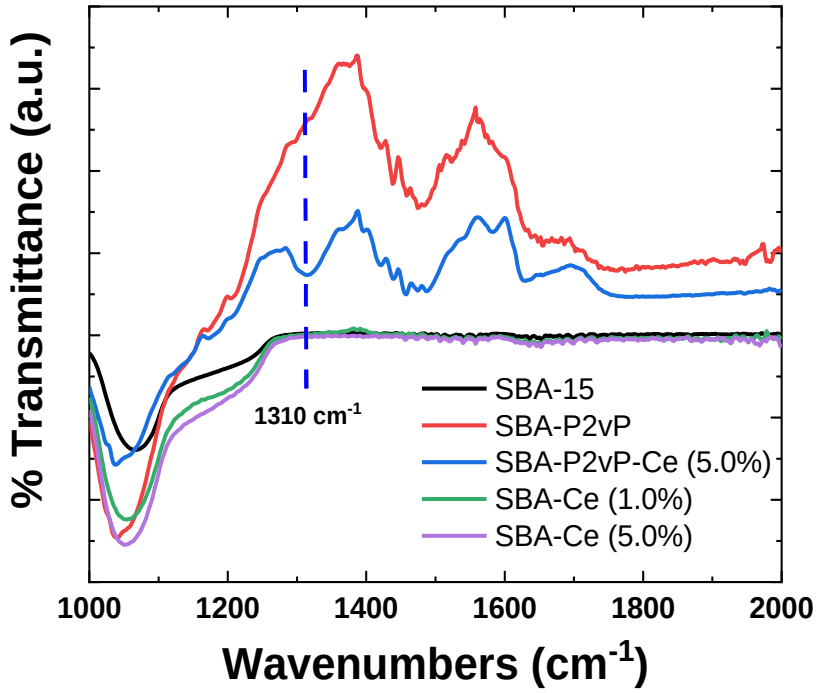


**Figure 4A.3:** **FT-IR spectra showing the difference between the control samples and the P2vP grafted samples which adsorption of the cerium metal was detected.**

# *Chapter 5*

# *Exploring the efficacy of methods that enable the smart delivery of antimicrobial essential oils in food applications: Porous silica particles as carriers*

## 5.1 Abstract

The objective of this study was to develop a simple method for smart delivery of antimicrobial essential oils using a support material with a high surface area that was chemically bound to a substrate. Mesoporous silica (SBA-15) was functionalised *via* a post-synthetic reaction using (3-aminopropyl) triethoxysilane (APTES) and then grafted to a 3-glycidyloxypropyltrimethoxysilane (GPTS) modified surface. The smart delivery device (mesoporous SBA-15) was loaded with antimicrobial oregano essential oil (OEO) and the antimicrobial activity assessed against common food spoilage microorganisms *Escherichia coli*, *Bacillus cereus*, *Staphylococcus aureus* and *Pseudomonas fluorescens*. Results indicate that functionalization of the SBA-15 with APTES resulted in similar antimicrobial activity to SBA-OEO and that SBA-APTES was successfully bound to a GPTS modified surface. However, the integration of the functionalised and loaded carrier materials to a model substrate did not result in significantly higher antimicrobial activity. Nevertheless, given the strong absorption properties of SBA materials, good antimicrobial activity and GRAS nature of SBA-OEO and SBA-APTES-OEO, the results found in this study open potential applications of the functionalised carrier materials *via* a simple "sprinkle" directly on a food product or through the insertion into an edible film and also potentially used as a flavour delivering system.

## 5.2 Introduction

### *5.2.1 Industrial Relevance*

Given the resource intensive nature of growing, producing, processing, and packaging food products, food wastage represent a significant cost not only to the food industry but also to society as a whole. Increasing consumer demand for sustainable, fresh-like, minimally processed, and clean label food products has driven interest in the use of essential oils (EO's) for food preservation. However, applications of EO's on food products is somewhat limited due to the EO's characteristics such as strong hydrophobicity and volatility, which may cause off-flavours and

odours within the packaged product. Therefore, techniques such as incorporation into active edible films, carriers, or encapsulation, could offer controlled release of EO's into the food environment reducing the organoleptic properties while delivering the antimicrobial properties of the EO's more effectively. We developed a simple method for smart delivery of antimicrobial essential oils using a support material (mesoporous SBA-15) with a high surface area that was chemically bound to a substrate. Given the strong antimicrobial activity and GRAS nature of SBA-OEO and SBA-APTES-OEO, this smart delivery system could potentially be applied *via* a simple "sprinkle" directly on a food product, through the insertion into an edible film or potentially used as a flavour delivering system of other EO's.

### *5.2.2 Introduction*

Global food security challenges such as an increasing global population (estimated to reach 9 billion by 2050), increasing rural to urban migration, and climate change are putting increased pressure on global food production and supply chains[1].To alleviate some of these challenges, extensive research has been carried out on the incorporation of natural antimicrobial materials (NAM's), a material derived from a naturally occurring source (i.ie plant, animals etc.), with packaging to help reduce food waste and meet consumer demand for sustainable, fresh-like, minimally processed and clean label food products[1]. One such suitable class of NAM's are essential oils (EO's) which are defined as a product obtained by steam distillation from a natural raw material of plant origin by the ISO (2013). These materials have favourable properties for use in food contact applications such as: good antimicrobial activity, GRAS (Generally Recognised as Safe) status approved by the Food and Drug Administration (FDA), and an acceptability to consumers from their historical use as natural flavourings[2,3]. Compositionally EO's are made up of a combination of secondary metabolites constituents such as terpenes, terpenoids, and phenylpropanoids. These metabolites such as p-cymene, thymol, and eugenol can synergistically contribute to the antimicrobial activity of EO's via interactions with cell walls components[4,5].

Despite EO's good antimicrobial properties, roadblocks in their application exist because of their hydrophobicity, thermolability, photosensitivity, and strong influence on organoleptic properties [1]. These volatile properties mean that EO's are highly susceptible to autoxidation, isomerisation and thermal rearrangements[6–8]. Therefore, to overcome these limitations several strategies to deliver EOs into food systems such as incorporation into sachets and edibles films have been used. However, these approaches also present their own technical issues like an impact on the organoleptic properties of food and limited suitability to certain packaging systems[9]. One potential solution to these roadblocks is the encapsulation of EO's into a porous siliceous material such as: Santa Barbara Amorphous (SBA-15) or Mobil Composition of Matter No. 41 (MCM-41)[10]. These materials can be used to protect EO's from environmental stressors and allow for controlled release of the EO while also facilitating more targeted release of EO onto the food surface, where most of the spoilage occurs[11]. In particular, the use of SBA-15 as an encapsulator is attractive as these materials are currently used in the food sector as catalysts in the synthesis of nutrients, bioactive molecules, sensor technology and as carriers to design smart delivery systems [11]. Moreover, SBA materials have greater mechanical and hydrothermal stability over other siliceous materials such as MCM-41 [12,13], and have adjustable nano-pore size[10], ordered pore structure[14], large specific surface area ($\sim$1000 $m^2$ $g^{-1}$) and relatively large void volume[13] and are also considered GRAS and are an authorised additive in the European Union (E-551) [11].

SBA-15 materials can be readily functionalised with various organic functional containing groups such as 3-aminopropyltriethoxysilane (APTES) which are covalently grafted on the wall of the porous structure *via* hydrolysis and/or condensation reactions resulting in an amine modified porous silica that retains the mesoporous silica's favourable physical properties[15]. Moreover, the amine modified SBA can undergo further reactions with other organo-functional alkoxysilanes such as 3-glycidoxypropyl-trimethoxysilane (GPTS) as the epoxy group on GPTS can readily undergo various reactions such as poly-addition to the amine group or hydrolytic ring opening. In addition, the trialkoxysilyl moiety of GPTS can undergo hydrolysis and condensation reactions

with terminal hydroxyl groups [16]. This method of grafting could be used to attach functionalised SBA to food packaging surfaces and could be suitable for food applications as the reaction between the APTES and GPTS can be carried out in deionised water, and will anchor the SBA support material covalently to a packaging surface[17].

Mesoporous silica supports for EO delivery in food applications have been reported. Park et al found that MCM-41 and SBA-15 loaded with natural antimicrobial allyl isothiocyanate were antimicrobially active against *Escherichia coli*, *Bacillus cereus*, and *Pichia anomola*[18]. Ruiz-Rico et al reported a significant reduction in the concentration of *Listeria innocua* in pasteurized skimmed milk using vanillin grafted onto the surface of MCM-41[19].

However, to the best of our knowledge, no studies were carried out to assess the potential novel strategy of using SBA functionalised with APTES and its covalent attachment to a GPTS modified surface. This would allow a carrier to be fixed to a surface limiting migration of the particles and allowing high density binding and high enough concentrations of OEO to be effective. Therefore, the objectives of this study were to covalently attach SBA functionalised with APTES to GPTS modified surface as a support material for grafting OEO. The synthesised materials were subsequently characterised, and their antimicrobial activity assessed.

## 5.3 Materials and Methods

### *5.3.1 Materials*

Oregano essential oil was purchased from Lionel Hitchens Ltd (Barton Stacey, Hampshire, UK). Mueller-Hinton Broth (MHB), Mueller-Hinton Agar (MHA), and Maximum Recovery Diluent (MRD) were purchased from Oxoid (Basingstoke, UK). *Escherichia coli* (*E. coli*) (NCIMB 11943), *Bacillus cereus* (B. cereus) (NCIMB 9373), *Staphylococcus aureus* (*S. aureus*) (NCIMB 13062) and *Pseudomonas fluorescens* (*P. fluorescens*) (NCIMB 9046) were maintained on Tryptic Soy Agar slants until use at 4 °C. Siliceous SBA-15 mesoporous material was purchased from

Glantreo, Ireland. Blanket Si substrates were purchased from Sil'tronix, France. Sulphuric acid (ACS reagent 95-98%), 3-Aminopropyltriethoxysilane (99%) (APTES), (3-glycidyloxypropyl)trimethoxysilane (>98%) (GPTS), hydrogen peroxide solution (30%), 2-propanol (CHROMASOLV, for high performance liquid chromatography [HPLC], 99.9%), dimethyl sulfoxide (DMSO) (anhydrous 99.9%) were all purchased from Sigma Aldrich, Ireland. Deionised water was purchased from Acros Organics and was used as necessary. Oregano essential oils along with silica are suitable for use in food products as demonstrated by approval by the EU. Silica is described by its registered E-number of E551 while oregano oil is produced from the steam distillation of plant leaves.

## *5.3.2 Methods*

### 5.3.2.1 Functionalisation of SBA-15 with APTES

The APTES was grafted to the surface of SBA-15 using DMSO as a novel solvent for this process. Briefly, 1 g of SBA was placed in a 50 mL flask with a magnetic stirrer bar and 20 mL of DMSO was added. To this solution, 2 mL of APTES was added dropwise and was reacted for 20 h before being washed with 20 mL of DMSO and 2-propanol, and finally washed with 3 aliquots of 20 mL deionised water. The SBA grafted with APTES (SBA-APTES) was then dried for 1 h in a vacuum oven at 90 °C.

### 5.3.2.2 Preparation of GPTS modified Si surface

Si wafers were prepared for GPTS attachment by cutting the Si into 1 $cm^2$ wafers before being placed into a round bottom flask with 40 mL of piranha solution (3:1 $H_2SO_4$:$H_2O_2$) for 1 h at 100 °C and then placed in distilled water until use for up to an hour. The GPTS was attached to the hydroxylated Si by immersing the wafers into a 9 % (v/v) GPTS in DMSO solution and reacted for 20 h at 90 °C. The grafted wafers were removed washed and sonicated in DMSO, 2-propanol and deionised water; dried using $N_2$ gas and placed in sample holders until further use.

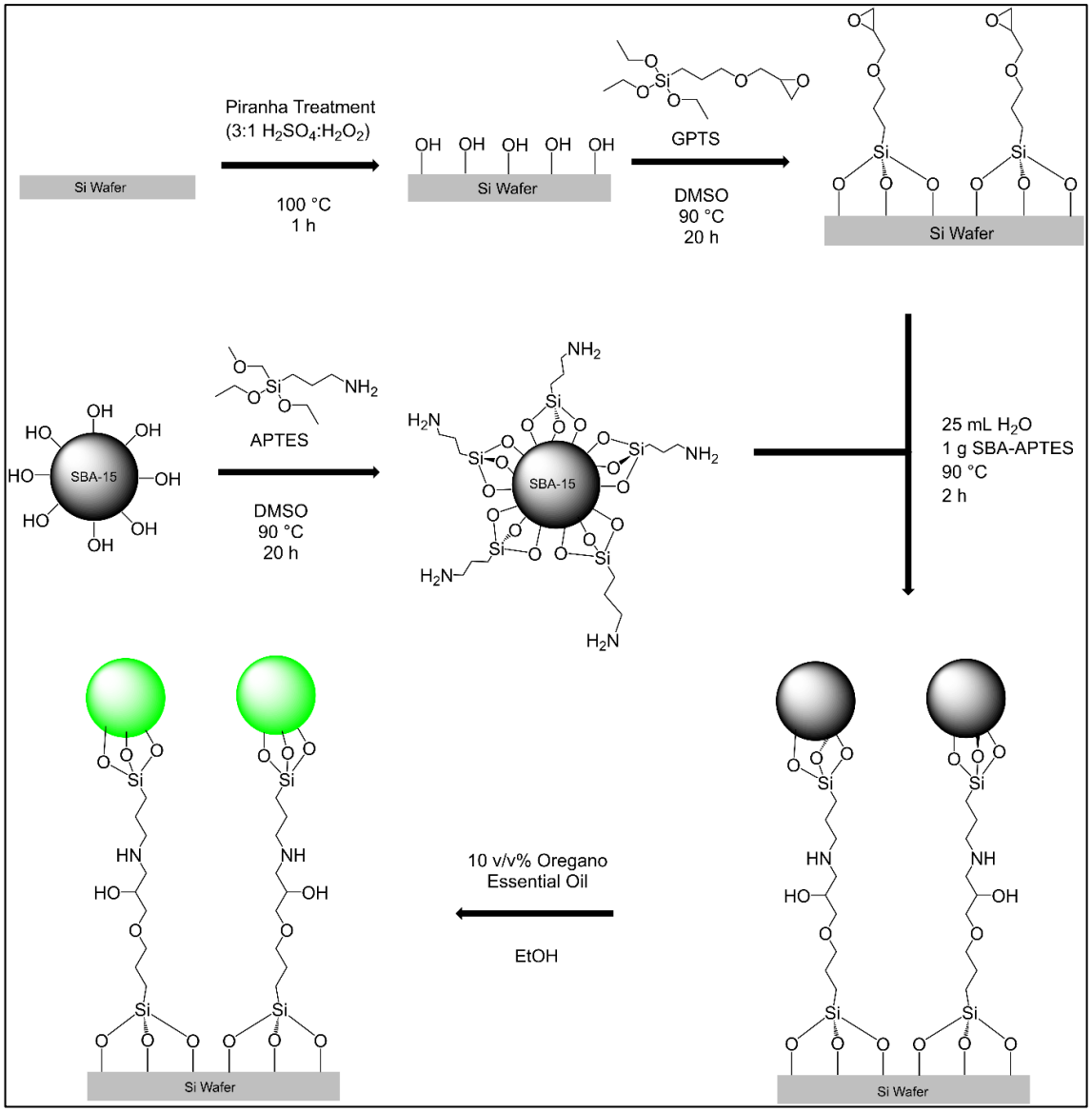


**Figure 5.1: Schematic outline of the synthesis of Si-GPTS-APTES-SBA modified surfaces.**

### 5.3.2.3 Attachment of Si-GPTS with SBA-APTES

The SBA-APTES was attached to the Si-GTPS surface as outlined in a schematic illustration shown in figure 5.1. Briefly, Si-GPTS wafers were submerged in 25 mL of deionised $H_2O$ to which 1 g of SBA-ATPES was added and the solution was then stirred for 2 hours at 90 °C before removal. To remove unbound SBA-APTES, the Si-GPTS-APTES-SBA was washed with deionised water and dried under a stream of $N_2$ gas.

#### 5.3.2.4 Loading of Oregano Essential

##### *5.3.2.4.1 Loading of SBA and SBA-ATPES*

Before loading OEO on bare SBA-15 and SBA-APTES, OEO was dissolved in absolute ethanol to make a 10 % v/v solution (as high concentrations of oil were found to be too viscous for loading). To this ethanolic solution, 0.5 g of either SBA-15 or SBA-APTES was added and then allowed to dry for 72 h at room temperature (21 °C) in a partially closed container to ensure full evaporation of the solvent.

##### *5.3.2.4.2 Loading of Si-GPTS-APTES-SBA*

Due to the process conditions, the OEO was loaded into the SBA after it was grafted to the Si surface. The Si-GPTS-APTES-SBA was loaded with 10 % v/v OEO in ethanol solution *via* drop casting directly onto wafer surface. Once the solution had attached onto the wafer, the OEO loaded wafer was gently washed with sterilised deionised water in order to remove unabsorbed EO solution and allowed to dry before use in the modified disk diffusion assay.

### *5.3.3 Characterisation*

#### 5.3.3.1 Electron Microscopy

Scanning electron microscopy (SEM) was carried out using a Karl Zeiss Ultra Plus field emission SEM with Gemini column. The samples were placed on carbon tape and then adhered to a stainless-steel stub before being placed in the instrument's chamber. It was operated at 5 keV and various magnifications were used as required. Transmission electron microscopy (TEM) was carried out using a JOEL 2100 at an operating voltage of 200 kV. The images were acquired in bright field mode.

#### 5.3.3.2 Fourier Transform Infrared (FTIR) spectroscopy

Fourier transform infrared spectroscopy (FTIR) analysis of OEO, SBA-15, SBA-OEO and SBA-ATPS-OEO was performed on a Varian 660-IR spectrometer (Varian Resolutions, Varian Inc, Victoria, Australia) using a diamond crystal ATR Golden Gate (Specac). Data was taken as the average of 32 scans at 2 $cm^{-1}$ resolution in a wavenumber range from 4000 - 500 $cm^{-1}$.

#### 5.3.3.3 X-ray photoemission spectroscopy (XPS)

X-ray photoelectron spectroscopy was performed under ultra-high vacuum conditions ($<5 \times 10^{-8}$ mbar) on a VG Scientific ESCAlab Mk II system equipped with a hemispherical analyser using Al Kα x-rays (1486.6 eV). The emitted photoelectrons were collected at a take-off angle of 90˚ from the disks' surface. The analyser pass energy for the survey scans was 200 eV. The binding energy scale was referenced to the adventitious carbon 1s core level scans at 284.8 eV. Core level scans of Si 2s, C 1s, N 1s and O 1s were examined.

#### 5.3.3.4 $N_2$ adsorption-desorption isotherms

The surface area, pore diameter, pore volume and pore size distribution measurements of the samples were performed based on the sorption technique using the Micromeritics Tristar II surface area analyser (Micrometrics, Norcross, GA, USA). The specific surface area of the samples was calculated using the multi-point Brunauer, Emmett and Teller ($S_{BET}$) method in the relative pressure range $P/P_0$ = 0.05-0.3. The specific pore volume, pore diameter and pore size distribution curves were computed based on the Barrett-Joyner-Halenda (BJH) method. The sorption analysis was carried out at 77 K and each sample was degassed under nitrogen for five hours at 200 ˚C prior to analysis.

#### 5.3.3.5 Elemental analysis

Elemental analysis was carried out on SBA-15 and SBA-OEO to determine the percentage of carbon, nitrogen, and hydrogen in the sample. The analysis was performed on Elementar vario EL cube elemental analyser. All samples analysed were carried out in triplicate.

#### 5.3.3.6 Thermal gravimetric analysis (TGA–DTG)

In order to evaluate the influence of temperature on the adsorbent stability, the adsorbents were studied by thermal gravimetric analysis. All TG/1st DTG curves were obtained on a Model TGA 2950 high-resolution thermogravimetric analyser V5.4a, on a temperature level from 30 to 800 °C with a warming speed of 5 °C $min^{-1}$ under nitrogen flow.

#### 5.3.3.7 Contact Angle

Dynamic contact angle and surface free energy were calculated from the advancing and receding water contact angles and were recorded on three different regions of each sample as outlined by Lundy et al[20]. Briefly, 60 nL of the liquid was dispensed on the material surface at a flow rate of 5 nL $s^{-1}$ using a microinjection syringe pump (SMARTouch, World Precision Instruments, Sarasota, FL, USA) with a needle ($\phi$ = 130 μm) and images were captured with a monochrome industrial camera (DMK 27AUR0135, The Imaging Source, Bremen, Germany). Contact angles were calculated using a piecewise polynomial fit (ImageJ, ver. 1.46, DropSnake plugin). The same procedure was used to determine diiodomethane ($CH_2I_2$) contact angles. The Surface free energy values were calculated from contact angles of deionized water and diiodomethane the using Owens–Wendt model (EQ. 5.1).

$$\frac{\gamma_{lv}(\cos\theta + 1)}{2} = \sqrt{\gamma_{lv}^{D} + \gamma_{sv}^{D}} + \sqrt{\gamma_{lv}^{P} + \gamma_{sv}^{P}} \qquad \textbf{EQ.5.1}$$

Surface energy values of $H_2O$ $\gamma_{lv}^D/\gamma_{lv}^P$ = 21.8/50.8 mJ $m^{-2}$ and $CH_2I_2$ $\gamma_{lv}^D/\gamma_{lv}^P$ = 48.5/2.3 mJ $m^{-2}$ were used.

#### 5.3.3.8 Atomic Force Microscopy

Atomic Force Microscope (AFM, Park systems, XE-7, South Korea) measurement on Si–GPTS were performed in non-contact mode with high resolution, silicon micro-cantilever tips. Topographic images were recorded at a resonance frequency of 270-300 kHz.

#### 5.3.3.9 Antimicrobial Assay

The antimicrobial activity of SBA-OEO and SBA-APTES-OEO against Gram-positive bacteria *S. aureus* and *B. cereus* and Gram-negative bacteria *E. coli* and *P. fluorescens* were assessed. Before use, all pure culture bacteria were grown for 18 h at 30 °C (*P. fluorescens* and *B. cereus*) or 37 °C (*S. aureus* and *E. coli*) in Mueller-Hinton broth (MHB) (Oxoid, UK) under constant agitation at 170 rpm on an orbital shaker (Innova 2300, New Brunswick™, Germany). These cultures were then used to determine the following:

#### 5.3.3.10 Minimum Inhibition Concentration (MIC) assay

The antimicrobial activity of SBA and SBA-APTES loaded with OEO was measured by determining the minimum inhibitory concentration (MIC) against the target microorganisms in a 96 flat bottom well tissue culture microplates (Sarstedt Inc., NC, USA) according to the NCCLS (2000) broth microdilution method as described by Kerry et al[21]. Bacterial strains were cultured overnight, at the appropriate temperature, adjusted to a final density of $10^5$ CFU/mL using maximum recovery diluent, and used as an inoculum within 15 min of preparation as outlined previously[22] by Sullivan et al[22]. Briefly, 100 µL of double-strength MHB (2XMHB) was added to each well in rows A to F, 200 µL of adjusted bacterial culture suspension was added to row H in columns 1–11 and 200 µL of sterile 2XMHB was added to column 12. In each well of

row G, 150 µL of SBA-OEO or SBA-APTES-OEO were dispensed in sterile distilled water and a threefold serial dilution was performed by transferring 50 µL of antimicrobial solutions from row G into the corresponding wells of row F through to row B. After mixing, 50 µL of the resultant mixture on row B was discarded. Finally, using a 12-channel electronic pipette (Model EDP3-Plus, Rainin, USA) 15 µL of the tested microorganisms was pipetted from each well in row H into the corresponding wells in row A followed by rows B to G. Positive (Row A) and negative growth controls (Column 12) were included in each assay plate. The inoculated plates were incubated in a wet chamber for 24 h at 30 °C (*P. fluorescens* and *B. cereus*) or 37°C (*E. coli* and *S. aureus*). After incubation, resazurin salt (0.015 %) was added to wells A – F (30 µL per well) and incubated for an additional 2 h as outlined by Elshikh et al[23]. Columns with no colour change (resazurins blue colour remained unchanged if no microbial growth; however, will turn pink if microbial growth occurs) were scored as above the MIC value. The lowest concentration showing inhibition of growth was considered to be the MIC for the target microorganisms. The test was repeated in triplicate.

#### 5.3.3.11 Modified Disk diffusion Assay

The antimicrobial activity of SBA functionalised surfaces containing OEO was also assessed using a modified agar diffusion method. MHA plates were swabbed with the target microorganism grown overnight at the appropriate temperature and adjusted to a final density of ~$10^5$ CFU $mL^{-1}$. SBA functionalised surfaces substrates containing OEO were then placed in the middle of the inoculated agar plates and incubated for 24 h at 30 °C (*P. fluorescens* and *B. cereus)* or 37 °C (*S. aureus* and *E. coli*). Streptomycin antibiotic disc (10 µg) was used as positive control, while unloaded SBA functionalised surfaces without EO was used as negative control. The inhibition zone around the substrate indicated the antimicrobial activity against the target microorganism. The inhibition zone (in millimetres) was measured using an electronic calliper (Model ECA 015D Moore &Wright, Paintain tools Ltd., Birmingham, UK).

#### 5.3.3.12 Statistical Analysis

Data for antimicrobial tests were analysed for means, standard deviations, and analysis of variance. One-way analysis of variance of data was carried out using the SPSS 24 for Windows (SPSS Statistical software, IBM Corp., Armonk, NY, USA) software package. Differences between pairs of means was resolved by means of confidence intervals using Tukey's test; the level of significance was set at $P<0.05$.

## 5.4 Results and Discussion

### *5.4.1 Functionalisation of SBA-15 with APTES*

The $N_2$ adsorption/desorption isotherms of the bare SBA-15 and SBA-APTES at 77°K are shown in figure 5.2(i & ii) while the properties including BET surface area ($S_{BET}$), BJH pore size ($D_{BJH}$), and total pore volume ($V_{total}$) are shown in table 5.1. Bare SBA-15 and SBA-APTES show type IV isotherm with H1 hysteresis and a sharp increase in adsorbed volume; characteristic of highly ordered mesoporous materials[14]. However, an overall reduction in the amount of $N_2$ absorbed after SBA grafting with APTES occurred due to filling of pores with the APTES molecule[15]. Textural properties calculated from the $N_2$ adsorption/desorption isotherms of SBA and SBA-APTES show that the $S_{BET}$ for pure SBA and SBA-APTES was 436.33 and 200.60 $m^2\ g^{-1}$ , respectively indicating that the surface area of the SBA-APTES is lower than SBA and was in agreement with Hernández-Morales et al.[13].

**Table 5.1 BET specific surface area ($S_{BET}$), BJH pore size ($D_{BJH}$), and total pore volume ($V_p$) properties of bare SBA-15 and SBA-APTES.**

| | **$S_{BET}$ ($m^2\ g^{-1}$)** | **$V_p$ (cc $g^{-1}$)** | **$D_{BJH}$ (Å)** |
|---|---|---|---|
| SBA | 436 | 0.452 | 45 |
| SBA-APTES | 201 | 0.301 | 54 |

The pore size distribution curves of SBA- 15 and SBA-APTES were calculated from the $N_2$ adsorption/desorption isotherms using the BJH model. The pore sizes of SBA-15 and SBA-APTES were estimated from the peak positions of the BJH pore size distribution curves measured from both the adsorption and desorption isotherms and were found to be 45 and 54 Å, respectively. These results are in good agreement with reports by Chong et al[14]. The pore volume of SBA-15 was 0.452 cc $g^{-1}$ and for SBA-APTES was 0.301 cc $g^{-1}$, indicating that the pore volume of the mesosphere was reduced after grafting with APTES and was in agreement with the literature[13,14,24].

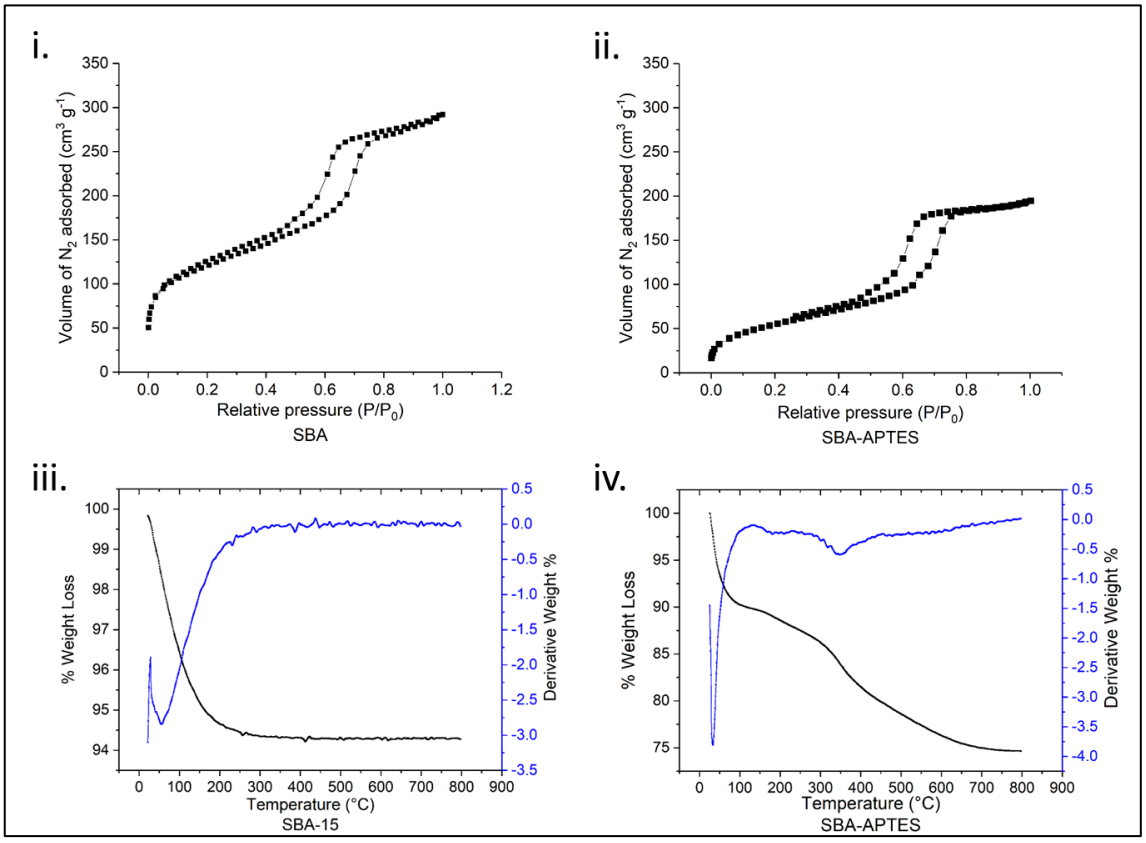


**Figure 5.2: Nitrogen adsorption/desorption isotherms at 77°K for (i.) SBA-15 and (ii) SBA-APTES and TGA curves and first derivative of bare (iii) SBA-15 and (iv) SBA-APTES.**

TGA analysis of SBA and SBA-APTES measuring weight loss curves are shown in figure 5.2 (iii & iv). Regarding SBA-15, the initial weight loss of 4.8 % is associated with the removal of

physisorbed water. The further weight loss of 0.8 % is due to the removal of chemisorbed water. The final weight loss 0.1 % was then attributed to the silanol groups which decompose to release water and subsequently the formation of silane bridges on the SBA surface. Likewise, TGA analysis of SBA-APTES has an initial weight loss of 10.4 % associated with the removal of physisorbed water, while a further 3.5 % was from the removal of chemisorbed water on the SBA-APTES surface. Furthermore, decomposition of the APTES can been seen over the 300 - 400 °C range and resulted in an overall weight loss of 4.65 % [13,25]. The final weight loss is associated with the dehydroxylation by condensation of silanols on the surface of the SBA-APTES [14]. The larger weight loss observed with respect to bare SBA-15 has been attributed to the presence of the amino groups. Those groups have high thermal stability (above 250 °C) suggesting that the SBA-15 silica sample has a stabilizing effect on the temperature of decomposition of the surface species[13].

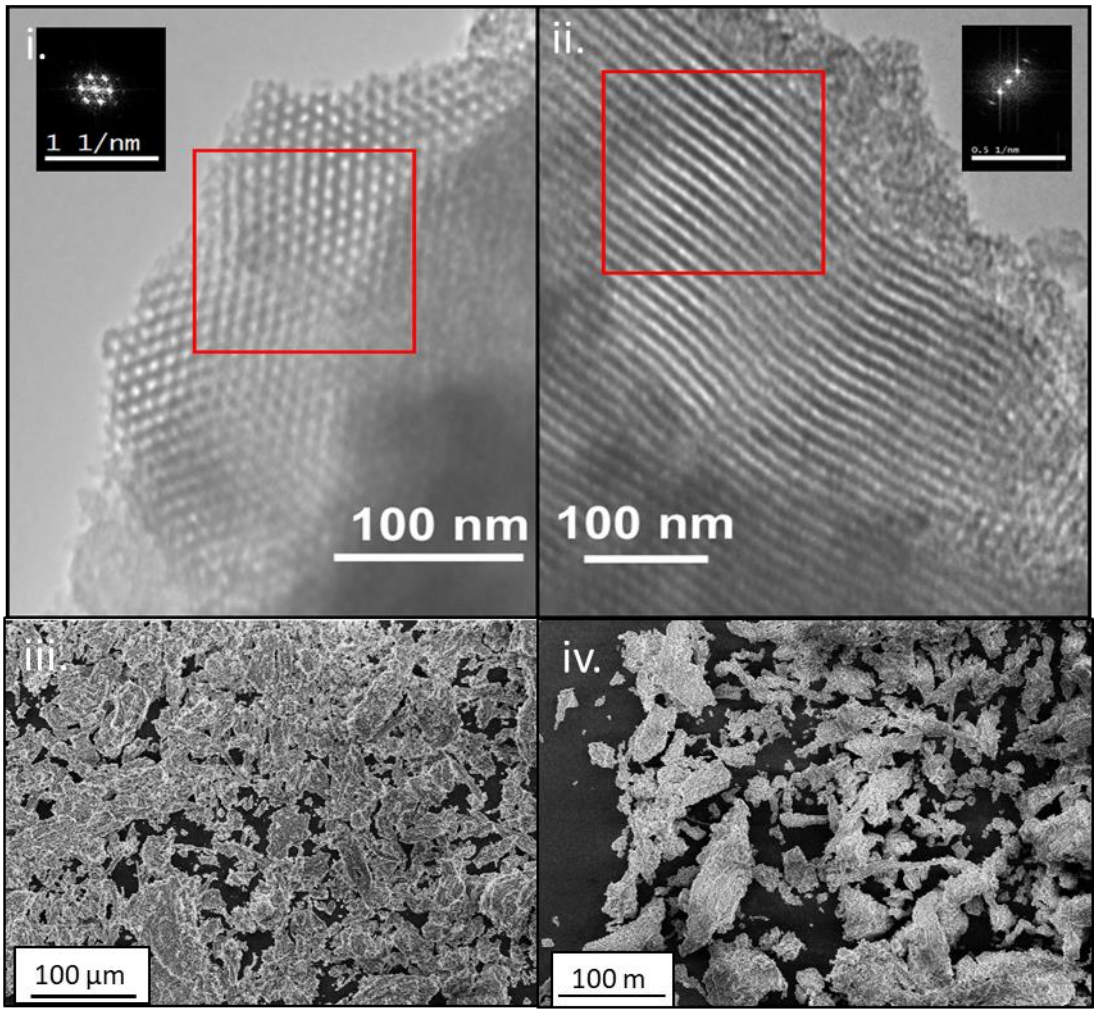


**Figure 5.3:** **TEM images of the SBA-15 showing well-ordered hexagonal array of mesopores (i) and parallel nanotubular pores (ii) with inset the FFT analysis and SEM images of SBA-15 (iii) and SBA-APTES (iv).**

The structure of bare SBA-15 was also analysed using TEM (Figure 5.3). TEM analysis shows a well-ordered hexagonal array structure (Figure 5.3.i) with nanotubular pores (Figure 5.3.ii) typical of SBA materials and have been widely reported and these results were further confirmed by using Fast Fourier Transform (FFT) analysis; showing the crystal lattice of the SBA-15 has a well-ordered hexagonal array structure with nanotubular pores (Figure 5.3.i & ii. (inset))[13]. SEM analysis of SBA-15 and SBA-APTES are also shown in figure 5.3. No major apparent differences were observed between either the SEM for SBA- 15 (Figure 5.3.iii) or SBA-APTES (Figure 5.3.iv)

which indicates that the APTES forms a coating over the SBA-15 and these results are in agreement with Munguía-Cortés et al[26].

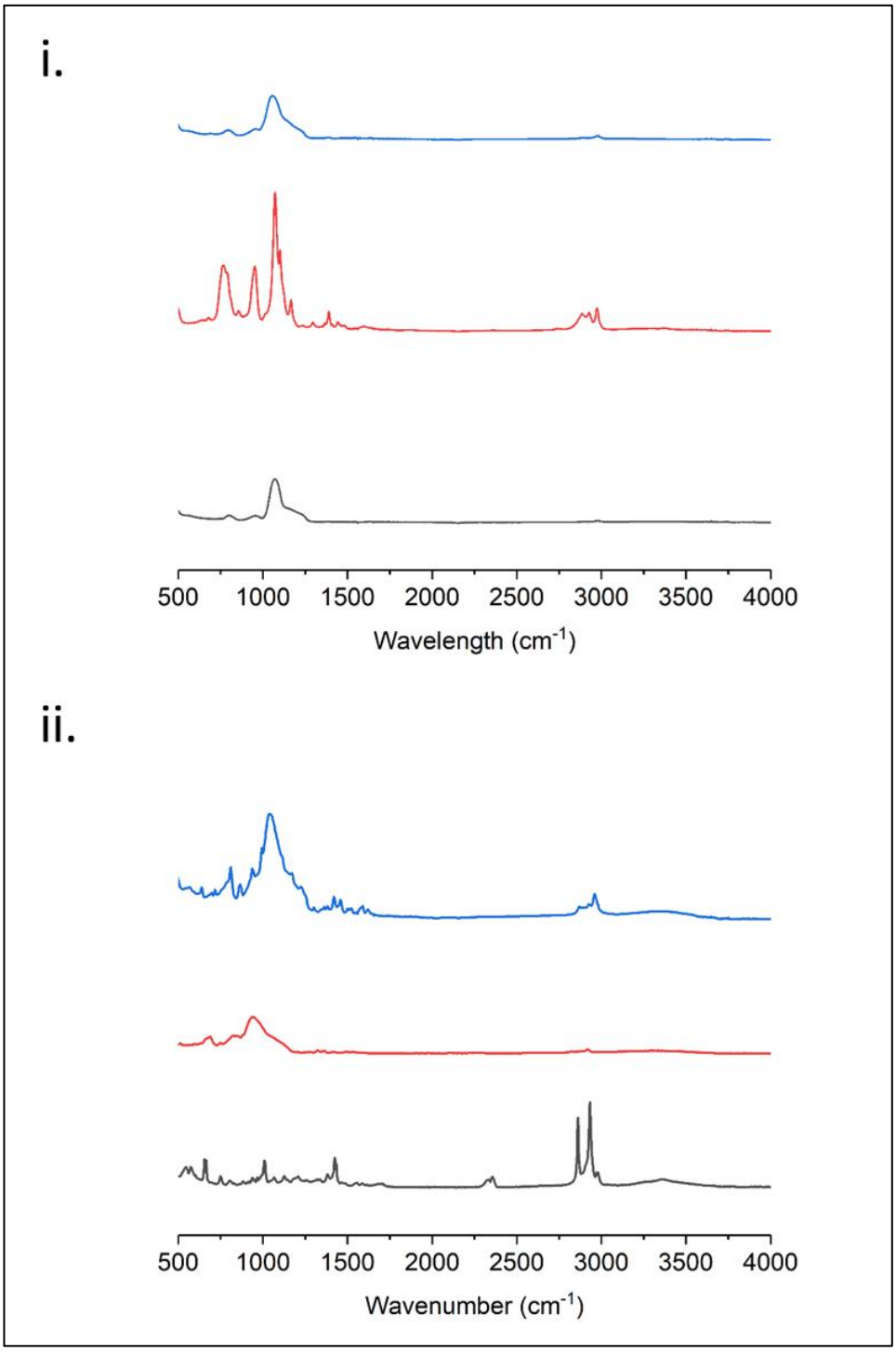


**Figure 5.4: FTIR spectra (i.) of SBA (—), APTES (—), and SBA-APTES (—) and FTIR spectra (ii.) of OEO (—), SBA-OEO (—), and SBA-APTES-OEO (—), between 2700 – 3200 $cm^{-1}$.**

The FTIR spectrum of pure SBA-15, pure APTES, and the functionalised SBA-APTES are shown in figure 5.4.i. SBA-15 showed major peaks at the 1000 – 1130 $cm^{-1}$ range which are the symmetrical and asymmetrical stretching of the Si-O-Si backbone of SBA, 3400 $cm^{-1}$ from the silanol groups that cover the surface of SBA[14] and are cross hydrogen bonding with adsorbed water[15] and at 3740 $cm^{-1}$ which corresponds to the symmetric stretching of terminal Si – O – H. With respect to pure APTES, the FTIR spectra shows characteristic peaks at the 1000 – 1130 $cm^{-1}$ range which are characteristic of symmetrical and asymmetrical stretching of Si-O groups, 1388 $cm^{-1}$ which is attributed to stretching C – N and at 2884, 2962 and 2974 are attributed to stretching C – H bonds. Moreover, a C – O terminal was observed at 1070 $cm^{-1}$ and at 1600 $cm^{-1}$ due to the H bending on the N of amine group. Regarding SBA-APTES, several new peaks emerge compared to SBA-15 due the presence of APTES at; 2927 and 2857 $cm^{-1}$ greater intensity of the peaks was observed due to a vibrational stretching C – H groups from the APTES, at 3300 – 3360 $cm^{-1}$ which is attributed to a combination of asymmetrical and symmetrical $NH_2$ stretches and at 1646 $cm^{-1}$ due to the H bending on the N of $NH_2$. When comparing the spectra of SBA and ATPES to SBA-ATPES, peak characteristic of both SBA and APTES were observed. Furthermore, the disappearance of the terminal Si – OH stretch at 3740 $cm^{-1}$ would suggest that the ethoxy group from the ATPES has bound to the surface of the SBA.

Overall, these results indicate that APTES has been grafted on to the surface of SBA-15 and are in agreement with results in the literature[27–29]. The proposed mechanism of SBA-15 functionalisation with APTES was through the condensation and hydrolysis of the terminal Si – OH from the SBA-15 with the alkoxy group ($-OCH_2CH_3$) of ATPES, releasing $H_2O$ and forming a stable covalent bond between SBA and APTES as previously outlined in figure 5.1 [28,30,31].

### *5.4.2 Attachment of GPTS to Si coupons to develop Si-GPTS-ATPES-SBA materials*

As previously outlined, a schematic representation of the functionalisation of silicon wafer surfaces with GPTS followed by reaction with the amine on the SBA-APTES to form a Si-GPTS-APTES-SBA active surface is shown in figure 5.1. The GPTS can attach to piranha treated Si wafers due to removal of deposited organic contaminants and increasing the density of – OH moieties on the Si wafer surface, facilitating the functionalisation of the Si surface through silanisation with the methoxy groups of GPTS *via* a hydrolysis reaction mechanism as outlined elsewhere by Vejayakumaran et al and Wach et al[17,31]. The irreversible attachment of SBA-APTES to Si-GPTS occurs *via* a nucleophilic epoxide ring opening reaction between the amine groups from APTES and oxirane ring from GPTS resulting in the covalent grafting of SBA-APTES to Si-GPTS[24,32,33]. To determine the attachment of the Si-GPTS surface to the SBA-APTES; dynamic contact angle, AFM and XPS analyses were carried out.

**Table 5.2 Dynamic contact angle and surface free energy of Si-GPTS and Si-GPTS-APTES-SBA.**

| Sample | Contact Angle ($H_2O$) (°) | Contact Angle ($I_2CH_2$) (°) | Surface Free Energy (mJ $m^{-2}$) |
|---|---|---|---|
| Si-GPTS | 56.90±2.1 | 39.90±0.5 | 48.6 ± 1.8 |
| Si-GPTS-APTES-SBA | 27.63±3.9 | 26.23±5.3 | 66.70 ± 5.8 |

Dynamic contact angle measurements of Si – OH (piranha treated Si), Si-GPTS and Si-GPTS-APTES-SBA are shown in table 5.2. For piranha treated Si wafers (Si-OH), the wettability was found to be 8.57°; however, after functionalisation of the Si-OH with GPTS, the wettability decreased to 56.90 ° as a result of the substitution of the hydrophilic hydroxyl sites with the more hydrophobic GPTS chains[27]. Following the functionalisation of the Si-GPTS with SBA-APTES, the wettability was found to decrease with respect to Si-GPTS to 26.23 ° due to the presence of the hydrophilic APTES on the surface. In addition, the dynamic contact angle of Si-

GPTS and Si-GPTS-APTES-SBA was also measured using the dispersive solvent diiodomethane and results showed a contact angle of 39.90 ° and 26.23 ° for Si-GPTS and Si-GPTS-APTES-SBA, respectively. Using the dispersive angle, the surface free energy was determined using the Owens-Wendt model (Eq. 5.1). Results indicate that the surface free energy (SFE) was 48.60 and 66.70 mJ $m^{-2}$ for Si-GPTS and Si-GPTS-APTES-SBA, respectively. The change in the SFE indicates that the surface has changed and most likely in conjunction with the tools show the SBA-APTES has attached to the Si-GPTS substrate. Moreover, the higher SFE reported for Si-GPTS-APTES-SBA would suggest that these materials are more reactive and will therefore interact better with the antimicrobial EO.

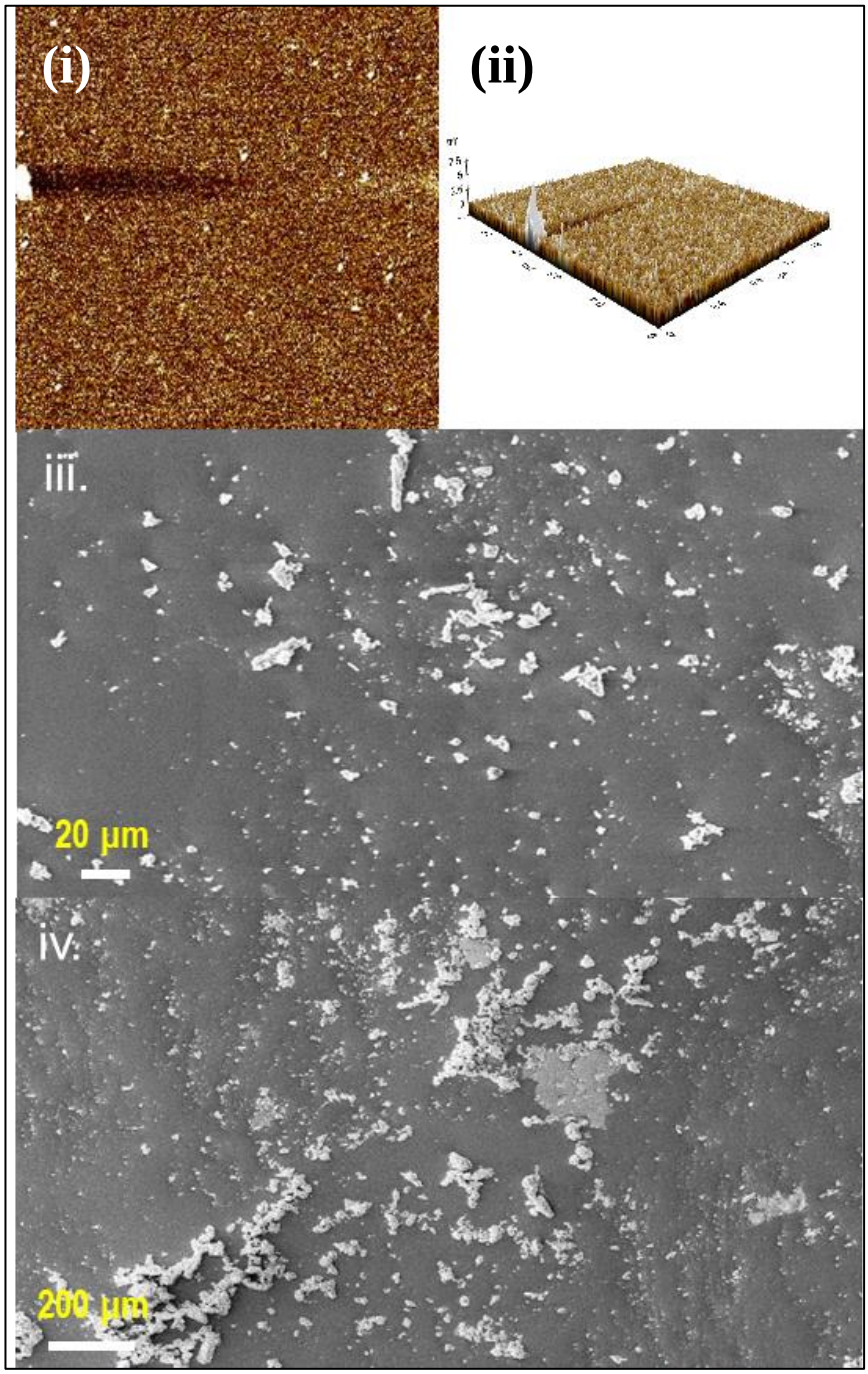


**Figure 5.5:** **AFM images of Si-GPTS showing (i) 2D and (ii.) 3D topographical images; and SEM images of Si-GPTS-APTES-SBA surface at 20 (iii.), and 200 (iv.) µm.**

Additionally, the thickness and topographical feature of Si-GPTS were measured using AFM analysis (Figure 5.5.i). AFM analysis showed that Si-GPTS has a smooth topographical surface

with small agglomerate features and may perhaps be due to excessive nucleation of GPTS onto the Si-OH surface and the surface roughness (Ra) values was 0.219 nm.

XPS analysis was used to examine the binding energies of Si 2p, O 1s, N 1s and C 1s core electrons of Si-GPTS-APTES-SBA (Figure 5.6.i). The XPS spectrum (Figure 5.6.ii) consists of peaks at 103 eV and 97.5 eV from organic and elemental silica, respectively. The O 1s scan (Figure 5.6.iii) shows peaks at 532 and 529 eV which are attributed to Si-$O_2$ and organic C – O, respectively[34]. In addition, peaks occurred in the N 1s spectra (Figure 5.6.iv) because of the amine groups present in APTES. The three different components of the peaks in the N 1s spectra were related to: non-protonated, primary amino groups (399.6 eV), formamide groups (400.3 eV), and hydrogen bonded or protonated amino species (401.5 eV)[17]. Furthermore, from the XPS survey the presence of an amino group peak indicates that the attachment of SBA-APTES to the surface of Si-GPTS has occurred. The C 1s scan (Figure 5.6.v) also revealed peaks at 284 eV from C – H and C – C of the alkyl group of GPTS and from adventitious hydrocarbon contamination, while the peak at 286.6 eV was from C – O – C and the oxirane ring of the GPTS. SEM analysis of Si-GPTS-APTES-SBA surfaces are shown in figure 5.3.iii and iv. Results indicated that SBA-APTES was bound to the Si-GPTS surface. Moreover, SEM showed that the SBA-APTES is not forming multilayer agglomerates, but instead isolated “specks”. Overall, these results indicate that the SBA-APTES has been attached to the functionalised Si-GPTS modified surface.

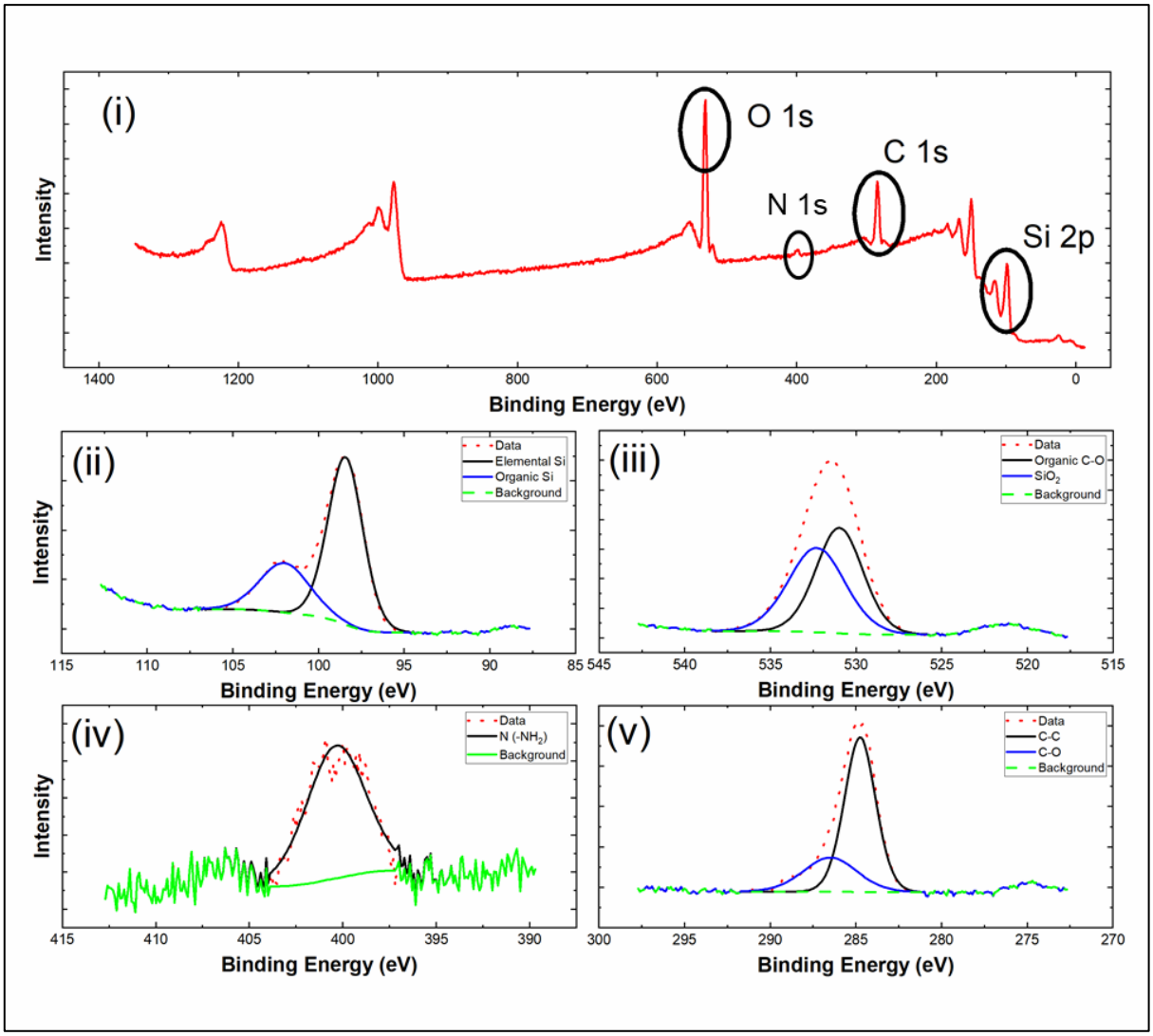


**Figure 5.6:** **XPS survey spectra (i) of Si-GPTS-APTES-SBA with binding energies of Si 2p (ii), O1s (iii), N1s (iv) and the C1s (v) scans.**

## *5.4.3 OEO loading and antimicrobial activity of SBA & SBA-APTES*

The C, H, N elemental analysis of SBA-15 and SBA-OEO are shown in table 5.3. Results indicate that after OEO loading, an increase in the amount of C, H, and N was observed due to secondary metabolites that make up EO's. In addition, the weight of SBA-OEO and SBA-APTES-OEO was found to increase by 65 and 63 % after loading indicating that the OEO has been successfully adsorbed into the SBA voids (data not shown).

**Table 5.3 Elemental analysis of C, H, and N before OEO loading (SBA-15 and SBA-APTES) and after OEO loading.**

| Element | SBA-15 | SBA-OEO |
|---|---|---|
| C | Nil | 29.63 |
| H | 0.74 | 3.99 |
| N | Nil | Nil |

FTIR spectra also confirmed successful loading of OEO into SBA (Figure 5.4.ii.). The FTIR spectra of the pure OEO showed sharp characteristic peaks at 2959 $cm^{-1}$ (-CH stretching), 1589 $cm^{-1}$ (N-H bending), 1458 $cm^{-1}$ (-$CH_2$ bending), 1253 $cm^{-1}$ (C-O-C stretching), 1117 $cm^{-1}$ (C-O-C stretching) and 937 $cm^{-1}$ (C-H bending)[35]. When the spectra of SBA-OEO and SBA-APTES-OEO are compared to the unloaded SBA-15 spectra (unloaded spectra previously outlined in figure 5.4.i), the presence of the characteristic peaks of OEO correspond to the wavenumber of the pure OEO indicating that OEO was loaded into the support material SBA-15 or SBA-APTES but apparently no modification or interaction between the OEO and SBA-15 occurred [35].

Upon successful loading of the OEO, the antimicrobial activity of SBA-OEO and SBA-APTES-OEO was assessed using a MIC assay and results showed that both SBA-OEO and SBA-APTES-OEO have good antimicrobial activity. The antimicrobial activity of bare SBA-15 and SBA-APTES was also assessed; however, no antimicrobial activity was observed for either (data not shown). For SBA-OEO, concentrations of 0.83 and 1.25 mg $mL^{-1}$ were required to inhibit Gram-negative *E. coli* and *P. fluorescens*, respectively; while concentrations of 0.83 mg $mL^{-1}$ was required to inhibit growth of Gram-positive *S. aureus* and *B. cereus* (Figure 5.7). For SBA-APTES-OEO, concentrations of 0.83 mg $mL^{-1}$ were required to inhibit the growth of Gram-negative *E. coli* and *P. fluorescens*; while concentrations of 0.73 mg $mL^{-1}$ was required to inhibit growth of Gram-positive *S. aureus* and *B. cereus* (Figure 5.7). These results indicate that SBA functionalisation with APTES enhanced the antimicrobial activity of OEO against Gram-positive

*S. aureus* and *B. cereus* bacteria compared to SBA-OEO; however, these results were not statistically ($P>0.05$) different. Nonetheless, the better antimicrobial activity of SBA-APTES-OEO against Gram-positive bacteria compared to SBA-OEO may perhaps be due to the functionalisation of SBA with ATPES changing the release profile of the secondary metabolites of OEO; therefore, effecting the interaction of OEO with the bacterial cell [36]. It has also shown that the anchoring of molecules with positive charges on the surface of mesoporous silica particles can reduce microbial growth [19]. The exact mechanism of antimicrobial action of OEO is not fully understood; however, a synergistic action of the secondary metabolites such as p-cymene, thymol, and carvacol present in oregano EO's has been reported [5]. In particular, carvacrol can disintegrate outer membranes of Gram-negative bacteria while in Gram-positive bacteria the membrane permeability is altered allowing permeation cations like $H^+$ and $K^+$ [5] and p-cymene, while not inherently antimicrobial, has a high affinity for bacterial cell membranes where it can substitute itself into the cell membrane altering the physiological barrier properties facilitating easier access for other more potent antimicrobial compounds [37]. Moreover, the shape of the bacteria has also been reported to affect the antimicrobial efficacy of EO's, where rod shaped cell being more sensitive than coccoid shaped cells [1].

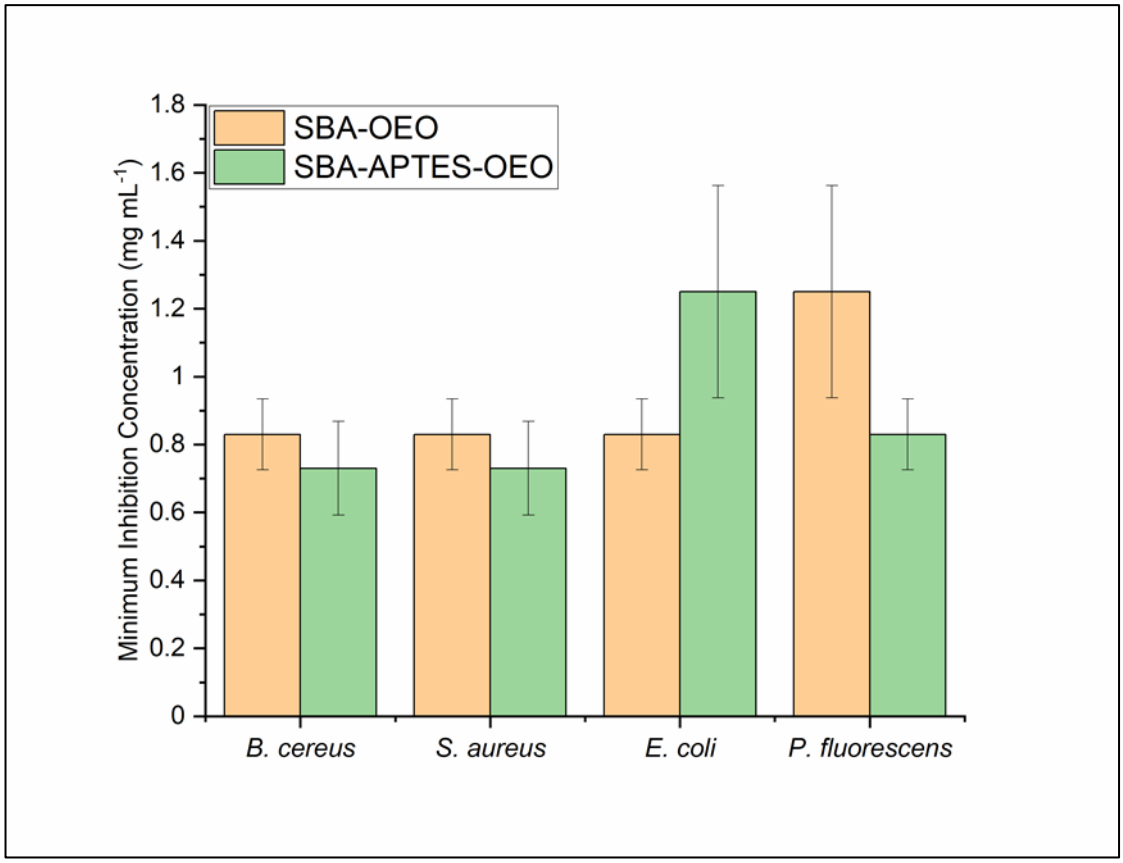


**Figure 5.7: Minimum inhibition concentration (b.) of SBA-OEO ( ) and SBA-APTES-OEO ( ) against B. cereus, S. aureus, E. coli and P. fluorescens. Error bars represent standard error of the mean of analysis of triplicate samples.**

Moreover, results indicated that Gram-positive showed a greater susceptibility to SBA-OEO and SBA-APTES-OEO compared to Gram-negative bacteria. Increased Gram-positive bacteria susceptibility has been widely reported in the literature and is believed to be through the lipophilic ends on lipoteichoic acid in the cell membrane of Gram-positive bacteria enabling the penetration of hydrophobic EO constituents into the internal cell structure [38]. Conversely, the reduced susceptibility of Gram-negative bacteria was attributed to the role of extrinsic membrane proteins and cell wall lipopolysaccharides limiting the diffusion of hydrophobic EO compounds into the microorganism[38].

Nevertheless, when disk diffusion assay was carried out on Si-GPTS-ATPES-SBA-OEO surfaces; no antimicrobial activity was observed (data not shown). This may perhaps be due to several factors such as insufficient amount of SBA-APTES attached on the surface of the Si-GPTS for the OEO to be absorbed into. For example, assuming that SBA was arranged in a spherical close packed order and had an average diameter of 20 µm, the total number of SBA-15 units on the surface can be estimated to be 250,000 particles per 1 $cm^2$. Then the volume of the SBA-15 can be worked out using $4/3\pi r^3$ to be 1.046 µL. The average load ability of the SBA was worked out from the weight before and after OEO loading and was found to be approximately 35 %. Therefore, we can assume that the max volume of OEO on a 1 $cm^2$ surface is 0.336 µL. Using the max MIC of 1.25 mg $mL^{-1}$ we can determine that the volume of OEO need for MIC was 0.26 µL. However, using image J to estimate the SBA surface coverage from the SEM analysis (Figure 4 iii and iv.), showed that coverage was approximately 10 %, and, therefore, well below the required volume to show an antimicrobial effect. Moreover, perhaps the interaction of APTES with the GPTS surface reduces the number of available pores for adsorption of the OEO, therefore, "blocking" its uptake into the mesospheric voids. To overcome these issues future investigations could look at other methods of OEO loading such as volatilisation/vaporisation of the essential oil at low temperatures (e.g. 40°C) as outlined by Bernardos et al[39] or perhaps through the use mesoporous silica nanoparticles as outlined by Muriel-Galet et al[40].

## 5.5 Conclusion

In this work we have presented a novel approach to attach SBA-APTES to a GPTS modified surface for application and have demonstrated the use of SBA-15 and SBA-APTES mesoporous materials are as an effective support material for volatile OEO. Moreover, the modification of SBA-15 with APTES was not found to negatively impact the antimicrobial activity of OEO, compared to unmodified SBA-15, against common food spoilage microorganisms *E. coli*, *B. cereus*, *S. aureus*, and *P. fluorescens*. However, when SBA-APTES was attached to a GPTS

modified surface no antimicrobial activity was observed. Therefore, results from this study indicated that the attachment of SBA to a functionalised surface has significant roadblocks to its application in food packaging as insufficient SBA carrier was attached to the GPTS modified surface and therefore, apparently there was insufficient OEO on the surface. Consequently, the attachment of SBA as a carrier to food packaging would appear not to be an effective or simple method to deliver antimicrobial OEO. This work suggests that delivery systems integrated to food packaging may afford very significant challenges in developing products that exhibit increased shelf-life. The work suggests that a more 'direct' application methods may be required to be developed. Given the strong antimicrobial activity and GRAS nature of SBA-OEO and SBA-APTES-OEO, they could potentially be applied *via* a simple "sprinkle" method (like salt) directly on a food product. Moreover, due to the strong absorption properties of SBA materials, other EO's such as thyme, rosemary etc. can be used as a flavour delivering system. However, toxicity studies of these materials need to be carried out.

## 5.6 References

[1] D.J. Sullivan, S. Azlin-Hasim, M. Cruz-Romero, E. Cummins, J.P. Kerry, M.A. Morris, Natural antimicrobial materials for use in food packaging, Elsevier Inc., 2017. https://doi.org/10.1016/B978-0-12-811982-2.00011-1.

[2] F. Donsì, G. Ferrari, Essential oil nanoemulsions as antimicrobial agents in food, J. Biotechnol. 233 (2016) 106–120. https://doi.org/10.1016/j.jbiotec.2016.07.005.

[3] R. Ribeiro-Santos, M. Andrade, N.R. de Melo, A. Sanches-Silva, Use of essential oils in active food packaging: Recent advances and future trends, Trends Food Sci. Technol. 61 (2017) 132–140. https://doi.org/10.1016/j.tifs.2016.11.021.

[4] R. Amorati, M.C. Foti, L. Valgimigli, Antioxidant activity of essential oils, J. Agric. Food Chem. 61 (2013) 10835–10847. https://doi.org/10.1021/jf403496k.

[5] M. Hyldgaard, T. Mygind, R.L. Meyer, Essential oils in food preservation: Mode of action, synergies, and interactions with food matrix components, Front. Microbiol. 3 (2012) 1–24. https://doi.org/10.3389/fmicb.2012.00012.

[6] A.R. Bilia, C. Guccione, B. Isacchi, C. Righeschi, F. Firenzuoli, M.C. Bergonzi, Essential oils loaded in nanosystems: A developing strategy for a successful therapeutic approach, Evidence-Based Complement. Altern. Med. 2014 (2014). https://doi.org/10.1155/2014/651593.

[7] J.R. Calo, P.G. Crandall, C.A. O'Bryan, S.C. Ricke, Essential oils as antimicrobials in food systems - A review, Food Control. 54 (2015) 111–119. https://doi.org/10.1016/j.foodcont.2014.12.040.

[8] C. Turek, F.C. Stintzing, Stability of essential oils: A review, Compr. Rev. Food Sci. Food Saf. 12 (2013) 40–53. https://doi.org/10.1111/1541-4337.12006.

[9] I. Sánchez-Ortega, B.E. García-Almendárez, E.M. Santos-López, A. Amaro-Reyes, J.E. Barboza-Corona, C. Regalado, Antimicrobial edible films and coatings for meat and meat products preservation, Sci. World J. 2014 (2014). https://doi.org/10.1155/2014/248935.

[10] L. nan Sun, L. xin Lu, X. lin Qiu, Y. li Tang, Development of low-density polyethylene antioxidant active films containing α-tocopherol loaded with MCM-41(Mobil Composition of Matter No. 41) mesoporous silica, Food Control. 71 (2017) 193–199. https://doi.org/10.1016/j.foodcont.2016.06.025.

[11] M. Ruiz-Rico, É. Pérez-Esteve, A. Bernardos, F. Sancenón, R. Martínez-Máñez, M.D. Marcos, J.M. Barat, Enhanced antimicrobial activity of essential oil components immobilized on silica particles, Food Chem. 233 (2017) 228–236. https://doi.org/10.1016/j.foodchem.2017.04.118.

[12] A. Bernardos, L. Kourimská, Applications of mesoporous silica materials in food - A review, Czech J. Food Sci. 31 (2013) 99–107. https://doi.org/10.17221/240/2012-cjfs.

[13] V. Hernández-Morales, R. Nava, Y.J. Acosta-Silva, S.A. MacÍas-Sánchez, J.J. Pérez-Bueno, B. Pawelec, Adsorption of lead (II) on SBA-15 mesoporous molecular sieve functionalized with -NH2 groups, Microporous Mesoporous Mater. 160 (2012) 133–142. https://doi.org/10.1016/j.micromeso.2012.05.004.

[14] S.M. Chong, X.S. Zhao, Functionalization of SBA-15 with APTES and characterization of functionalized materials, J. Phys. Chem. B. 107 (2003) 12650–12657. https://doi.org/10.1021/jp035877+.

[15] E. Vilarrasa-García, J.A. Cecilia, S.M.L. Santos, C.L. Cavalcante, J. Jiménez-Jiménez, D.C.S. Azevedo, E. Rodríguez-Castellón, CO2 adsorption on APTES functionalized mesocellular

foams obtained from mesoporous silicas, Microporous Mesoporous Mater. 187 (2014) 125–134. https://doi.org/10.1016/j.micromeso.2013.12.023.

[16] B. Riegel, S. Blittersdorf, W. Kiefer, S. Hofacker, M. Müller, G. Schottner, Kinetic investigations of hydrolysis and condensation of the glycidoxypropyltrimethoxysilane/aminopropyltriethoxy-silane system by means of FT-Raman spectroscopy I, J. Non. Cryst. Solids. 226 (1998) 76–84. https://doi.org/10.1016/S0022-3093(97)00487-0.

[17] A. Wach, P. Natkański, M. Drozdek, B. Dudek, P. Kuśtrowski, Functionalization of mesoporous SBA-15 silica by grafting of polyvinylamine on epoxy-modified surface, Polimery. 62 (2017) 516–524.

[18] S.Y. Park, M. Barton, P. Pendleton, Mesoporous silica as a natural antimicrobial carrier, Colloids Surfaces A Physicochem. Eng. Asp. 385 (2011) 256–261. https://doi.org/10.1016/j.colsurfa.2011.06.021.

[19] M. Ruiz-Rico, É. Pérez-Esteve, C. de la Torre, A.I. Jiménez-Belenguer, A. Quiles, M.D. Marcos, R. Martínez-Máñez, J.M. Barat, Improving the Antimicrobial Power of Low-Effective Antimicrobial Molecules Through Nanotechnology, J. Food Sci. 83 (2018) 2140–2147. https://doi.org/10.1111/1750-3841.14211.

[20] R. Lundy, C. Byrne, J. Bogan, K. Nolan, M.N. Collins, E. Dalton, R. Enright, Exploring the Role of Adsorption and Surface State on the Hydrophobicity of Rare Earth Oxides, ACS Appl. Mater. Interfaces. 9 (2017) 13751–13760. https://doi.org/10.1021/acsami.7b01515.

[21] M.C. Cruz-Romero, T. Murphy, M. Morris, E. Cummins, J.P. Kerry, Antimicrobial activity of chitosan, organic acids and nano-sized solubilisates for potential use in smart

antimicrobially-active packaging for potential food applications, Food Control. 34 (2013) 393–397. https://doi.org/10.1016/j.foodcont.2013.04.042.

[22] D.J. Sullivan, S. Azlin-Hasim, M. Cruz-Romero, E. Cummins, J.P. Kerry, M.A. Morris, Antimicrobial effect of benzoic and sorbic acid salts and nano-solubilisates against Staphylococcus aureus, Pseudomonas fluorescens and chicken microbiota biofilms, Food Control. 107 (2020) 106786. https://doi.org/10.1016/j.foodcont.2019.106786.

[23] M. Elshikh, S. Ahmed, S. Funston, P. Dunlop, M. McGaw, R. Marchant, I.M. Banat, Resazurin-based 96-well plate microdilution method for the determination of minimum inhibitory concentration of biosurfactants, Biotechnol. Lett. 38 (2016) 1015–1019. https://doi.org/10.1007/s10529-016-2079-2.

[24] R. Rajan, E. Rainosalo, S.P. Thomas, S.K. Ramamoorthy, J. Zavašnik, J. Vuorinen, M. Skrifvars, Modification of epoxy resin by silane-coupling agent to improve tensile properties of viscose fabric composites, Polym. Bull. 75 (2018) 167–195. https://doi.org/10.1007/s00289-017-2022-2.

[25] X.S. Zhao, G.Q. Lu, a K. Whittaker, G.J. Millar, H.Y. Zhu, Comprehensive study of surface chemistry of MCM-41 using Si-29 CP/MAS NMR, FTIR, pyridine-TPD, and TGA, J. Phys. Chem. B. 101 (1997) 6525–6531. https://doi.org/10.1021/jp971366+.

[26] L. Munguía-Cortés, I. Pérez-Hermosillo, R. Ojeda-López, J.M. Esparza-Schulz, C. Felipe-Mendoza, A. Cervantes-Uribe, A. Domínguez-Ortiz, APTES-functionalization of SBA-15 using ethanol or toluene: Textural characterization and sorption performance of carbon dioxide, J. Mex. Chem. Soc. 61 (2017) 273–281. https://doi.org/10.29356/jmcs.v61i4.457.

[27] M. Lazghab, K. Saleh, P. Guigon, Functionalisation of porous silica powders in a fluidised-bed reactor with glycidoxypropyltrimethoxysilane (GPTMS) and

aminopropyltriethoxysilane (APTES), Chem. Eng. Res. Des. 88 (2010) 686–692. https://doi.org/10.1016/j.cherd.2009.11.005.

[28] M. Moritz, M. Łaniecki, SBA-15 mesoporous material modified with APTES as the carrier for 2-(3-benzoylphenyl)propionic acid, Appl. Surf. Sci. 258 (2012) 7523–7529. https://doi.org/10.1016/j.apsusc.2012.04.076.

[29] A. Szegedi, M. Popova, I. Goshev, J. Mihály, Effect of amine functionalization of spherical MCM-41 and SBA-15 on controlled drug release, J. Solid State Chem. 184 (2011) 1201–1207. https://doi.org/10.1016/j.jssc.2011.03.005.

[30] Z. Luan, J.A. Fournier, J.B. Wooten, D.E. Miser, Preparation and characterization of (3-aminopropyl) triethoxysilane-modified mesoporous SBA-15 silica molecular sieves, Microporous Mesoporous Mater. 83 (2005) 150–158. https://doi.org/10.1016/j.micromeso.2005.04.006.

[31] P. Vejayakumaran, I.A. Rahman, C.S. Sipaut, J. Ismail, C.K. Chee, Structural and thermal characterizations of silica nanoparticles grafted with pendant maleimide and epoxide groups, J. Colloid Interface Sci. 328 (2008) 81–91. https://doi.org/10.1016/j.jcis.2008.08.054.

[32] T. Kamra, S. Chaudhary, C. Xu, N. Johansson, L. Montelius, J. Schnadt, L. Ye, Covalent immobilization of molecularly imprinted polymer nanoparticles using an epoxy silane, J. Colloid Interface Sci. 445 (2015) 277–284. https://doi.org/10.1016/j.jcis.2014.12.086.

[33] R. Rajan, P.A. Sreekumar, K. Joseph, M. Skrifvars, Thermal and Mechanical Properties of Chitosan Reinforced Polyhydroxybutyrate Composites, J. Appl. Polym. Sci. 124 (2011) 3357–3362. https://doi.org/10.1002/app.

[34] H. Du, G. He, T. Liu, L. Ding, Y. Fang, Preparation of pyrene-functionalized fluorescent film with a benzene ring in spacer and sensitive detection to picric acid in aqueous phase, J.

Photochem. Photobiol. A Chem. 217 (2011) 356–362. https://doi.org/10.1016/j.jphotochem.2010.11.004.

[35] S.F. Hosseini, M. Zandi, M. Rezaei, F. Farahmandghavi, Two-step method for encapsulation of oregano essential oil in chitosan nanoparticles: Preparation, characterization and in vitro release study, Carbohydr. Polym. 95 (2013) 50–56. https://doi.org/10.1016/j.carbpol.2013.02.031.

[36] M. Stanzione, N. Gargiulo, D. Caputo, B. Liguori, P. Cerruti, E. Amendola, M. Lavorgna, G.G. Buonocore, Peculiarities of vanillin release from amino-functionalized mesoporous silica embedded into biodegradable composites, Eur. Polym. J. 89 (2017) 88–100. https://doi.org/10.1016/j.eurpolymj.2017.01.040.

[37] S. Burt, Essential oils: Their antibacterial properties and potential applications in foods - A review, Int. J. Food Microbiol. 94 (2004) 223–253. https://doi.org/10.1016/j.ijfoodmicro.2004.03.022.

[38] P. Tongnuanchan, S. Benjakul, Essential Oils: Extraction, Bioactivities, and Their Uses for Food Preservation, J. Food Sci. 79 (2014) 1–19. https://doi.org/10.1111/1750-3841.12492.

[39] A. Bernardos, M. Bozik, S. Alvarez, M. Saskova, E. Perez-Esteve, P. Kloucek, M. Lhotka, A. Frankova, R. Martinez-Manez, The efficacy of essential oil components loaded into montmorillonite against Aspergillus niger and Staphylococcus aureus, Flavour Fragr. J. 34 (2019) 151–162. https://doi.org/10.1002/ffj.3488.

[40] V. Muriel-Galet, É. Pérez-Esteve, M. Ruiz-Rico, R. Martínez-Máñez, J.M. Barat, P. Hernández-Muñoz, R. Gavara, Anchoring gated mesoporous silica particles to ethylene vinyl alcohol films for smart packaging applications, Nanomaterials. 8 (2018). https://doi.org/10.3390/nano8100865.

# *Chapter 6*

# *Conclusions & Future Work*

## 6.1 Conclusions and Future Work

The drive for more efficient and robust materials to deal with some of the challenges mentioned throughout this thesis, has continued increasing the interest into porous materials. The use of mesoporous silicas as supports and potential devices including hybrid materials, is an ever-expanding field with novel proof of concept ideas and a continuation of vast literature in this area.

Chapter 1 introduced the fundamental background of silicon dioxide materials including properties relating to silicas and wafers, synthesis methods including mechanisms of different routes and also functionalisation of these materials which is a critical step in the formation of products. The discussion of naturally occurring silicas compared to the large variation in synthetically produced silicas with differing sizes, morphologies, pore structures all the while having almost identical surface chemistry. It is this universal surface chemistry which give silicas with huge differences as mentioned, the ability to be grafted with an impossible number of functional groups or derivatives of such. It is therefore obvious that with these new surface functional groups, lead silicon dioxide materials to be a favourite for many applications. With other beneficial properties such as high surface areas, large pore diameters, regular pore structures and more offer porous silicas advantages over some competing materials. Applications such as chromatography where silica has been the backbone of separations for many decades and as support materials for catalysts. The uses of silica will continue to grow and with that more insights into how these materials will be optimised and made more efficient and robust going into the future.

Chapter 2 outlined the methods which were utilised throughout this thesis. It included the synthesis methods for differing mesoporous silicas along with the preparation of the highly oxidative piranha acid solution. The methods of analysis which included the instruments that were used was also discussed. The principals of these characterisation techniques were also mentioned and also the operating parameters.

Chapter 3 focused on the hydroxylation of mesoporous silicas. Pre-treatment steps including refluxing in piranha acid solution, nitric acid and water were examined. A dry-cleaning method using ultraviolet/ozonolysis was also carried out. The impact of cleaning showed that re-hydroxylation of siloxanes to silanol groups did not occur. It did however show that silanols present were cleaned of adsorbates and were now accessible for grafting. It was shown that grafting increased due to cleaning especially for piranha acid solution. These processes, common in the semiconductor industry, can now be shown to be very beneficial as efficiency can be increase due to higher grafting numbers. Further work into the area of cleaning should be examined especially looking at other cleaning methods. Some of these might include hydrofluoric acid and methods described as RCA (SC-I & SC-II). Methods used for pore expansion could also be examined to determine if these routes can clean and in turn increase attachment of different functional groups. It would also be worthwhile to prove that other ligands act in the same way as APTS.

Chapter 4 presented the functionalisation of mesoporous silicas with poly-2-vinyl pyridine. Two types of mesoporous silicas were synthesised and studied which are known as SBA-15 and MCM-41. Attachment of differing polymer weights of P2vP to these materials showed two completely different curves for the two materials. SBA-15 which has larger pores, but a lower surface area was able to attain higher loading of the polymer while also more of the higher P2vP weights. Infiltration of metal salts into the silica support is utilised by its interaction with the pyridine ring specifically the nitrogen component. Cerium salt selectively infiltrated into the polymer and was measured. Future work and ideas into this process could be extended to other metal salts. Some of these metals could include nickel, platinum, ruthenium, or titanium with applications such as catalysis and heavy metal extraction. Further research into producing these devices or supports with data to back up their potential performance at their specific role.

Chapter 5 explored the proof of concept of producing potential devices which can utilise the benefits of mesoporous silicas to provide supports as antimicrobial. The chapter examined the

attachment of mesoporous silicas to silicon dioxide wafers using silane linkers on both materials. APTS was grafted to mesoporous silica SBA-15 while silicon substrates were functionalised with GTPS. Oregano essential oils were loaded into SBA-15 and functionalised SBA-15 where antimicrobial activity was determined. Although the device did not show any antimicrobial activity it did prove that the potential joining of the two materials could be useful if examined further. Determining the coverage of GPTS on the wafer and determining the amount of SBA attached could improve its potential. Techniques such as ellipsometry and raman spectroscopy could help in these. Also increasing the potential weight of the oil could impact by improving antimicrobial activity. Finally, further studies at combining mesoporous silicas so polymers which could be included in food packaging to further develop the device.

# *Chapter 7*

# *Appendix*

## 7.1 Appendix

### *7.1.1 Articles to be submitted*

i. 'Functionalisation and optimisation of ordered mesoporous silica with hydroxy-terminated poly-2-vinyl pyridine with applications in metal salt infiltration' - Microporous and mesoporous materials.

### *7.1.2 Conference Presentations*

i. O'Mahony, T F; Morris M A; Lundy R; *'Comparison of functionalisation of mesoporous silicas and silicon wafer substrates with hydroxy-terminated poly-2-vinyl pyridine with metal adsorption by infiltration for various applications'* **ECASIA 2019**, 15-20 September 2019, Dresden, Germany (Oral presentation).

ii. O'Mahony, T F; Morris, M A; *'Effect of rehydroxylation methods on mesoporous silica with direct comparison to functionalisation'* **MRS Fall Meeting,** 1-6 December 2019, Boston, USA (Poster presentation).

iii. O'Mahony, T F; Morris, M A; *'Effect of rehydroxylation methods on mesoporous silica with direct comparison to functionalisation'* **AMBER Conference,** 15 January 2020, Portlaoise, Ireland (Poster presentation).